Near-Surface Snow Temperature Changes Over Terrain

Laura Bakermans

UNIVERSITY OF CALGARY

Near-Surface Snow Temperature Changes Over Terrain

by

Laura Anne Bakermans

A THESIS
SUBMITTED TO THE FACULTY OF GRADUATE STUDIES
IN PARTIAL FULFILMENT OF THE REQUIREMENTS FOR THE
DEGREE OF MASTER OF SCIENCE

DEPARTMENT OF CIVIL ENGINEERING
CALGARY, ALBERTA
NOVEMBER 2006

Abstract

The energy balance at the snow surface results in substantial diurnal temperature fluctuations within the top portion of the snowpack. These temperature fluctuations, which vary both spatially and over time, can have important effects on snowpack stability.

During the winters of 2005 and 2006, field data for a near-surface warming study were collected on a knoll located in the Columbia Mountains of British Columbia. Performance of the Swiss computer model SNOWPACK was compared against field measurements of near-surface snow temperatures.

A semi-empirical warming model was developed from the field dataset for use by avalanche forecasters. The semi-empirical model, which predicts the magnitude of near-surface daytime warming, requires only readily available input parameters like slope, aspect, expected cloud cover and number of days since snowfall. Warming model results can be displayed graphically for different slope and aspect combinations to illustrate variations in daytime warming over terrain.

Acknowledgements

This project would not have been possible without Dr. Bruce Jamieson, who provided supervision, advice, constructive feedback, training and funding.

For their careful measurements and good company in the field, I am grateful to Catherine Brown, James Floyer, Dave Gauthier and Antonia Zeidler. Ali Haeri, Paul Langevin and Ken Matheson shared their enthusiasm and field experience. Cam Campbell, James Floyer and Dave Gauthier provided much-appreciated proofreading.

I would like to thank Dr. Charles Fierz with the Swiss Federal Institute for Snow and Avalanche Research for contributing his thoughts on measuring near-surface snow temperatures and for patiently answering all of my questions about SNOWPACK. I am also grateful to Dr. Patrick Hettiaratchi and Dr. Masaki Hayashi for their comments on this thesis as members of my defence committee.

For field support and practical insight, I thank the Avalanche Control Section of Glacier National Park: Tom Chalmers, Eric Dafoe, Zuzana Driediger, Dean Flick, Jeff Goodrich, Mark Harrison, Bruce McMahon, Jim Phillips and Johan Schleiss.

Jessica Smith with Campbell Scientific Canada, Paul Lavoie, Joe Sabourin and Rob Scorey from the University of Calgary Engineering Faculty Machine Shop and University of Calgary Civil Engineering Technologists Don Anson and Don McCullough provided invaluable assistance with field equipment.

I am also grateful to Alliance Pipeline for their financial support of the Naomi Heffler Memorial Scholarship in Avalanche or Snow Science.

Finally, I would like to thank my parents, Susan and Richard Bakermans, and partner, Sean Fraser, for their support and encouragement.

Table of Contents

List of Tables

List of Figures

List of Symbols and Abbreviations

1F	one finger in glove (hand hardness)
4F	four fingers in glove (hand hardness)
ACS	Avalanche Control Section of Parks Canada
ASARC	Applied Snow and Avalanche Research at the University of Calgary
α	albedo
B_0	linear regression intercept
$B\mathrm{i}$	linear regression coefficient
BKN	broken cloud
β	short wave radiation extinction coefficient
c	cloudiness
c_1	constant (Equation B.20)
c_2	constant (Equation B.20)
clr	contribution of diffuse incoming short wave radiation under clear skies
CAA	Canadian Avalanche Association
CLR	clear sky
d	depth below snow surface
dfN	aspect (degrees from north)
D	Kolmogorov-Smirnov test statistic
D_l	latent turbulent transfer coefficient
D_s	sensible turbulent transfer coefficient
$^{\mathrm{d}T}/_{\mathrm{dz}}$	temperature gradient in the z direction
ΔT_d	daytime warming at depth d
e_s	snow surface vapour pressure
e_sat	saturated water vapour pressure
e_z	vapour pressure at height z
E	east
ENE	east-northeast
ε	emissivity
ε_s	emissivity of snow
F	fist in glove (hand hardness)
FEW	few clouds
GIS	Geographic Information Systems
GNP	Glacier National Park

I	ice - too hard to insert knife (hand hardness)
iLW	incoming long wave radiation under all sky conditions
$\mathrm{iLW}_{\mathrm{avg}}$	average incoming long wave radiation determined from estimated incoming long wave radiation values calculated at 7:00 am and 12:00 noon
$\mathrm{iLW}_{\mathrm{avg\_SWmax}}$	average hourly incoming long wave radiation from sunrise to the time at which the maximum daily value of incoming short wave radiation occurred
$\mathrm{iLW}_{\mathrm{avg\_}T\mathrm{max}}$	average hourly incoming long wave radiation from sunrise to the time at which the maximum snow temperature was measured at depth *d*
$\mathrm{iLW}_{\mathrm{clr}}$	incoming long wave radiation under clear skies
$\mathrm{iLW}_{\Sigma\mathrm{\_SWmax}}$	sum of hourly incoming long wave radiation from sunrise to the time at which the maximum daily value of incoming short wave radiation occurred
$\mathrm{iLW}_{\Sigma\_T\mathrm{max}}$	sum of hourly incoming long wave radiation from sunrise to the time at which the maximum snow temperature was measured at depth *d*
k	thermal conductivity
K	knife blade (hand hardness)
K-S	Kolmogorov-Smirnov
λ_{max}	wavelength of energy emitted with greatest intensity
MB	mean bias
μ_{meas}	mean of measured dataset
μ_{mod}	mean of modelled dataset
n	number of data points included in analysis
N	north
N	number of days since snowfall
NE	northeast
NNE	north-northeast
NW	northwest
oLW	outgoing long wave radiation
$\mathrm{oLW}_{\mathrm{avg}}$	average outgoing long wave radiation determined from estimated surface temperature values calculated at 7:00 am and 12:00 noon
$\mathrm{oLW}_{\Sigma\mathrm{\_SWmax}}$	outgoing long wave radiation sum determined by multiplying $\mathrm{oLW}_{\mathrm{avg}}$ by the number of hours from sunrise to the time at which the maximum daily value of incoming short wave radiation occurred
$\mathrm{oLW}_{\Sigma\_T\mathrm{max}}$	outgoing long wave radiation sum determined by multiplying $\mathrm{oLW}_{\mathrm{avg}}$ by the number of hours from sunrise to the time at which the maximum daily value of incoming short wave radiation occurred
OBS	obscured sky
OVC	overcast sky

p	statistical significance value
P	blunt end of pencil (hand hardness)
PST	Pacific Standard Time
Q_{c}	conductive heat flux
Q_{l}	latent turbulent heat flux
Q_{lw}	net long wave radiation flux
Q_{p}	heat flux from precipitation
Q_{s}	sensible turbulent heat flux
Q_{sw}	short wave radiation flux
Q_{t}	total heat flux
r	Pearson correlation coefficient
r^2	coefficient of determination
R_{e}	emitted radiation
RH	relative humidity
RMSE	root mean square error
ρ	snow density
sigma	standard deviation of regression residuals
S	south
S_0	solar constant
SCT	scattered cloud
SE	southeast
SEE	standard error of estimate
SH	surface hoar
SLF	Swiss Federal Institute for Snow and Avalanche Research
SW	southwest
$\mathrm{SW}_{\mathrm{all}}$	incoming short wave radiation under all sky conditions
$\mathrm{SW}_{\mathrm{clr}}$	incoming short wave radiation under clear skies
SW_{d}	short wave radiation at depth d
$\mathrm{SW}_{\mathrm{diff}}$	diffuse incoming short wave radiation
$\mathrm{SW}_{\mathrm{dir}}$	direct incoming short wave radiation
$\mathrm{SW}_{\mathrm{max}}$	maximum daily value of incoming short wave radiation
SW_{s}	short wave radiation incident on the snow surface
$\mathrm{SW}_{\Sigma\_\mathrm{SWmax}}$	sum of hourly short wave radiation values from sunrise to the time at which the maximum daily value of incoming short wave radiation occurred
$\mathrm{SW}_{\Sigma\_T\mathrm{max}}$	sum of hourly short wave radiation values from sunrise to the time at which the maximum snow temperature was measured at depth d
σ	Stefan-Boltzman constant

t_c	cloud transmissivity
T	temperature
T_0	screen-level air temperature
T_a	air temperature
T_{err}	temperature measurement error
T_{meas}	measured snow temperature
T_{mod}	SNOWPACK modelled snow temperature
T_s	snow surface temperature
T_z	air temperature at height z
θ	solar zenith angle
u	wind speed
u_{avg}	average wind speed
u_z	wind speed at height z
w	precipitable water content
W	west
WW	Willmott and Wicks index of agreement
Z	Mann-Whitney U-test statistic

CHAPTER ONE: INTRODUCTION

An avalanche is a moving mass of snow, which may also contain soil, ice or rocks. Avalanche hazard exists when people or structures are exposed to avalanches, creating potential for injury, death or damage.

Statistics compiled by the Canadian Avalanche Association (CAA) indicated a yearly average of eleven avalanche related fatalities between 1970 and 2003. The reported average is sixteen fatalities per year in the latter five years of this time period (CAA, 2003). While the majority of the above noted accidents involved backcountry recreationalists, avalanches also have substantial impacts on industry and transportation. Avalanche forecasting/control measures and road closures are expensive; estimates prepared for Canada suggest annual costs of $10 million (McClung and Schaerer, 1993, p. 15) and $5 million (Jamieson and Stethem, 2002), respectively. The destruction of valuable natural resources like merchantable timber also has substantial economic effects. Jamieson and Stethem (2002) report damage of approximately $400,000 worth of timber by one avalanche near Revelstoke, British Columbia.

Avalanche forecasting, the process of evaluating snow stability and avalanche hazard, involves consideration of numerous snowpack, weather and terrain factors. Access to relevant information about the snowpack structure and potential instabilities helps people working and traveling in avalanche terrain make better decisions. This thesis focuses on near-surface snowpack warming, which contributes to the spatially variable nature of the snowpack and can be difficult to visualize over terrain. The primary research objective is to develop a spatial warming model, with practical data input requirements, that will provide avalanche forecasters with additional information for consideration when evaluating stability. Field data collected will also be used to verify modelling of near-surface snow temperatures by the Swiss model SNOWPACK.

1.1 Avalanches

There are two main types of avalanches: loose snow avalanches and slab avalanches (Figure 1.1). Loose snow avalanches initiate from a loss of cohesion at a single point, which sets additional snow in motion, fanning out in a triangular shape. Slab avalanches occur when snow releases as a cohesive unit and slides over a failed weak layer. Data compiled by the Canadian Avalanche Association (CAA) show that, between 1984 and 2003, 96% of the reported recreational avalanche accidents involved slab avalanches (CAA, 2003).

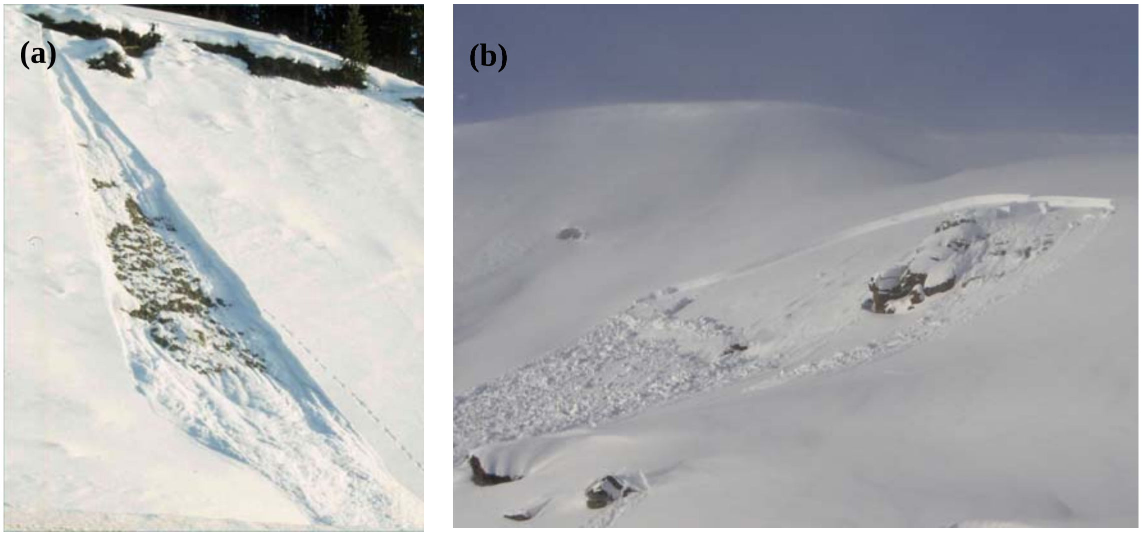

Figure 1.1: *Two types of avalanches: (a) Loose snow avalanche (photo: B. Jamieson). (b) Slab avalanche.*

1.2 Mountain snowpack

Snow forms as tiny ice crystals within atmospheric clouds. The size and shape of the snow crystals depend on the atmospheric temperature and water vapour density (McClung and Schaerer, 1993, p. 40). Size and shape changes occur as the crystals fall through regions of different temperature and water vapour density en-route to the earth's surface. Sublimation and mechanical interactions due to wind also result in snow crystal changes.

The snowpack consists of layers deposited under different meteorological conditions, each with distinct properties. This layered structure is critical for slab avalanche formation, which requires a cohesive slab above a weaker layer. The relative strengths of adjacent layers, as well as the degree of bonding between them, will vary depending on conditions within the snowpack.

The six-pointed stellar crystal shape typically formed in the highly supersaturated atmosphere is not stable in the snowpack, which has a typical supersaturation value of about 1 % (McClung and Schaerer, 1993, p. 46). Initial shape changes in new snow crystals reflect a transition towards spherical particles, as mass is sublimated from areas of high vapour pressure (branch tips) to low vapour pressure (convexities). This initial rounding, which results from very localized vapour pressure gradients, is soon overwhelmed by the effects of temperature gradients within the snowpack. Depending on the magnitude of the resultant vapour pressure gradient, one of two types of metamorphism will occur. Low temperature gradients (<10 ºC/m) indicate low vapour pressure gradients, under which continued rounding of the snow crystals will occur. This process is often termed equilibrium or equi-temperature metamorphism. Rounded crystals tend to bond well to one another, forming strong layers within the snowpack. Vapour pressure gradients caused by strong temperature gradients (>10 ºC/m) result in the growth of large, angular crystals (facets) as ice sublimated from one crystal is deposited on the neighbouring crystal. Faceting, also known as kinetic metamorphism, produces crystals that do not typically bond well and, once buried, become a potential weak layer within the snowpack. Facets large enough to be a concern can develop in a day under ideal conditions, although several days is a more typical time frame (Birkeland, 1998).

Surface hoar, described as the solid equivalent of dew (McClung and Schaerer, 1993, p. 44), consists of angular, cup-shaped crystals formed as a result of vapour pressure gradients above the snow surface. Requirements for surface hoar formation are a supply of water vapour in the air and a temperature gradient above a cool snow surface. Like facets, surface hoar crystals do not bond well and often become weak layers when buried in the snowpack.

The presence of weak layers within the snowpack is a critical factor in the formation of slab avalanches. Weak layers often develop on the snow surface and are buried by subsequent snowfall. Surface processes also impact slab characteristics, which are important with respect to avalanche initiation and propagation. An understanding of the processes that affect the snow surface, like near-surface warming, is therefore valuable in determining when and where weak layers may be present within the snowpack.

The spatially variable nature of the snowpack in mountainous areas complicates stability evaluation. Sturm et al. (1995) comment on the difficulty inherent in classifying mountain snow cover because of its spatial variability; wind turbulence and the distribution of incoming short wave radiation over complex terrain are cited as the most important factors contributing to this spatial variability. Colbeck (1991) also suggests that the strong influence of short wave radiation and diurnal swings in near-surface temperature gradient add complexity to the evaluation of upper snowpack layers.

1.3 Forecasting

Avalanche forecasters evaluate current and future snow stability by synthesizing data from a variety of sources. The forecasting process is undertaken by personnel making closure and control decisions for a highway or ski area, organizations providing bulletins for public recreation areas and by guides selecting routes for a day of ski touring. In addition to the accuracy and relevance of available input data, the experience, insight and local knowledge of the forecaster are important.

As illustrated in Figure 1.2, avalanche forecasters consider three classes of information in evaluating stability (McClung and Schaerer, 1993, Chapter 6). The first,

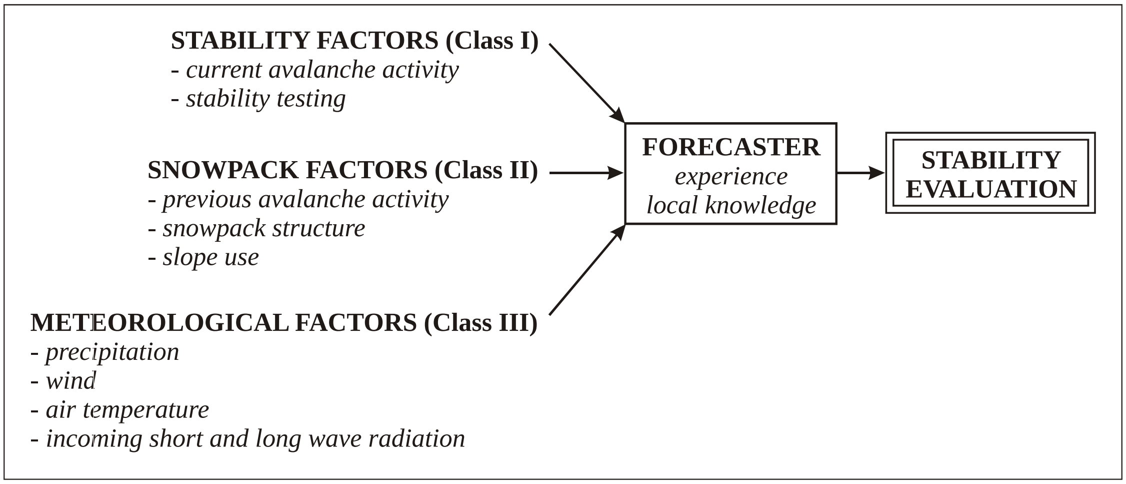

Figure 1.2: *Factors considered by an avalanche forecaster when evaluating stability (after McClung and Schaerer, 1993, Chapter 6).*

and most directly indicative of avalanche potential, consists of stability factors (often termed Class I factors). These include observations of current avalanche activity, the results of field stability tests and slope testing with explosives or by ski cutting. Class II factors pertain to the structure of the snowpack and the relationship between potential snowpack weaknesses and the loads upon them. Examples are manual observations of snowpack layer properties like density, hardness, grain type and grain size. Meteorological data like precipitation, wind speed, temperature and radiation measurements can provide indirect evidence about current and future snow stability. These are considered to be Class III factors. The emphasis given to information included in the forecasting process typically decreases as the observations become less direct (i.e. Class I factors are given more weight than Class III factors).

The amount and sophistication of available information can vary greatly depending on the type of operation and size of the forecast area. With larger forecast areas, more variability in snowpack and weather conditions exists. In a study comparing forecast danger levels with local danger ratings based on field observations, Jamieson et al. (2006) found that, for large forecast areas (approximately 25,000 km^2), reduction in forecast area would likely result in greater improvements in forecast accuracy than an increase in forecast frequency.

1.4 Snowpack evolution modelling

Avalanche forecasters rely on point observations of snowpack structure that are often limited and specific to certain terrain features. Collection of sufficient detailed snow profile information to represent the spatial variability of the snowpack is not always practical due to time and access constraints. As such, there is considerable interest in developing computer models capable of accurately modelling snowpack evolution under different conditions. Computer models currently used in operational avalanche forecasting allow for consideration of complex snowpack processes.

Computer modelling of the energy exchange at the snow surface began initially for hydrological purposes. Early models have since expanded to include internal snowpack processes, like grain metamorphism, and information relevant for snow stability evaluation, like snowpack layering. SNOWPACK (Bartelt and Lehning, 2002) and CROCUS (Brun et al., 1992) are two well-developed models currently used in operational avalanche forecasting in Europe. To determine the energy balance at the snow surface, each model uses meteorological parameters as input. In addition, estimation or calculation of several snowpack dependent parameters is required.

Accurate and continuous meteorological measurements are essential for successful modelling, which limits the practicality for many users. Measurements of incoming short and long wave radiation, particularly, are uncommon for most avalanche forecasting operations in Canada. In addition to constraints on the availability of input data, variability in terrain, snowpack and weather parameters limits model performance.

1.5 Near-surface warming

Daily temperature fluctuations in the upper snowpack result from the surface energy balance. These fluctuations vary spatially and over time, and can have important effects on stability. The primary mechanisms of energy exchange which contribute to these temperature fluctuations are radiation, conduction and convection (Figure 1.3). The

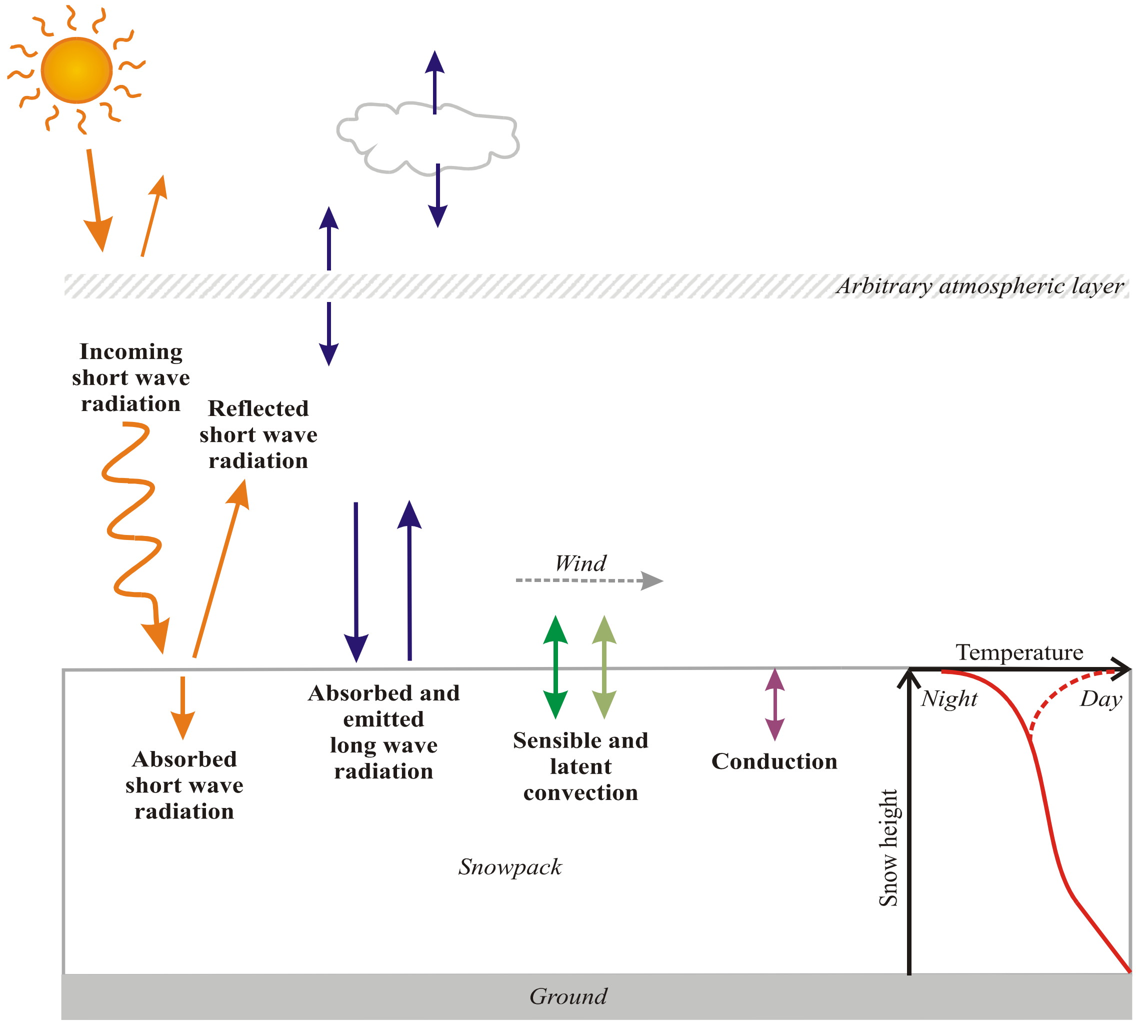

Figure 1.3: *Key components of the snow surface energy balance, with an example of the resultant diurnal temperature fluctuations in the top portion of the snowpack (after McClung and Schaerer, 1993, p. 34, p. 45).*

terms included in the calculation of the total surface energy flux, which is the energy available for temperature or phase change at the snow surface, are given in Equation 1.1. Energy fluxes into the snowpack are typically defined as positive; a positive total surface energy flux indicates that the snow surface is warming, while a negative total energy flux results in cooling of the snow surface.

$$Q_t = Q_{sw} + Q_{lw} + Q_s + Q_l + Q_c \tag{1.1}$$

where Q_t = total surface energy flux
Q_{sw} = net short wave radiation flux
Q_{lw} = net long wave radiation flux
Q_s = sensible turbulent heat flux
Q_l = latent turbulent heat flux
Q_c = conductive heat flux

An additional term is often included in net surface energy balance calculations to account for heat added to the snowpack by liquid precipitation.

1.5.1 Radiation

Radiation is energy transfer in the form of electromagnetic waves. The electromagnetic waves, which travel at the speed of light, define the quantity (wave amplitude) and type (wavelength) of energy transferred. Figure 1.4 shows the common wavelength bands used to categorize radiation.

All objects above 0 kelvin emit radiation. The following equations define the relationships between the temperature of the object and the intensity and wavelength of emitted radiation. Simply put, hotter objects release more energy at shorter wavelengths than cooler objects.

$$R_e = \varepsilon \cdot \sigma \cdot (T + 273.15)^4 \tag{1.2}$$

$$\lambda_{max} = 2900 / (T + 273.15) \qquad \textit{Wiens Law} \tag{1.3}$$

where R_e = emitted radiation (W/m^2)
ε = emissivity
σ = Stefan-Boltzman constant (5.67×10^{-8} W/m^{2}K^4)
T = temperature (ºC)
λ_{max} = wavelength of energy emitted with greatest intensity (µm)

Approximately 99% of the radiation emitted by the sun is short wave radiation, while approximately 99% of the radiation emitted by all other objects is long wave radiation. Literature shows some variation in the value, but 4 μm is typical for defining the transition from short wave to long wave (Figure 1.4). Short wave radiation emitted by the sun and long wave radiation emitted by the earth's surface, clouds and the atmosphere both strongly influence the energy balance at the snow surface.

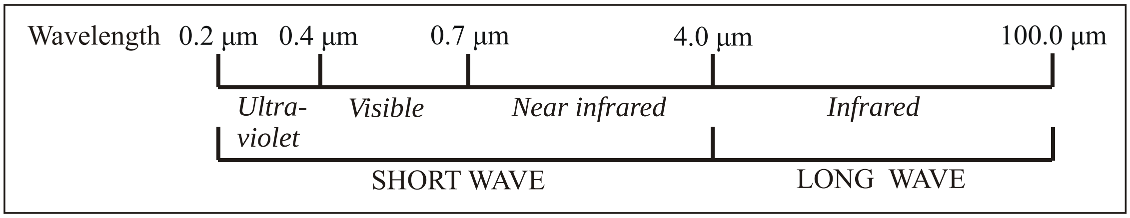

Figure 1.4: *Common wavelength bands used to categorize radiation.*

Short wave radiation

The amount of solar energy released by the sun is relatively constant (1367 W/m^2). The amount reaching any given location on the earth's surface, however, depends on a number of factors. Latitude, elevation, time of year and time of day all affect the distance from the sun, the path length through the atmosphere, and the angle at which the incoming radiation hits the surface.

The earth's atmosphere absorbs and scatters some solar radiation before it reaches the snow surface. Scattered short wave radiation reaching the earth's surface is termed diffuse radiation, while the portion unaffected by the atmosphere is known as direct radiation. The term global solar radiation includes both the direct and diffuse components. Male and Gray (1981) estimate that diffuse radiation makes up approximately 10% of global solar radiation on clear days, increasing to 100% under overcast conditions.

At the snow surface, both reflection and absorption of global radiation occur. For a given surface, the albedo is defined as the ratio of reflected radiation to total incoming radiation, integrated over the short wave radiation spectrum (e.g. Male and Gray, 1981). Reflected radiation includes that which enters the snowpack and is scattered back out by snow grains in the uppermost snow layer. Snow albedo values cited by Male and Gray (1981) range from 0.95 for clean, dry compact snow to 0.61 for clean, wet granular snow. In his paper summarizing models of the optical properties of snow, Warren (1982) outlines numerous factors which influence snow albedo. These include wavelength, cloud cover, solar zenith angle, grain size, liquid water content, impurity concentration and surface roughness.

Short wave radiation that is not reflected out of the snowpack decreases in intensity with depth below the surface. Attenuation of short wave radiation within the snowpack, which occurs through absorption and scattering by individual snow crystals, is a function of wavelength and the snow crystal characteristics. Near infrared radiation at the longer wavelength end of the short wave radiation spectrum attenuates quickly, while shorter wavelengths are associated with greater penetration depth. Grain radius, snow density, moisture content and the presence of impurities also affect scattering and absorption; these snow properties therefore influence depth of penetration (Warren, 1982). McClung and Schaerer (1993, p. 33) estimate that less than 10% of solar radiation penetrates to a depth greater than 10 cm. This depth, over which incoming short wave radiation contributes to warming, will vary depending on the properties of the surface snowpack layers.

Long wave radiation

In addition to long wave radiation emitted from the snow itself, the net long wave radiation flux at the snow surface includes incoming long wave radiation emitted by clouds, the atmosphere, trees and surrounding terrain features. Reflection of long wave radiation is commonly neglected in snow surface energy balance calculations because the long wave reflectance of snow, equal to 1 minus the emissivity, is very small (e.g. Male and Granger, 1981; Warren, 1982; Plüss, 1997).

Atmospheric incoming long wave radiation is emitted by ozone, carbon dioxide and water vapour. Male and Gray (1981) estimate that these components emit approximately 2%, 17% and 81% of the total, respectively. Variations in atmospheric incoming long wave radiation are attributed primarily to differences in the amount and temperature of atmospheric water vapour. Ohmura's (2000) radiation modelling showed that, under a cloudless sky, approximately 60% and 90% of the incoming long wave radiation originated within the first 100 m and 1 km of the earth's surface, respectively.

Because the net long wave radiation flux at the snow surface consists of both incoming and outgoing radiation, the result can be either warming or cooling. McClung and Schaerer (1993, p. 33) note that most incident long wave radiation is absorbed within 1 cm of the snow surface. The effects of the net long wave radiation balance are essentially limited to the snow surface.

1.5.2 Convection

Convection is the transfer of heat by turbulent mixing of a fluid medium. There are two types of convective heat flux: sensible and latent. Sensible heat flux occurs because of a temperature difference between the air and the snow surface. Latent heat flux results from energy created or absorbed by a change in phase, often caused by a difference in vapour pressure between the air and the snow. Some examples of latent heat fluxes include heat released as liquid precipitation freezes, or heat released as water vapour condenses on the snow surface during surface hoar formation.

Equations 1.4 and 1.5 are typical for simplified calculation of sensible and latent heat fluxes at the snow surface (Male and Gray, 1981).

$$Q_s = D_s \cdot u_z \cdot (T_z - T_s) \tag{1.4}$$

$$Q_l = D_l \cdot u_z \cdot (e_z - e_s) \tag{1.5}$$

where Q_s = sensible heat flux (W/m^2)
Q_l = latent heat flux (W/m^2)
D_s = sensible turbulent transfer coefficient (kJ/m^3·°C)
u_z = wind speed at height z (m/s)
T_z = air temperature at height z (°C)
T_s = snow surface temperature (°C)
D_l = latent turbulent transfer coefficient (kJ/m^3·mb)
e_z = vapour pressure at height z (mb)
e_s = snow surface vapour pressure (mb)

Like the effects of the net long wave radiation flux, convective heat transfer processes occur primarily at the snow surface and can result in either warming or cooling. Sensible turbulent heat exchanges can be significant when strong winds are associated with particularly warm or cool air temperatures relative to the snow surface. Fierz et al. (2003) note that while the effects of turbulent heat exchange on the surface energy balance are minor when considered over long time periods, they can be critical at time periods less than a day.

1.5.3 Conduction

The movement of heat through a substance via transfer of energy from molecule to adjacent molecule is termed conduction. Conductive heat flux is defined using Fourier's law (Equation 1.6).

$$Q_c = -k \cdot {}^{dT}/_{dz} \qquad (1.6)$$

where Q_c = conductive heat flux (W/m^2)
k = thermal conductivity (W/m·ºC)
${}^{dT}/_{dz}$ = temperature gradient in the z direction (ºC/m)

Heat conduction through snow, especially low density snow as often found near the surface, is not an efficient heat transfer process. In the snowpack, conduction can occur through connected ice grains or through air in the pore spaces between grains. Often, latent heat transfer resulting from sublimation within the pore spaces is included in the calculation of conductive heat fluxes. In these cases, the thermal conductivity value in Equation 1.6 is replaced by a value, termed effective conductivity, which includes this process.

The efficiency of conduction through the ice skeleton relates to grain characteristics and bonding. Sturm et al. (1997) used density, as an indicator of grain connectedness, to estimate effective conductivity. Results of this analysis, which was based on a comprehensive set of data points, indicated that the relationship between density and effective conductivity was strong for rounded grains and wind damaged snow. The effective conductivity of faceted crystals and surface hoar, however, was relatively independent of density.

Sturm et al. (1997) also note that conduction through connected ice grains can be up to one hundred times greater than conduction through air in the pore spaces. When the thermal conductivity through the ice grains is low, higher temperature and vapour pressure gradients result and latent heat transport across the pore spaces is high. The opposite effect occurs when the thermal conductivity through the ice grains is high. Connected ice grains can also inhibit movement of vapour in the pore spaces. The arrangement of grains and pores, as well as their size, affects the relative strengths of these processes, as do the temperature and temperature gradient.

Adams and Sato (1993) assumed a snowpack made up of uniform interconnected spheres to calculate values for effective thermal conductivity. Their calculations also indicated that density is a strong indicator of thermal conductivity, as is the degree of bonding; calculated values increased with the ratio of bond radius to grain radius.

1.5.4 Net surface energy flux

The net energy flux at the snow surface is a sum of the energy transfer processes outlined above (Equation 1.1). As discussed, a number of different factors influence each of the energy flux terms. Of the different heat transfer mechanisms, radiation is often the most dominant, but the relative importance of each term will vary because of differences in location, terrain, snowpack characteristics, meteorological conditions and time of year and/or day.

1.5.5 Effects of near-surface temperature changes on snowpack stability

Temperature fluctuations within the top portion of the snowpack affect stability through development of weak layers and changes in the properties of existing slabs. These temperature fluctuations can vary substantially with location and over time, and the net effects on snowpack stability can be hard to quantify. Even when the magnitude of heat exchanged is very small, heat exchange processes can have a significant impact on snow stability; an example is the development of surface hoar.

McClung and Schweizer (1997) describe two opposing effects of snow temperature change on dry snow slab stability; these occur on different time scales. The delayed effects of warming are rounding, bonding and creep, which tend to promote stability by increasing the density and hardness of affected snow layers. The immediate effects of an increase in temperature are changes in the mechanical properties of the slab. These include decreases in the stiffness, failure toughness and failure strength, which are associated with a reduction in stability.

McClung (1996) suggests that temperature has greater effects on the stiffness and failure toughness of snow than on failure strength. Decreases in snow stiffness due to warming are attributed to increases in strain components during ice deformation. Delayed elastic deformation associated with intergranular sliding and viscous deformation due to intergranular deformation are strongly dependent on temperature between -1 ºC and -20 ºC. McClung (1996) notes that a third component of ice deformation, pure elastic deformation in the ice lattice, is not strongly dependent on temperature within this range.

A decrease in slab stiffness results in increased strain and strain rates at the weak layer (Schweizer et al., 2003). This result is important because it indicates that stability will decrease even if warming does not reach the weak layer. McClung and Schaerer (1993, p. 82) note that temperature release observations typically correspond to slabs less than 0.5 m thick overlying a very weak layer. If warming reaches the weak layer, decreases in weak layer toughness and strength will further contribute to decreased stability. Less stiff slabs also allow deformation resulting from surface loads, such as skiers or snowmobiles, to penetrate deeper (McClung and Schweizer, 1997).

Sudden cooling has the reverse effect on slab stiffness compared to the rapid warming discussed above, decreasing the probability of skier triggering. However, cooling of the snow surface can lead to strong temperature gradients in the top snowpack layers and promote conditions favourable for faceting and surface hoar growth. These weak layers are potential failure layers for slab avalanches once buried by subsequent snowfall.

Incoming short wave radiation and outgoing long wave radiation combine to produce diurnal fluctuations, in which rapid night time cooling often follows rapid daytime warming. Daily surface temperature variations can result in near-surface faceting due to strong temperature gradients, overnight surface hoar formation, or the development of melt-freeze crusts. In addition to creating a smooth sliding surface for potential avalanches, the presence of crusts buried within the snowpack can promote near-crust faceting

When surface cooling due to outgoing long wave radiation and/or turbulent heat exchange occurs at the same time as warming of the top portion of the snowpack by incoming solar radiation, the result is a strong temperature gradient within the top snow layer, as shown in Figure 1.5. These conditions favour the development of near-surface facets. This process, known as radiation recrystallization, is more effective in low density snow because conductive heat transfer is less efficient in reducing the magnitude of the temperature gradient in the top snow layer. Temperature gradients sufficient for faceting would not persist if conductive heat transfer through the snowpack was efficient.

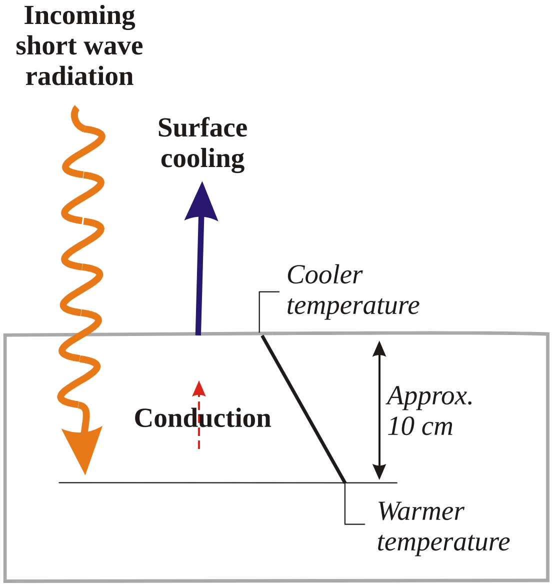

Figure 1.5: *Schematic showing a strong temperature gradient within the top snow layer due to surface cooling combined with warming of the upper portion of the snowpack by incoming solar radiation. This process, termed radiation recrystallization, results in the formation of near-surface faceted crystals.*

1.6 Research objectives

The objectives of this thesis are as follows:

1. Investigate variation in the magnitude of daytime snowpack temperature changes as a result of differences in time of year, cloud cover, slope angle and aspect.

2. Run the Swiss computer model SNOWPACK using data collected in the Columbia Mountains of British Columbia and compare the modelled near-surface temperatures to field measurements.
3. Using field data, develop a warming model to illustrate variation in daytime snowpack temperature changes given a set of easily measured input parameters.
4. Display the warming model output graphically for ease of interpretation by avalanche forecast and control teams.

Modelling the effects of warming on stability is beyond the scope of this thesis project. The intent of the warming model is to provide information about the magnitude and variability of near-surface warming. This will add to available information, and may help forecasters identify areas where additional field observations would be most useful. Ease of use is an important consideration, as avalanche forecasters typically have limited time and resources. In Canada, where forecast areas are often very large and representative meteorological data (particularly radiation data) not always available, a simple model is perhaps more applicable than a complex computer simulation.

Chapter 2 is a literature review relevant to the energy balance at the snow surface and modelling near-surface warming. Chapter 3 outlines field equipment and methods used for data collection. Some field data examples are included in Chapter 4. Comparison of the SNOWPACK model to field measurements is presented in Chapter 5. In Chapter 6, development and display of a practical warming model are discussed. Chapter 7 summarizes conclusions and presents recommendations for further research.

CHAPTER TWO: LITERATURE REVIEW

A brief discussion of the effects of terrain, weather and snowpack properties on the surface energy balance is presented in Section 2.1. Surface energy balance modelling is summarized in Section 2.2, followed by an introduction to the snowpack evolution models CROCUS and SNOWPACK in Section 2.3. Section 2.4 reviews several methods of measuring near-surface snow temperatures and touches on the difficulties inherent in doing so accurately.

2.1 Surface energy balance

The key components of the surface energy balance were identified and discussed briefly in Section 1.5. Male and Gray (1981) provide a detailed description of surface energy fluxes, and the factors which influence them, in their summary of the physical processes contributing to snowmelt. Another thorough synopsis, specific to snowmelt over mountainous terrain, is given by Obled and Harder (1978).

Many discussions of the surface energy balance suggest that net radiation is often the largest component (e.g. Obled and Harder, 1978; Male and Granger, 1981; Plüss, 1997). McClung and Schaerer (1993, p. 33) attribute quick changes in near-surface temperature to the changing balance between short and long wave radiation. Because the focus of this study is on rapid temperature changes in the upper portion of the snowpack, subsequent sections will concentrate primarily on variation in radiation fluxes.

2.1.1 Terrain

Terrain parameters like aspect and slope angle come in to the surface energy balance primarily as modifiers of the amount of incoming short wave radiation received. Latitude, elevation, time of year and time of day also affect the distance from the sun, the path length through the atmosphere, and the angle at which the incoming short wave radiation hits the surface; along with aspect and slope angle these parameters are fundamental in determining how much direct short wave radiation is incident on a particular slope. Male and Gray (1981) note that the effects of slope and aspect on daily values of direct incoming short wave radiation, which are symmetric across a north-south line, decrease towards the summer solstice.

Deems et al. (2002) studied the relationship between topography and geographic patterns in snow temperature gradients. Their results indicated that temperature gradients had limited dependence on terrain parameters; however, the analysis was limited to depths greater than 30 cm below the snow surface and is not indicative of the rapid near-surface temperature changes resulting from the surface energy balance.

During field trials conducted in Montana, Cooperstein et al. (2004) measured temperatures within the top portion of the snowpack at two sites, one north-facing and one south-facing, to compare the effects of aspect on the formation of persistent weak layers. Analysis of the meteorological data indicated that the south-facing site received more incoming short wave radiation, had higher surface temperatures and experienced more diurnal temperature fluctuation than the north-facing site. The temperature gradient between the air and the snow surface appeared higher at the north-facing site. Field observations indicated better developed near surface facets on the south-facing slope and larger surface hoar crystals on the north-facing slope. Cooperstein et al. (2004) credited these differences in grain type to the aspect-dependent variations in near-surface snow temperatures.

Surrounding terrain can strongly influence the net radiation exchange at the snow surface. Both the short and long wave components are affected. In addition to direct and diffuse incoming short wave radiation from the sun, additional diffuse short wave radiation is reflected by nearby terrain. Shading by nearby terrain features can act to eliminate the direct short wave component. In a similar manner, incoming atmospheric long wave radiation is reduced when the sky is obstructed by surrounding topography. However, these terrain features are also emitting long wave radiation which will add to the incident long wave radiation at the point of interest.

Plüss and Ohmura (1996) undertook sensitivity analysis, based on long wave radiance calculations used in the model LOWTRAN7, to determine the importance of long wave radiation contributions from surrounding terrain. Their analysis indicated that this component was small for flat sites, but that contributions from nearby terrain were important in long wave radiation balance calculations for sloped sites. Results showed that the intervening air temperature should also be considered in the calculations if different from the temperature of the emitting surface.

Plüss (1997) verified parameterizations for energy balance fluxes using measurements made in the eastern Swiss Alps. Energy fluxes calculated in an alpine area from these parameterizations showed similar incoming radiation values for both shaded slopes and open horizontal sites. This result was explained by the increased short and long wave radiation fluxes incident on the shaded slope as a result of reflection and emission from surrounding terrain features.

2.1.2 Cloud cover

Cloud cover influences the magnitude of short wave radiation reaching the snow surface, as well as the division between direct and diffuse incoming short wave radiation. Changes to the spectral distribution of incoming short wave radiation as a result of absorption by clouds also has an effect on the albedo (Warren, 1982) and short wave radiation extinction coefficient (Brandt and Warren, 1993).

As noted in Section 1.5.1, incoming long wave radiation at the snow surface includes long wave radiation emitted by clouds. One difficulty in estimating incoming radiation fluxes, as noted by Fierz et al. (2003), is that cloud cover attributes like height, thickness, or size and distribution of holes, are not reflected in the manual observations typically used as the basis for parameterization; these attributes will affect the amount of long wave radiation emitted by the cloud cover. This limitation in manual sky condition observations will also impact methods of estimating incoming short wave radiation.

2.1.3 Wind and air temperature

Air temperature can play an important role in the surface energy balance if it differs considerably from the snow surface temperature and/or strong winds are present. Turbulent heat fluxes will increase under these conditions.

While air temperature does not initially seem to be an important factor in determining radiation fluxes, early methods of estimating melt rate using air temperature measurements proved to be quite successful. Ohmura (2000) concluded that the physical explanation for the success of these simple models is the dominance of long wave atmospheric radiation during snowmelt and the reasonable approximation of near-surface atmosphere temperature provided by screen-level air temperature. Screen-level air temperature refers to a measurement made in a louvered screen meeting meteorological standards. Male and Gray (1981) also note a good correlation between air temperature at screen level and incoming long wave radiation. Absorbed global radiation and sensible turbulent heat flux, identified by Ohmura (2000) as the second and third largest contributions to melt energy, also correlate well with air temperature.

In their work describing and comparing several methods of calculating sensible and latent turbulent fluxes, Plüss and Mazzoni (1994) note the difficulty of obtaining direct turbulent flux measurements. In their summary of several energy balance studies in alpine environments, they suggest that sensible turbulent fluxes can range in magnitude from negligible to comparable with net radiation, while latent turbulent heat fluxes are typically much smaller. Important conclusions include the observation that sensible and latent heat fluxes are often of similar magnitude but opposite sign. The variable magnitude of turbulent heat fluxes is also noted. During snowmelt, Ohmura (2000) estimated that the contribution of the turbulent sensible heat flux was less than 20% of the incoming long wave radiation flux.

2.1.4 Tree cover

Like surrounding terrain, tree cover changes the balance of both short and long wave radiation at the snow surface. Trees can shade the snow surface from direct incoming short wave radiation and can alter incoming short wave fluxes by reflection from their trunks. Long wave radiation incident on the snow surface will increase near trees due to emissions from the trunks and canopy. Woo and Giesbrecht (2000) provide a good explanation of how a single tree affects the snow surface energy balance.

Woo and Giesbrecht (2000) and Giesbrecht and Woo (2000) describe melt models created to reproduce snowmelt under a single spruce tree and within a spruce woodland, respectively. Results of their single tree model study indicated that radiation fluxes were the key energy balance component during snowmelt, typically contributing more than 90% of the total melt energy. The reduction in incoming short wave radiation resulting from the tree canopy was offset by increased incoming long wave radiation. Additional long wave radiation fluxes from the tree enhanced melting, particularly under overcast conditions.

Link et al. (2004) also observed an increase in incoming long wave radiation along with a reduction in incoming short wave radiation under the tree canopy. Based on radiation measurements made above-canopy and on the snow surface, however, their data indicated a net decrease in total radiation of 22-25% beneath the canopy.

Rowlands et al. (2002) also compared incoming short and long wave radiation measurements above and below the tree canopy. Their data, collected under isothermal conditions in March, included measurements made with radiometer arrays in both dense and open forested areas. Thermocouples and a portable scanning thermal radiometer measured snow surface, underbrush and tree trunk temperatures. The following key observations pertaining to the influence of tree cover on the surface energy balance were reported:

- The spatial distribution of short wave radiation under the open forest varied over time as the solar position changed. The spatial distribution of long wave radiation under the open forest canopy was less variable.
- The difference between incoming short wave radiation above and below the canopy decreased on a cloudy day, as did the spatial variability in incoming short wave radiation.
- On a clear day, measurements of incoming long wave radiation were highest under dense forest canopy, lower in the open forest area and lowest above the canopy. Values measured at all three locations were similar on the cloudy day.
- More variation in surface temperatures (i.e. between the snow surface, understorey and tree trunks) was observed in the open forest area. Measured surface temperatures remained similar under the dense canopy.

Tree cover will also affect turbulent heat fluxes. Giesbrecht and Woo (2000) noted that, during snow melt, turbulent fluxes played a relatively minor role within the spruce woodland because of low wind speeds within tree covered areas.

After favourable comparison of model results against field measurements made in both a forest clearing and a coniferous forest, Koivusalo and Kokkonen (2002) examined their model output to identify differences in surface energy fluxes at the two sites. Model results showed that, in midwinter, sensible heat fluxes dominated in the clearing, while both sensible heat fluxes and net radiation were important within the forest. Again, the importance of sensible heat fluxes was attributed in part to higher wind speeds. With stronger short wave radiation inputs in the spring time, the net radiation flux became the most important surface energy input at both sites. The study notes that field measurements were not available to validate the modeled turbulent flux values.

2.2 Modelling the surface energy balance

Most surface energy balance models were initially developed to study snowmelt for hydrological purposes. Early models consisted of seasonal melt rate calculations made over a drainage basin, typically based on average air temperature measurements. Ohmura (2000) provides a good summary of melt rate estimation methods based on air temperature. Physically-based snowmelt models then developed; Anderson (1976) is often cited as one of the very first point energy balance models for snowcover (e.g. Plüss, 1997). Energy balance models advanced rapidly with improvements both in the availability of meteorological input data and in computational capacity. Some examples are Marks et al. (1999), who present modifications to a physically-based point snowmelt model for application over digital terrain information, and Brock and Arnold (2000), who discuss a point snowmelt model in Microsoft Excel spreadsheet format that can be easily modified and applied to different sites. There are many existing snowmelt models; most require radiation data, deal specifically with a melting snowpack and provide output in terms of a melt rate.

Kondo and Yamazaki (1990) describe a snowmelt model that includes calculation of the snow surface temperature and freezing depth. This model, which assumes a constant linear temperature profile over the depth of the snowpack, was developed to include consideration of night time refreezing in runoff calculations. Kondo and

Yamazaki (1990) note that this linear temperature profile approximation does not apply in mid-winter when temperatures in lower snowpack layers fall below freezing. Input requirements include either measured or estimated values of incoming radiation, as well as estimates of snowpack parameters like albedo, density, water content and thermal conductivity.

The DAISY model calculates temperature profiles within a layered snowpack based on input measurements of air temperature, relative humidity, wind speed, short wave radiation and long wave radiation. In addition to a description of the theory behind DAISY, Bader and Weilenmann (1992), present several hypothetical case studies in which DAISY was applied to examine the effects of rapid snowpack warming, melt-freeze cycles, forest cover and slope aspect on temperature profiles.

The computer models CROCUS (Brun et al., 1992) and SNOWPACK (Bartelt and Lehning, 2002), discussed in greater detail in Section 2.3, include the effects of snow microstructure on the surface energy balance. Because these models account for grain metamorphism and the layered structure of the snowpack, applicability to avalanche forecasting is better than for the aforementioned models. Aggarwal et al. (2006) describe the recent addition of grain microstructure and metamorphism routines to SNTHERM, another example of a physically based computer model that considers the layered nature of the snowpack and completes detailed surface energy balance calculations. Jordan (1991) provides a detailed description of the SNTHERM model.

Etchevers et al. (2004) summarize a comparison of surface energy balance simulations completed with 23 different models varying from complex, like CROCUS and SNOWPACK, to very simple. Results indicated that increased model complexity corresponded to better simulation of net long wave radiation fluxes. With respect to the net short wave radiation fluxes, however, model performance was dependent on accurate determination of the albedo; this was not necessarily a function of model complexity. Etchevers et al. (2004) note that, of the simple albedo parameterizations, those based on snow age seemed to work best during melt periods and those based on a constant value or on a relationship with snow surface temperature were more successful during non-melt periods.

Recent work by Staples et al. (2006) illustrates the potential for application of surface energy balance models over detailed digital terrain information. Snow surface temperatures were determined with the energy balance model Radtherm/RT, applied after incoming short and long wave radiation fluxes were adjusted at each grid point for surrounding terrain using a view factor approach. While limited field data were available for verification, and preliminary comparisons between measured and modelled snow surface temperatures show that further work is required, the approach used to adjust radiation fluxes shows promise. Modelling errors were attributed in part to coverage of the radiometers by snowfall and in part to the changing thermal properties of snow.

2.3 Snowpack evolution models

The following sections will expand on SNOWPACK and CROCUS, two well-developed computer models currently used in operational avalanche forecasting. To determine the energy balance at the snow surface, SNOWPACK and CROCUS require measured meteorological parameters as input. In addition, the calculations require estimation or calculation of parameters based on snowpack characteristics. Table 2.1 summarizes typical model input parameters.

Table 2.1: *Typical input parameters for snowpack evolution model surface energy balance calculations.*

	Model Input
Measured Meteorological Parameters	incoming short wave radiation incoming long wave radiation snow surface temperature (or measured outgoing long wave radiation) air temperature wind velocity precipitation (liquid water mass)
Estimated/ Calculated Snowpack Parameters	albedo short wave radiation extinction coefficient emissivity turbulent transfer coefficients effective snow conduction coefficient

Both models divide the snowpack into layers and apply energy and mass conservation equations to each layer. Energy exchanges are projected perpendicular to the slope, with energy transfer into the snowpack defined as positive.

2.3.1 CROCUS

CROCUS is a physically based computer model developed in France. The intent was to build upon early hydrological models and develop something that would, with measured meteorological data as input, model a layered snowpack and provide information useful for characterizing the mechanical properties of snow layers and for use in snowpack stability evaluation. Brun et al. (1992) describe incorporation of snowpack grain metamorphism into the CROCUS model.

For operational use, CROCUS is applied in conjunction with SAFRAN (a meteorological model) and MEPRA (an expert forecasting system) to forecast avalanche risk for different regions in the French Alps and Pyrenees (Durand et al., 1999). Each forecast region covers an area of approximately 500 square kilometres. Meteorological input for CROCUS is obtained from SAFRAN, which produces a large-scale weather forecast for each region. The resultant CROCUS output then consists of multiple snow profiles, determined for different aspect and slope angle combinations, which are meant to be typical of the entire forecast region.

2.3.2 SNOWPACK

The Swiss Federal Institute for Snow and Avalanche Research (SLF) developed SNOWPACK to produce useful snowpack information such as layering, grain types, densities and temperatures from meteorological input data. The model is currently in operational use by the Swiss avalanche warning service, as well as by several other European countries. More than eighty automatic weather stations in Switzerland provide data input for the SNOWPACK model (Lehning et al., 2002a). Forecasters use the snow stratigraphy modelled for each weather station location to supplement other information, like manual snow profile and avalanche observations, used in their stability analysis. In addition to this operational use, the model has been valuable in other areas of snow and avalanche research. Lehning et al. (2004) describe SNOWPACK applications in alpine ski run preparation, for runoff calculations and in climate change studies.

SNOWPACK considers snow as a three phase medium consisting of air, water and ice. The three phases are assumed to be at the same temperature. The model solves equations for conservation of mass, energy and momentum using a finite element method, typically on a time step of fifteen minutes. These equations reflect energy exchange, heat transfer, water flow and snow metamorphism within the snowpack. The model output includes settlement, density and snowpack temperatures. Metamorphism routines model changes in grain size and shape, and estimate bonding between grains. Precipitation values are determined from measurements of snow height and estimated settlement. Bartelt and Lehning (2002) and Lehning et al. (2002a, 2002b) provide a detailed description of the physical processes and calculations included in the SNOWPACK model.

The SNOWPACK model version used operationally does not use a separate term to define latent heat due to vapour diffusion within the pore spaces (Q_{mm}). This process is included with convective heat transfer by adjusting the effective conductivity. In determining effective conductivity, the model considers microscopic snow properties such as grain size and bonding in conjunction with macroscopic properties such as density. Adjustments are made to the effective conductivity in the uppermost layers of the snowpack to include additional convective heat fluxes due to wind pumping.

Bartelt and Lehning (2002) describe the two boundary conditions used to define the energy exchange at the snow surface. When snow surface measurements are available and well below freezing, the surface temperature is set to the measured value (Dirichlet boundary condition). A Neumann boundary condition comparable to Equation 2.1 is used when the snow surface temperature is either unknown or near 0 ºC.

$$k \cdot {}^{\mathrm{d}T}/_{\mathrm{dz}} = Q_{\mathrm{lw}} + Q_{\mathrm{s}} + Q_{\mathrm{l}} + Q_{\mathrm{p}} \tag{2.1}$$

where k = thermal conductivity (W/m·ºC)
${}^{\mathrm{d}T}/_{\mathrm{dz}}$ = temperature gradient in the z direction (ºC)
Q_{lw} = net long wave radiation flux (W/m^2)
Q_{s} = sensible turbulent heat flux (W/m^2)
Q_{l} = latent turbulent heat flux (W/m^2)
Q_{p} = heat flux from precipitation (W/m^2)

SNOWPACK can be run using measurements of either, or both, incoming or reflected short wave radiation (Spreitzhofer et al., 2006). Some stations collecting weather data are equipped with upward and downward-facing pyranometers to provide measurements of both incoming short wave radiation and that reflected off the snow surface. Reflected short wave radiation values are provided for operational use in Switzerland, as measurement errors resulting from snow cover on upward-facing sensors are avoided. Where measurements of both incoming and reflected short wave radiation are not available, an estimate of the snow albedo is required. The operational version of the SNOWPACK model uses empirical relationships between meteorological and snowpack parameters, which do not consider spectral variability, to determine the albedo and short wave radiation extinction coefficients.

Meirold-Mautner (2004) compared the model-derived extinction coefficient values with field measurements and found that SNOWPACK overestimated the extinction coefficient. His research resulted in proposed improvements to SNOWPACK's radiation calculations, which would consider both spectral variation in the short wave parameters and differences in scattering within the snowpack due to different grain shapes. Lehning et al. (2004) describe modifications to the original SNOWPACK model which included the addition of this spectrally resolved multiple scattering radiation transfer scheme.

Additional improvements to SNOWPACK described by Lehning et al. (2004) include calculation of several stability indices (both for natural and skier-triggered avalanches), incorporation of a soil modelling module and addition of a vegetation module. With input parameters such as canopy height, leaf area index and direct through fall fraction, the vegetation module includes the effects of tree cover by considering mass and energy balance at the tree canopy; heat fluxes due to radiation and turbulent exchange can both occur here. SNOWPACK then adjusts input values used in the snow surface mass and energy balance calculations, thus improving model performance in forested areas.

2.3.3 Verifying model output

In addition to limited availability of detailed meteorological data for model input, a drawback to computer models like SNOWPACK and CROCUS is the potential for errors when the model is applied in snowpack and weather conditions different from those for which it was initially developed. This is less of a problem where physically based equations define processes. If empirical equations characterize relationships between parameters, different conditions can be more of a concern and it is important to confirm the validity of the model output. Precise field measurements are required for refinement and verification of model output. Some examples of verification completed for the SNOWPACK model are provided below.

Bartelt and Lehning (2002) describe comparison of SNOWPACK model output to snowpack observations made in Switzerland during the winter of 1998-1999. Results of the comparison indicated that the model mass and energy balance equations worked well and provided reasonable estimations of layering and snowpack temperatures. Additional verification summarized by Lehning et al. (2002a) compared manual snow profiles to the model output with particular emphasis on the formation of crusts and surface hoar layers, which are very dependent on the surface energy balance. Model results compared favourably with observations, indicating accurate simulation of the surface energy balance calculations. The verification summary also noted that modelled snow temperatures and densities were typically in better agreement with observations than grain size and shape.

In the winter of 1999-2000, researchers ran the SNOWPACK model using meteorological information obtained from a weather station in the Bridger Mountains near Bozeman, Montana. Lundy et al. (2001) compared SNOWPACK output to measurements obtained from weekly manual snow profiles. The comparison indicated that the model was successful in predicting temperatures within the snowpack, although visual comparison of the measured and modelled temperature profiles indicated a decrease in accuracy near the snow surface.

For numerical measurements, like temperature, Lundy et al. (2001) used statistical parameters to quantitatively compare SNOWPACK output with field measurements. Hirashima et al. (2004) used the same statistical descriptors to evaluate SNOWPACK model performance for three sites in Hokkaido, Japan. Comparison of SNOWPACK output with the Japanese field data showed generally good agreement between modelled and observed grain type. Some discrepancies were noted relating to depth hoar and faceted grains that formed near the snow surface. These were attributed more to the simulation of grain metamorphism rather than the calculated near-surface temperature gradients, which were reproduced fairly well by SNOWPACK (Hirashima et al., 2004).

2.4 Measuring near-surface snow temperatures

The physical and optical properties of snow contribute to the challenge in obtaining accurate measurements of near-surface snow temperature. Placement of equipment within the snowpack disturbs the fragile snow structure, and settlement of measurement equipment relative to the snow is an issue in low density near-surface snow. Measurement errors occur because of differences in albedo and emissivity between the temperature measurement equipment and the snow. Most materials have lower albedo and emissivity than snow and, as a result, equipment tends to absorb more solar radiation and warm more than the actual snowpack. These solar heating errors are difficult to eliminate and to quantify.

To study the viability of a new snow surface temperature measurement method, Andreas (1986) compared surface temperatures measured with a thermistor and a thermocouple to values obtained with a dew-point hygrometer placed approximately 10 cm above the snow surface. The dew-point hygrometer, which operates on the assumption that the air just above the snow surface is in saturation with the snow, was mounted inside an aspirated radiation shield. Both the thermistor and thermocouple measured substantially warmer temperatures than the dew-point hygrometer at midday, corresponding with peaks in measured incoming solar radiation values. Differences ranged from 3 to 9 ºC and 4 to 11 ºC for the thermistor and thermocouple, respectively. Andreas (1986) does not comment on whether either the thermistor or thermocouple were coated to minimize absorption of short wave radiation.

Brandt and Warren (1993) presented results based on data measured with thermocouples (painted white to minimize solar contamination) placed at varying depths within the top 60 cm of the snowpack. After the array equilibrated, it was shaded from direct sunlight with a piece of plywood. Initial rapid cooling for approximately one minute was followed by a more gradual cooling trend. The initial cooling was attributed to removal of the incident short wave radiation absorbed by the thermocouples, while the subsequent gradual cooling was thought to reflect cooling of the snowpack itself. The magnitude of both cooling processes decreased with depth, with initial rapid temperature decreases of approximately 2.4 ºC at the snow surface and 0.2 ºC at 10 cm depth.

During a field study focused on the formation of near-surface facets, Birkeland et al. (1998) measured temperatures within the top 20 cm of the snowpack with an array of thermocouples mounted inside small diameter stainless steel tubes. They reported that increased heating of the thermocouples closest to the surface due to solar radiation absorption may have contributed to errors in the calculated temperature gradients. No discussion regarding quantification of these errors or potential means of mitigation was provided.

Glendinning and Morris (1999) made near-surface snow temperature measurements to compare with results of radiative transfer modelling. Modelling included several methods of differing complexity to determine temperatures within the top portion of the snowpack. Corresponding temperatures within the top metre of the snowpack were measured with an array of platinum resistance thermometers. No attempts to shade or coat the thermisters are noted in the paper and, in comparing the model results with the measured values, Glendinning and Morris (1999) suggest that differences between the measured and modelled values were enhanced by solar contamination and melting around the thermisters in the top 40 cm of the snowpack. Root mean square errors between the modelled and measured results were calculated to be approximately 6 ºC near the snowpack surface, decreasing to less than 2 ºC at 40 cm depth.

In Morstad's (2004) experimental chamber trials, an array of thermocouples measured snow sample temperatures at 1 cm increments from the surface to 10 cm depth, and at 5 cm increments from 15 to 40 cm depth. Each thermocouple sat inside a 1.2 mm diameter mylar-wrapped hermatocrit glass tube, with the tip extending slightly beyond the end of the tube. The equipment was painted with white acrylic paint. Errors in measured temperatures as a result of excess absorption of short wave radiation were quantified by turning the radiation source (metal halide lamp) off at the end of each experiment. Noticeable temperature changes near the top of the snowpack, which reached a maximum value of approximately 6 ºC in one trial, were observed just after turning the lamp off. This maximum temperature change corresponded with a measured temperature of +6 ºC at 3 cm depth, even though corresponding snow melt was not observed. The magnitude of solar contamination, which varied depending on the experimental chamber conditions and snow sample properties, decreased with depth and was typically not noticeable below depths of 5 to 10 cm.

CHAPTER THREE: FIELD METHODS

3.1 Study area

Field data were collected at Gopher Butte, a knoll located approximately 300 m northwest of the Mount Fidelity research station in Glacier National Park. This field location offered a tree line study site (approximately 1940 m) in close proximity to an automated weather station maintained by the Avalanche Control Section (ACS) of Parks Canada. The availability of meteorological data was necessary to undertake SNOWPACK model simulations.

Glacier National Park is located within the Columbia Mountains of British Columbia, Canada (Figure 3.1). Hägeli and McClung, (2003) describe this range as having a transitional snow climate with a strong maritime influence. A transitional or inter-continental snow climate displays both maritime and continental snowpack characteristics. Maritime regions usually receive heavy snowfall with relatively mild temperatures, while continental areas are typically colder with a thinner snowpack (McClung and Schaerer, 1993, p. 18). Average monthly snow depths measured at the Mount Fidelity study plot during the winters of 2005 and 2006 are given in Table 3.1.

Table 3.1: *Average monthly snow depth at Mount Fidelity.*

	Snow depth (cm)	
	2005	***2006***
January	210	197
February	265	259
March	273	268
April	285	249

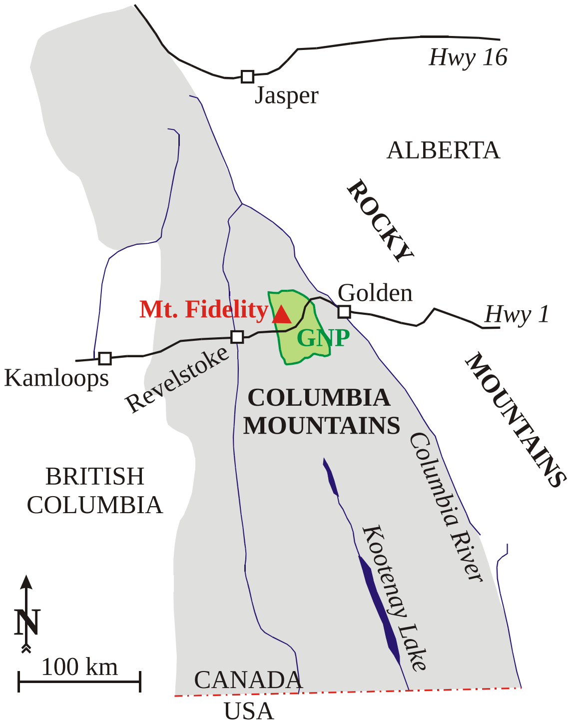

Figure 3.1: *Map showing the location of the study site at Mount Fidelity in Glacier National Park (GNP).*

Collection of field data on a knoll allowed for comparison of near-surface temperature data on different aspects. A field location in the vicinity of an automated weather station was required, as previously noted, to ensure that sufficient meteorological data were available as input for the SNOWPACK model. Gopher Butte knoll did fulfill this requirement, as well as being relatively easy to access with field equipment. The tree cover on Gopher Butte, however, limited selection of sites for measurement of near-surface temperatures. Sites without trees in close proximity were desired in order to minimize the effects of shading from direct incoming short wave radiation and increased long wave radiation emissions from trees on the surface energy balance. The west-facing knoll slopes have more tree cover than the relatively open east-facing slopes (Figure 3.2), resulting in less data collected on west-facing slopes.

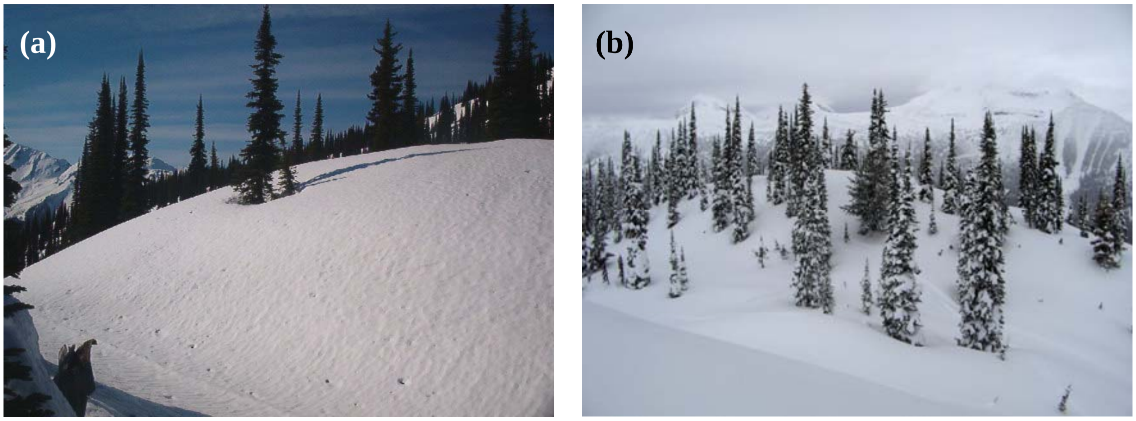

Figure 3.2: *Photographs of Gopher Butte showing tree cover on the (a) east- and (b) west-facing knoll slopes (photos: ASARC).*

3.2 Equipment

3.2.1 Meteorological measurements

The ACS provided hourly air temperature, precipitation and relative humidity measurements from the Mount Fidelity study plot. Incoming short and long wave radiation measurements were collected with a pair of radiometers on loan from the University of British Columbia Avalanche Research Group. The Eppley Precision Spectral Pyranometer and Precision Infrared Radiometer were mounted facing upwards on a tower in the study plot. Both instruments were continuously ventilated with AC power. Accumulated snow, if any, was manually removed by the ACS, who visit the study plot on a near-daily basis. Applied Snow and Avalanche Research at the University of Calgary (ASARC) maintains an RM Young Wind Monitor, mounted on the same tower, which provided hourly measurements of wind direction and wind speed in the study plot.

3.2.2 Near-surface temperatures

Near-surface temperatures were measured in the field with arrays of thermocouples constructed from AWG 30, type K (chromel-alumel) thermocouple wire with Teflon Neoflon insulation. The thermocouples had a standard limits of error designation of the greater of 2.2 ºC or 0.75% of the measured temperature (Omega Engineering Inc., 2004). After cutting the thermocouple wire into desired lengths, the bare wire ends were twisted together and passed briefly through an acetylene torch flame to create a good contact bead.

Balsa wood sections were constructed to place and hold the thermocouple wires. Requirements for a light material with thermal properties somewhat similar to snow lead to the selection of balsa wood for construction of the sections. Male and Gray (1981) quote 50 to 65 kg/m^3 for the density of newly deposited snow falling in still air. Snow density can increase rapidly after deposition, particularly if wind is present. Values of 70 to 90 kg/m^3 and 280 kg/m^3 are quoted for settling snow and average wind-toughened snow, respectively (Male and Gray, 1981). Standard density balsa wood has a typical density of 155 kg/m^3 and thermal conductivity of 0.063 W/mºC (Balsa Sales Ltd., 2003). For comparison, applying the model of Sturm et al. (1997) results in an effective conductivity of 0.059 W/mºC for snow with a density of 155 kg/m^3. Holes were punched in the balsa wood sections to further reduce their weight.

The balsa wood sections were painted with white acrylic spray paint in an attempt to mimic the highly reflective properties of snow and to minimize absorption of incoming short wave radiation by the temperature measurement equipment. A single thermocouple was glued to the underside of each section prior to painting.

Two different section designs were used during the course of this project. For the winter of 2005, the sections were constructed of 50.8 mm by 1.6 mm (2" by $^1/_{16}$") balsa wood strips (Figure 3.3) glued to a 3.2 mm ($^1/_8$") square balsa wood backbone to form an inverted angle section. The thermocouple tips were set slightly under the end of each section so as not to be exposed directly to incoming short wave radiation. The average density of a painted section (without thermocouple attached) was approximately 150 kg/m^3.

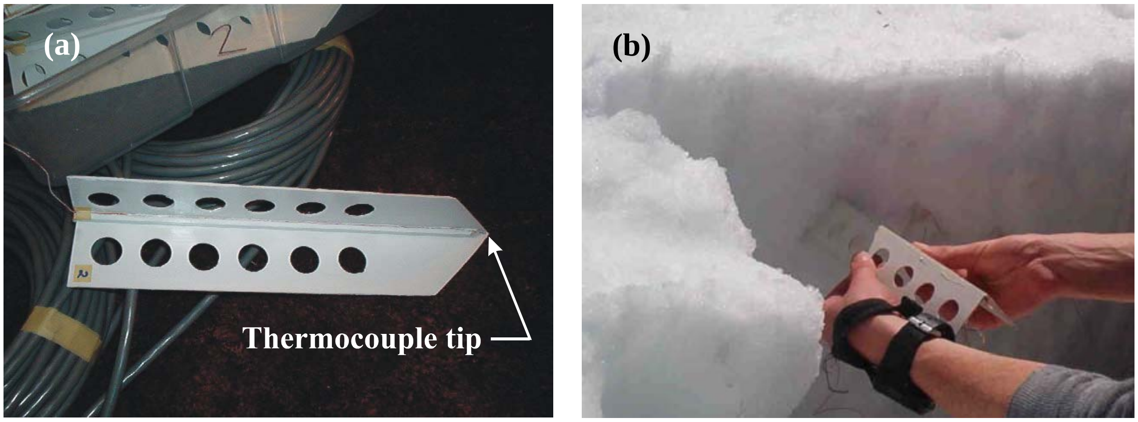

Figure 3.3: *Photographs of balsa wood sections used to place and hold thermocouples during 2005 field experiments: (a) thermocouple attached to the underside of a painted balsa wood cover and (b) placement in the field (photos: ASARC).*

The sections were extremely fragile and difficult to place when the snow was dense or crusts were present. A metal cutter was used in these instances to pre-cut the snow before inserting the thermocouples at the desired location. This helped to minimize breakage of the balsa wood sections during placement. The guiding template used to assist with placement was removed before each array was backfilled.

Data collected during the winter of 2005 showed that above-zero temperatures were measured in the top portion of the snowpack even when melting was not observed.

Despite steps taken to match the properties of the measurement equipment to the snow, differences in the absorption and emission characteristics of the equipment contributed to the temperature measurement errors. Design modifications were made to the balsa wood sections for the winter of 2006 to improve the ease of construction, longevity and placement accuracy of the thermocouples. It was hoped that the changes would also reduce the magnitude of temperature measurement errors.

The sections used in 2006 were constructed of 9.5 mm ($^{3}/_{8}$") triangular balsa wood sections (Figure 3.4(a) and (b)). The thermocouple tips extended just beyond the end of each section, which was bevelled to minimize snow compaction during placement. Two Ethafoam blocks, which have a typical density of 36 kg/m^3 and thermal conductivity

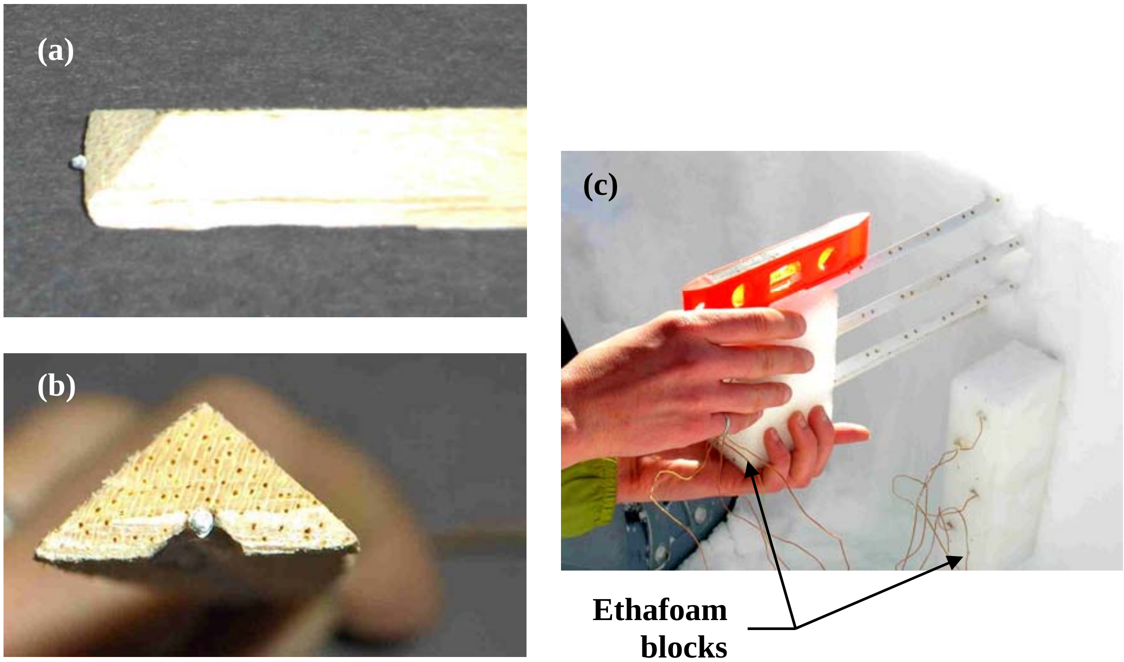

Figure 3.4: *Photographs of balsa wood sections used to place and hold thermocouples during 2006 field experiments: (a) side and (b) end views of thermocouple attached to the underside of a balsa wood cover (equipment has not yet been painted) and (c) placement in the field (photos: ASARC).*

of 0.05 W/mºC (Dow Chemical Company, 2002), were used with each array to assist with placement (Figure 3.4(c)). These were backfilled in place during each experiment.

Each array consisted of 10 thermocouples placed within the top portion of the snowpack at approximate depths of 2, 4, 6, 8, 11, 14, 18, 22, 27 and 32 cm. Field staff used a guiding template to assist in placing the thermocouples at the desired depths and had a second team member 'eyeball' the thermocouples for straightness during insertion to improve placement accuracy. Four AMT25 multiplexers (one for each array) connected to a single CR10X datalogger allowed for sufficient data inputs and placement of the thermocouple arrays at different locations while minimizing the individual thermocouple lengths (approximately 1.0 to 1.6 m). Based on thermocouple measurements made at 30 (2005) or 60 (2006) second intervals, the datalogger recorded average temperature values every 10 (2005) or 15 (2006) minutes.

Thermocouples were calibrated several times during each field season, using a snow/water slurry to provide a reference temperature. Field thermocouple measurements were adjusted using the thermocouple-specific offset from 0 ºC measured during the most recent calibration session. Table 3.2 summarizes the values measured during calibration. At the end of the 2006 winter season, the thermocouples were calibrated using an ice/water mixture made with distilled water. Offsets from 0 ºC were similar to those measured previously with the snow/water slurry.

Table 3.2: *Temperatures measured during thermocouple calibration*.

	Minimum	**Average**	**Maximum**
2005	-0.08 ºC	-0.03 ºC	0.09 ºC
2006	-0.28 ºC	-0.15 ºC	0.05 ºC

3.2.3 Surface temperature

A Testo 825-T4 infrared thermometer was used to manually measure snow surface temperature at periodic intervals during each field experiment (Figure 3.5). An infrared thermometer measures the amount of long wave radiation emitted from a surface and, given an emissivity value, converts the emitted long wave into temperature. Unlike a traditional thermometer, an infrared thermometer does not skew measurements by absorbing excess short wave radiation. The thermometer used had a resolution of 0.5 ºC and accuracy of ±2 ºC in the temperature range of interest. The adjustable emissivity was set to 0.99 during the field experiments.

Figure 3.5: *Testo 825-T4 infrared thermometer used to make manual measurements of snow surface temperature at each array site (photo: ASARC).*

At times, field staff noticed unexpected variations and substantial drift in the infrared temperature measurements. The temperature of the instrument itself appeared to have a significant effect on the measured value (i.e. colder measured temperatures when the thermometer body was warm and warmer measured temperatures when the thermometer body was cold). Several tests undertaken to confirm these observations also indicated that the measured values drifted more when the thermometer temperature differed substantially from the ambient air temperature. For consistency, the infrared thermometer was allowed to equilibrate to the outside air temperature before each measurement was taken, and measurements were taken at each location until the same value was obtained for three successive measurements. While taking measurements, the infrared thermometer was held perpendicular to the snow surface at an approximate distance of 15 cm. This corresponds to a circular measurement area with diameter of approximately 5 cm (diameter equal to one-third of the distance between the thermometer and the surface).

3.3 Field procedure

For each field experiment, four thermocouple arrays were set up to measure near-surface snowpack temperatures. One array was placed at a flat location on the knoll top and the remaining three were placed in undisturbed areas on varying aspects, as shown schematically in Figure 3.6. To maintain measurement depths close to the snow surface and reduce difficulties in tracking thermocouple depths, the field equipment was only set up during periods without forecast precipitation. Data were collected under a variety of different cloud cover conditions.

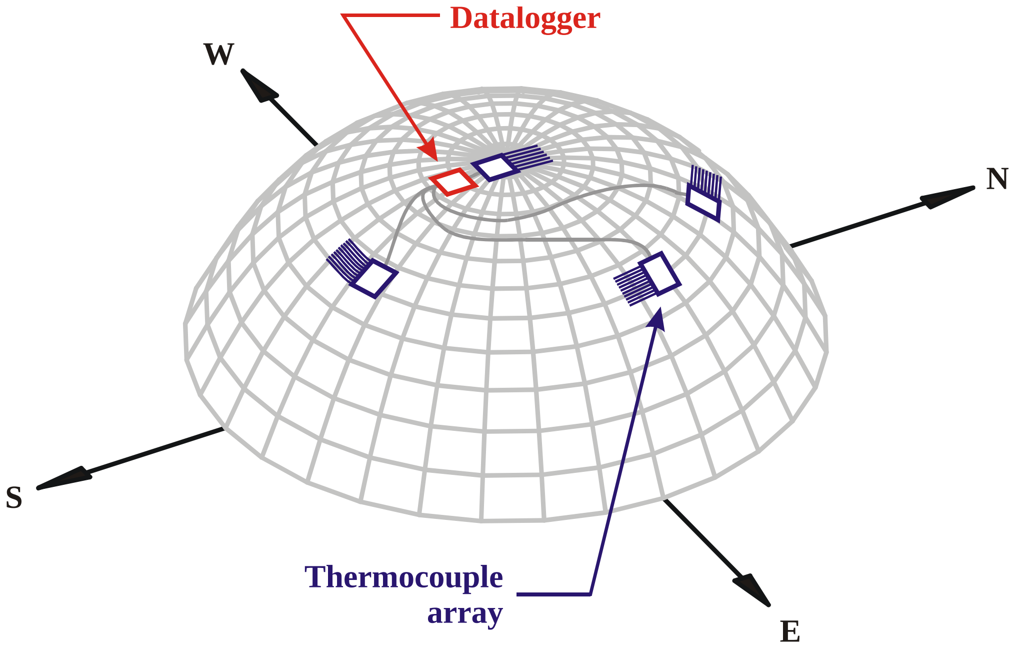

Figure 3.6: *Schematic illustration showing typical array placement. Knoll slope arrays were placed on different aspects for each field experiment.*

At each array location, the aspect and slope angle were recorded and a shallow pit (approximately 40 cm deep) was dug to allow placement of the thermocouples. Following insertion of the thermocouples at the desired depths using the guiding template or foam block, the multiplexer was connected to the datalogger, placed in the pit and backfilled with snow to minimize temperature fluctuations. Once all four arrays were installed, the datalogger battery was connected and temperature recording commenced.

Through the day, manual measurements of air temperature and infrared snow surface temperature were made for each array at approximately hourly intervals. Observations of cloud cover, estimated wind speed and snow surface condition (i.e. sunny or shaded) were also recorded. This information was collected at four hour intervals overnight for the experiments run in the winter of 2005.

Each field experiment ran for a period of 1 to 6 days (2 days was typical), after which the data was downloaded and the datalogger disconnected. The exact depth from the snow surface to each thermocouple tip (perpendicular to the slope) was measured after carefully digging out the tip end of each thermocouple array. Field staff took photographs at each array location at setup, throughout each experiment and during removal of the thermocouples.

Near the beginning of each measurement period, a shallow snow profile (approximately 40 cm deep) was completed in an undisturbed area representative of each array site. Following procedures outlined in the Canadian Avalanche Association Observation Guidelines and Recording Standards (CAA, 2002, 14-19), layers within the top portion of the snowpack were identified. For each layer, data recorded included the hand hardness, crystal form, crystal size, moisture content and density. Observations included the surface crystal size and form. For many of the experiments, snow profile observations were also made near the end of the data collection period.

3.4 Field data summary

Near-surface temperatures were measured over eleven different time periods in February, March and April of 2005 and 2006. A summary of the field data is provided in Table 3.3 and Figure 3.7.

Table 3.3: *Summary of field data collected in the winters of 2005 and 2006.*

Start date	Start time (PST)	Total hours	Daily average sky condition *	Array	Aspect	Slope
27-Feb-05	1310	35	CLR, FEW	*1*	TOP	0
				2	S (162)	12
				3	NE (63)	17
				4	NE (32)	17
10-Mar-05	1250	20	SCT	*1*	TOP	0
				2	SW (210)	20
				3	E (88)	22
				4	NE (39)	19
13-Mar-05	1140	46	FEW	*1*	TOP	4
				2	S (180)	9
				3	N (7)	10
				4	E (100)	14
25-Apr-05	1115	25	CLR, FEW	*1*	TOP	0
				2	S (172)	11
				3	N (2)	11
				4	E (96)	11
6-Feb-06	1100	148	CLR, FEW, SCT, BKN, OVC	*1*	TOP	2
				2	S (164)	14
				3	E (86)	21
				4	N (5)	15
18-Feb-06	1215	49	FEW, BKN, OVC	*1*	TOP	4
				2	SW (212)	23
				3	E (108)	20
				4	NE (41)	19
4-Mar-06	1230	26	FEW, BKN	*1*	TOP	2
				2	SW (216)	32
				3	SE (116)	23
				4	NE (43)	19
27-Mar-06	1015	47	BKN, OVC	*1*	TOP	3
				2	S (168)	12
				3	E (80)	19
				4	NW (336)	15
29-Mar-06	1115	48	BKN	*1*	TOP	3
				2	SW (213)	27
				3	SE (114)	21
				4	NE (48)	19
3-Apr-06	1145	50	SCT, BKN, OVC	*1*	TOP	3
				2	SW (204)	20
				3	E (91)	21
				4	NE (35)	20
21-Apr-06	1145	52	CLR, BKN, X	*1*	TOP	0
				2	E (96)	22
				3	TOP	0
				4	W (264)	22

* *Definitions for sky condition codes are provided in Table B.1, Section B.1.1.*

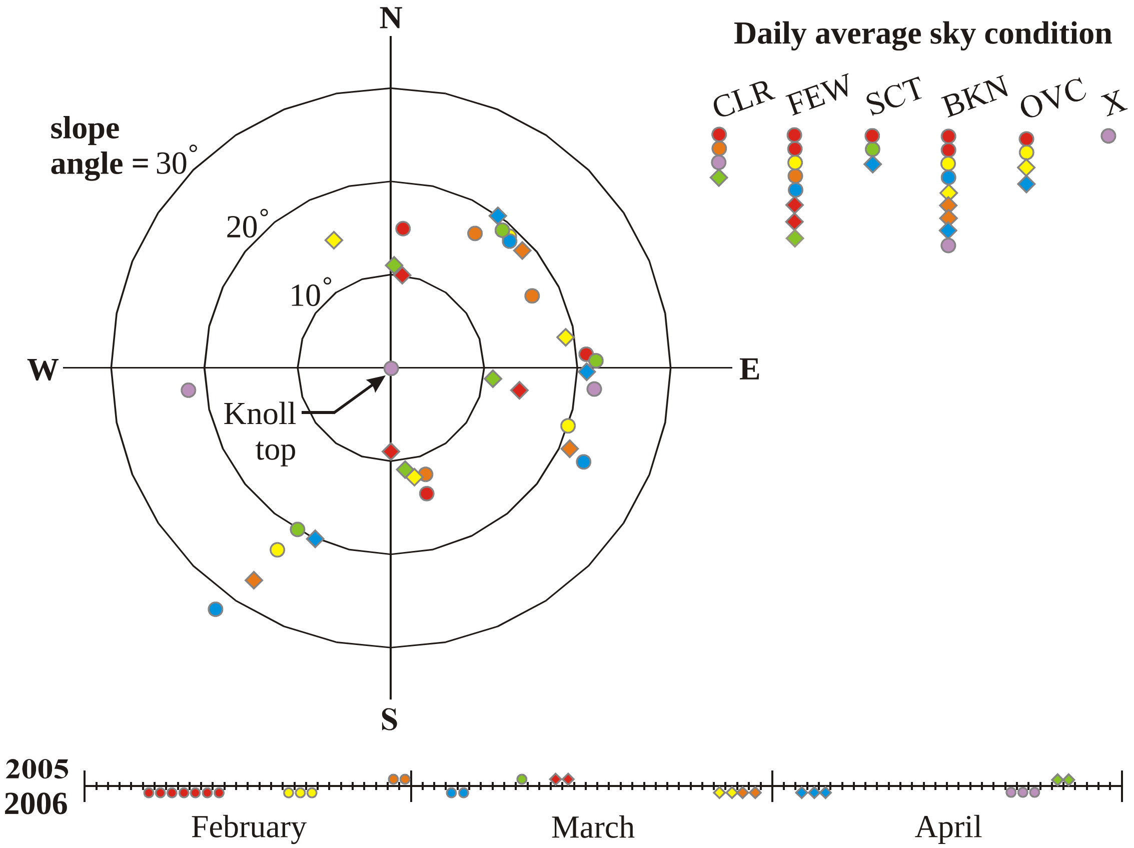

Figure 3.7: *Graphical summary of field data collected in the winters of 2005 and 2006. Note that each field experiment included a knoll top array. Definitions for sky condition codes are provided in Table B.1, Section B.1.1.*

CHAPTER FOUR: FIELD DATA EXAMPLES

Field data examples are presented in the following sections to illustrate measured variations in near-surface temperature changes due to differences in terrain, snowpack characteristics, weather and time of year. Focus is placed on daytime warming (ΔT_d), the parameter chosen in this study to represent temperature fluctuations in the upper portion of the snowpack. Here, daytime warming refers to the difference, at depth *d*, between the temperature at sunrise and the maximum afternoon temperature (Figure 4.1).

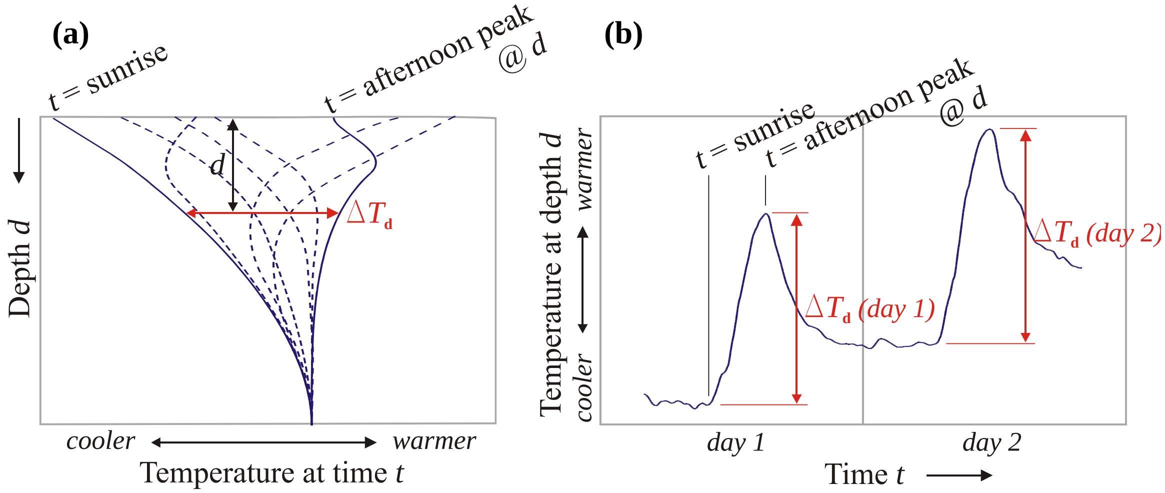

Figure 4.1: *Illustration of typical daytime warming (ΔT_d) relative to (a) temperature profiles at different times t, and (b) plot of temperature, at specific depth d, over time.*

4.1 28 February 2005

Of interest from the first of the eleven field experiments is a comparison between near-surface temperatures measured on an east-northeast-facing slope (ENE, 063º) and those measured on a north-northeast-facing slope (NNE, 032º). Both array sites were relatively open, with the same slope angle of 17º. No nearby terrain features were directly opposite either array location. Sky conditions over the two day period varied from clear skies to a few clouds.

Figure 4.2 illustrates the temperatures measured at different depths below the snow surface for these two arrays. It is evident that temperatures were warmer on the

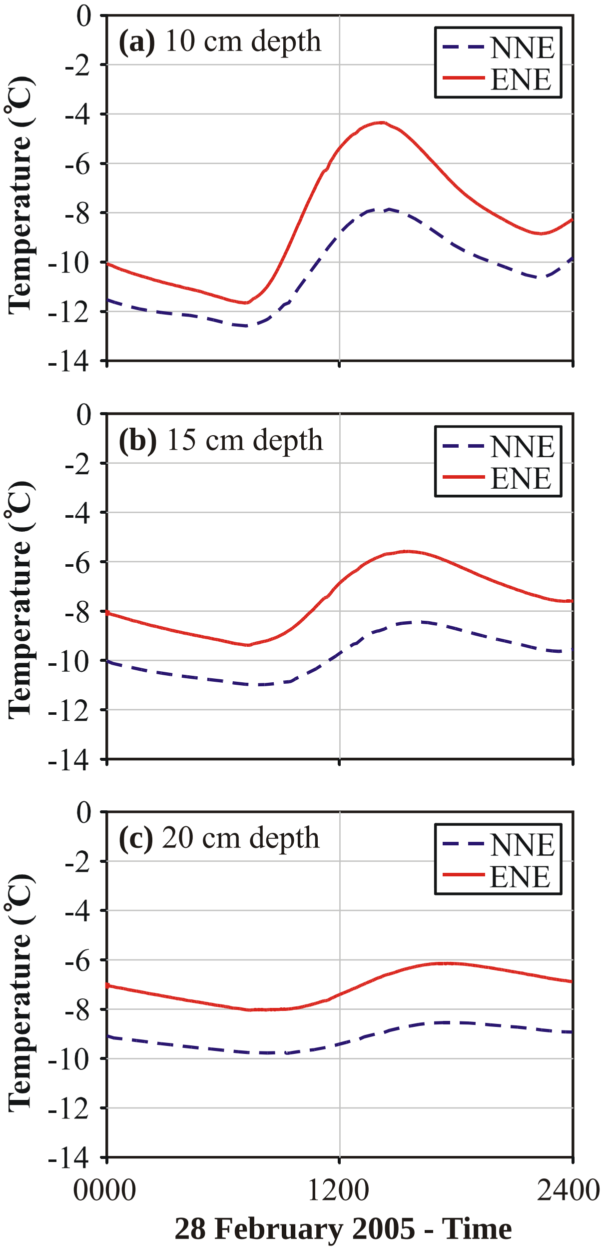

Figure 4.2: *Temperature measurements made at north-northeast (*NNE*) and east-northeast (*ENE*) array locations on 28 February 2005: (a) 10 cm, (b) 15 cm, and (c) 20 cm depth.*

ENE slope, with a greater difference between array sites at midday than overnight. The magnitude of daytime warming on the ENE slope was also greater than that measured on the NNE slope. Daytime fluctuations in near-surface temperature are primarily the result of the changing balance between short and long wave radiation fluxes at the snow surface (McClung and Schaerer, 1993, p. 33) and, as expected, they decreased in magnitude with depth. Table 4.1 summarizes the daytime warming measurements made at each array site.

Table 4.1: *Daytime warming* (ΔT_d) *measured at east-northeast (*ENE*) and north-northeast (*NNE*) array sites on 28 February 2005.*

Depth (cm)	**Daytime warming (ºC)** *ENE*	*NNE*
10	7.3	4.7
15	3.8	2.5
20	1.9	1.2

While slightly warmer temperatures on a more easterly-facing slope are not surprising, the magnitude of the temperature difference, considering the relatively small change in aspect, is worth noting. Estimates based on the methods outlined in Section B.1.1 show that, in late February under clear skies, the NNE array location would receive approximately 80% of the short wave radiation incident on the ENE slope.

A secondary factor which may have contributed to the temperature differences is related to the snowpack structure at each site. Manual snow profiles completed on the morning of 28 February 2005 showed surface hoar crystals on the surface and a combination of decomposing fragments and mixed forms to a depth of 20 cm at both array locations. The main difference between the two profiles was in the hand hardness, which is a qualitative scale used during manual snow profile observations to provide a measure of layer hardness. As outlined in the CAA Observation Guidelines and Recording Standards (CAA, 2002, p. 15), the observer records which of the following objects can be pushed into each snow layer, parallel to the layer boundaries, with moderate effort: fist in glove (F), four fingers in glove (4F), one finger in glove (1F), blunt end of pencil (P) or knife blade (K). If the layer is too hard to insert a knife, ice (I) is recorded.

As shown in Figure 4.3, slightly higher hand hardness values were recorded in the top 10 cm of the snowpack at the NNE array location; this suggests slightly higher density snow (Geldsetzer and Jamieson, 2001a) and therefore greater attenuation of short wave radiation (Bohren and Barkstrom, 1974) at this location. Higher density is also indicative of greater conductivity (Sturm et al., 1997). In addition to its effects on surface energy balance inputs, aspect may also have influenced near-surface temperatures through its effects on snowpack characteristics. Examples are spatially variable snowpack properties due to previous aspect-dependent differences in the surface energy balance or in exposure to wind.

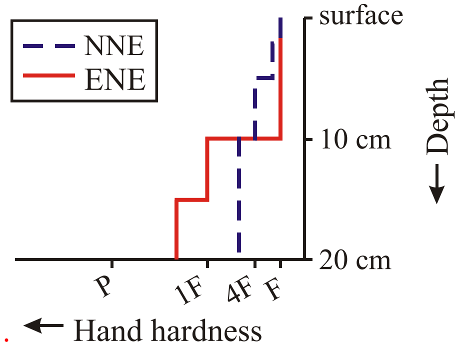

Figure 4.3: *Hand hardness observations made at north-northeast (*NNE*) and east-northeast (*ENE*) array locations on the morning of 28 February 2005.*

4.2 7-12 February 2006

The longest field experiment, spanning six days in early February 2006, included data collected under a variety of cloud cover conditions. Figure 4.4(a) illustrates the temperatures measured at 10 cm depth for arrays on the knoll top, north, east and south-facing slopes. A representative sky condition observation is given for each day, using data codes as defined in the Canadian Avalanche Association Observation Guidelines and Recording Standards (CAA, 2002, p. 2). Definitions for each data code are provided in Table B.1, Section B.1.1. Incoming short and long wave radiation data for 7-12 February 2006 were measured in the Mount Fidelity study plot and are plotted in Figure 4.4(b). The average daytime air temperature, which was approximately -5 ºC during most of the experiment, dropped to about -10 ºC on the 9th and 10th.

On an overcast day, 8 February, the measured snow temperatures did not vary much with aspect. At a depth of 10 cm, there was a difference of only one degree in the magnitude of daytime warming measured at each array location. In comparison, the aspect-dependent differences in near-surface temperature on a clear day, 11 February, were larger. Not only was there substantial variation in the peak afternoon temperature, but also in the magnitude of daytime warming. On 11 February, the greatest daytime warming value at 10 cm was measured as 10.8 ºC at the south-facing array site. This is almost 7 ºC greater than the corresponding value measured on the north-facing slope. The difference in daytime warming between aspects decreased to approximately 2 ºC at 20 cm depth. Table 4.2 presents a summary of the aspect-dependent differences in daytime warming measured on 8 and 11 February. On the overcast day (8 February) the highest and lowest daytime warming values were measured on the north and east slopes, respectively.

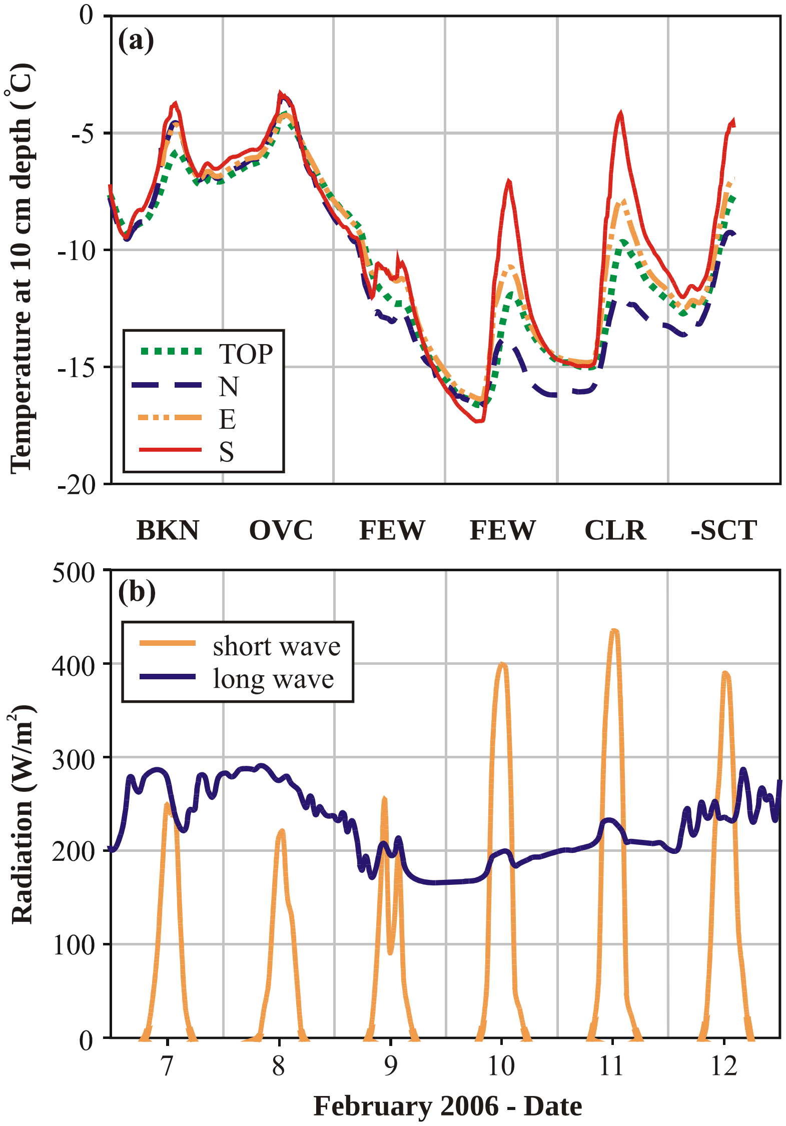

Figure 4.4: *Field measurements made on 7-12 February 2006: (a) temperature at 10 cm depth at four array locations, (b) short wave and long wave radiation incident on a horizontal plane in the Mount Fidelity study plot. A representative sky condition observation is given for each day (Table B.1, Section B.1.1). The dash (i.e. -SCT) indicates thin cloud.*

Table 4.2: *Maximum difference in daytime warming* (ΔT_d) *between aspects measured on an overcast day (8 February 2006) and a clear day (11 February 2006).*

Depth (cm)	**Maximum difference in daytime warming between aspects (°C)**	
	8 February 2006 (OVC)	***11 February 2006 (CLR)***
10	1.0	6.9
15	0.4	3.0
20	0.3	1.8

With the exception of the temperature measurements made on 9 February, where a considerable drop in air temperature and a midday incoming short wave radiation 'blip' complicate the interpretation, a similar relationship between cloud cover and differences in daytime warming was observed throughout this measurement period. Days with broken or overcast cloud cover showed less aspect-dependent differences in daytime warming than days with few clouds or clear skies. With little cloud cover, the proportion of direct short wave radiation is high and slopes facing the sun receive more short wave radiation than those with less exposure due to orientation or shading by surrounding terrain. Diffuse incoming short wave radiation is distributed more evenly over terrain, consistent with observations of less variation in daytime warming as scattering increased with cloud cover.

An additional point to note is the difference between incoming long wave radiation on 10 February, a day with few clouds, and 12 February, a day with thin scattered cloud. Increased cloud cover on 12 February corresponded with an increase in incoming long wave radiation. At the same time, however, there was very little decrease in incoming short wave radiation, as much of it was able to penetrate the thin cloud.

Under these thin cloud conditions, near-surface warming received relatively strong contributions from both short and long wave radiation fluxes.

4.3 10 February 2006 and 14 March 2005

To look at temporal changes in the spatial distribution of daytime warming, data from 10 February 2006 and 14 March 2005 were compared. On both of these days, arrays were set up on north, east and south-facing slopes as well as the knoll top. Corresponding array sites were within 7º in slope angle and 16º in azimuth. The sky conditions differed slightly, with few thin clouds present throughout 10 February and few clouds increasing to scattered clouds on the afternoon of 14 March. The average daytime air temperatures were -10 ºC and -1 ºC for 10 February and 14 March, respectively. Average relative humidity values were 66% on 10 February 2006 and 55% on 14 March 2005.

Measured temperatures at 10 cm depth and incoming short wave radiation values are plotted in Figure 4.5; short wave radiation values measured in the Mount Fidelity study plot have been projected for each array location (Section B.1.1). Note that the slight differences in terrain characteristics and cloud cover mentioned above are considered in the calculations done to project the study plot measurements of incoming short wave radiation from a horizontal plane to each array slope. Figure 4.5(a) indicates that, on both days, the warmest daytime temperatures at 10 cm depth occurred on the south-facing slope, with successively cooler temperatures measured on the east-facing slope, knoll top and north-facing slope. The incoming short wave radiation values show similar trends (Figure 4.5(b)).

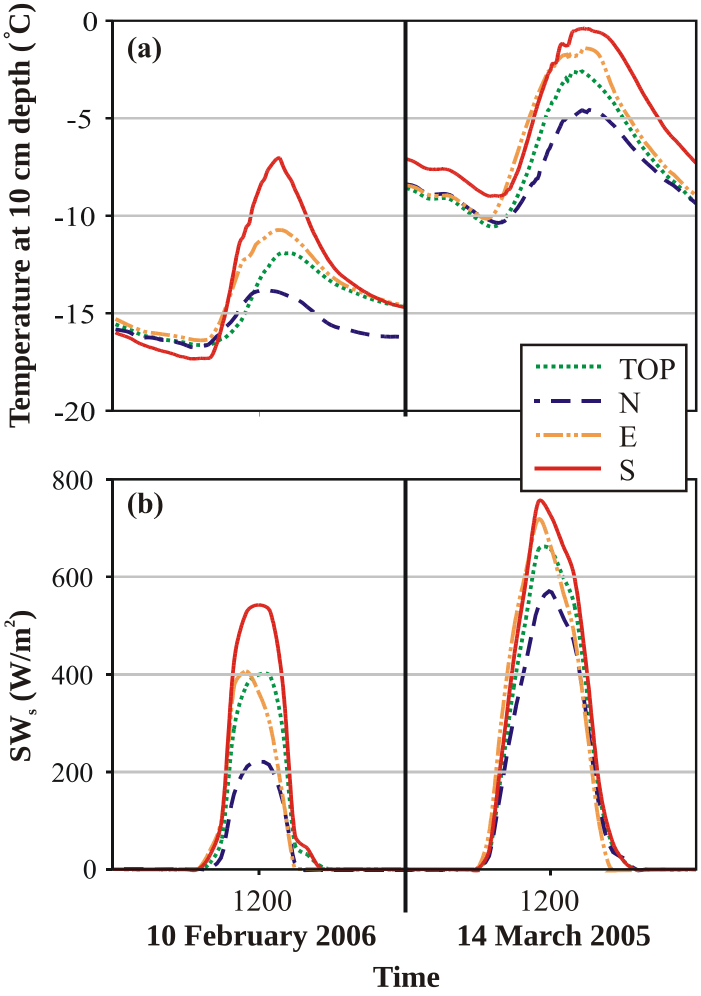

Figure 4.5: *Field measurements made on 10 February 2006 and 14 March 2005: (a) temperature at 10 cm depth, (b) incident short wave radiation on each array slope* (SW_S) *projected from horizontal measurements made in the Mount Fidelity study plot.*

In comparing daytime warming at each array site, we note an increase of approximately 2.5-3 ºC from February to March for the knoll top, north, and east arrays. On the south-facing slope, however, the magnitude of daytime warming actually decreased by approximately 2 ºC (Table 4.3). The data from 14 March also show slightly more daytime warming at 10 cm depth on the east-facing slope than on the south; the midday temperature values remained higher on the south-facing slope because the early morning temperatures were approximately 1 ºC warmer than those measured at the east array location.

Table 4.3: *Daytime warming at 10 cm depth* (ΔT_{10}) *measured on 10 February 2006 and 14 March 2005.*

Aspect	**Daytime warming (ºC)**	
	10 February 2006	***14 March 2005***
TOP	4.7	7.7
N	2.9	5.4
E	5.7	8.6
S	10.3	8.3

The daytime warming results are not consistent with the incoming short wave radiation trends noted above. Variability in the characteristics of the surface snowpack layers, which has not yet been considered in this discussion, is again a possible explanation for the apparent contradiction. Differences in albedo and extinction coefficient may have altered the amount of short wave radiation reaching 10 cm below the snow surface and thus the magnitude of daytime warming at depth.

Figure 4.6 presents the data in a different format. Measured values of daytime warming at 10 cm depth and maximum incoming short wave radiation (projected to each array location) are shown relative to the corresponding knoll top measurement. For both parameters, data from 10 February show greater variability between aspects than the data from 14 March. This is consistent with the expectation that, as the sun becomes higher in the sky, differences in exposure to direct short wave radiation would tend to decrease. Male and Gray (1981) note that the influence of orientation on daily incoming short wave radiation decreases closer to the summer solstice. The measured daytime warming values

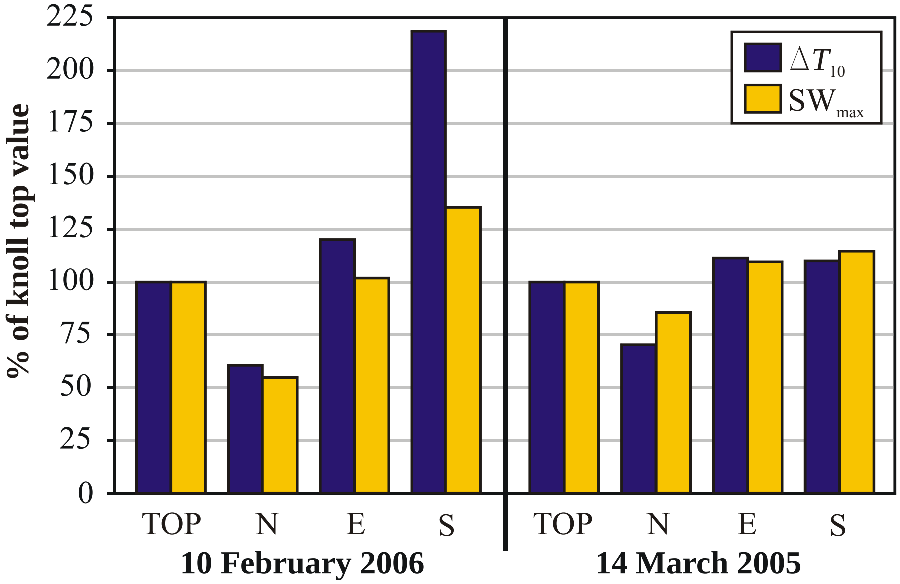

Figure 4.6: *Comparison of measured daytime warming at 10 cm (ΔT_{10}) and maximum incoming short wave radiation (SW_{max}) at each array location on 10 February 2006 and 14 March 2006. Values are relative to the corresponding knoll top measurement.*

on the east and south-facing slopes, particularly, were very similar on 14 March, corresponding with short wave radiation values that were also very alike.

Data collected on 10 February 2006 show greater between-aspect variability in daytime warming than in maximum incoming short wave radiation. Better agreement in the distribution of these two parameters over terrain is seen in the 14 March 2005 data. Again, spatial variability of the top snowpack layer properties is a possible explanation.

Manual snow profile observations made on 13 and 14 March 2005 showed a mixture of faceting decomposed fragments and thin melt-freeze crusts in the top 10 cm at all array locations. Because the upper snowpack consisted of many thin layers, field density measurements were not made. Manual profiles completed on 10 and 11 February 2006 indicated surface hoar on the snow surface at all array locations. The top 10 cm of the snowpack consisted of decomposing fragments and mixed forms (faceting rounds), in different proportions, at each array site. Density measurements made on 11 February 2006 at the north, east and south array locations indicated similar average densities within the top 10 cm of the snowpack

Estimation of the short wave radiation extinction coefficient is difficult for the thin layers observed on 13 and 14 March. As noted in Section 1.5.1, attenuation of short wave radiation is a function of the snow crystal characteristics in the upper snowpack layers. An extinction coefficient parameterization based solely on a linear relationship with snow density, like that outlined in Section B.2.2, is simple to apply, but perhaps not applicable for melt-freeze crusts. An average of melt-freeze crust densities provided by Geldsetzer and Jamieson (2001a) suggests that 292 kg/m^3 is a reasonable approximation. With a linear extinction coefficient parameterization, this results in a relatively high extinction coefficient value; literature values reported for ice (i.e. approximately 10 m^{-1} as cited by Mellor (1977) for bubbly ice) indicate that a lower value may be appropriate for a melt-freeze crust. The lack of field density measurements for the thin layers introduces additional uncertainty, as these values must also be estimated.

Because calculation of the short wave radiation flux at depth is sensitive to the extinction coefficient and this value cannot be determined with confidence, a comparison of the aspect-dependent distribution of short wave radiation at depth is not presented. The properties of the upper snowpack layers may have contributed to the observed aspect-dependent variations in daytime warming; noted differences between measurements made on 14 March 2005 and 10 February 2006 may also have resulted from changes in the spatial variability in these snowpack properties over time.

4.4 5 March and 30 March 2006

Field experiments completed on 5 March and 30 March 2006 included measurements made on southeast and southwest-facing slopes. The southwest-facing array sites were within 5º in slope angle and 3º in azimuth, while the southeast-facing sites differed by only 2º in both slope angle and aspect. Cloud cover observations showed variable cloud (broken to overcast) on both days, although thin cloud is noted throughout 5 March.

Table 4.4 summarizes the daytime warming measurements. On both days, the magnitude of daytime warming measured on the southeast-facing slope was greater than that measured on the southwest-facing slope. This is an interesting result for several reasons. First, the actual array locations were such that the southwest array sites (azimuth approximately 215º) were more southerly than the southeast array sites (azimuth approximately 115º). This would suggest that the southwest sites received more incoming short wave radiation. Second, in both experiments the southwest arrays were also located on steeper slopes than the southeast arrays. The difference in slope angle between array sites was approximately 9º on 5 March 2006 and approximately 6º on 30 March. Steeper slope angles also suggest that the southwest sites received more incoming short wave radiation.

Table 4.4: *Daytime warming at 10 cm depth* (ΔT_{10}) *measured on 5 March 2006 and 30 March 2006.*

Aspect	**Daytime warming (ºC)**	
	5 March 2006	***30 March 2006***
SW	8.4	3.2
SE	9.4	5.7 *

* *Measured temperature reached 0 ºC at midday.*

As noted in Section 3.1, tree cover is heavier on the west-facing slopes of Gopher Butte knoll than on the east-facing slopes. The effect of tree cover on the net radiation balance at the snow surface is variable (Section 2.1.4); shading of the snow surface from direct short wave radiation is offset by increased emission of long wave radiation by the trees. The relative magnitudes of these two processes will vary and result in either warming or cooling of the snow surface. The southwest-facing slope also has nearer opposite terrain than the southeast-facing slope, perhaps resulting in further differences in incoming short and long wave radiation.

Manual observations showed thin crusts present in the top 10 cm of the snowpack for both profiles on the southwest-facing slope. No crusts were observed in either southeast profile, although a thin layer of melt-freeze polycrystals was present at approximately 7 cm depth on 30 March. As discussed in the previous section, difficulty estimating appropriate short wave radiation extinction coefficients for thin melt-freeze crust layers limits convincing analysis of short wave radiation penetration at 10 cm depth.

Variable cloud cover over the day provides the best explanation for the measured differences in daytime warming. Incoming short wave radiation values were projected to each array slope from the hourly values measured in the Mount Fidelity study plot (Section B.1.1) and are plotted in Figure 4.7. The split of global incoming short wave radiation into direct and diffuse components was based on hourly manual cloud cover observations made from 0800 to 1500 on each measurement day.

On 5 March 2006, incoming short wave radiation was quite similar at both sites. This is consistent with a small difference in measured daytime warming. While the maximum incoming short wave radiation value was slightly greater on the southwest-

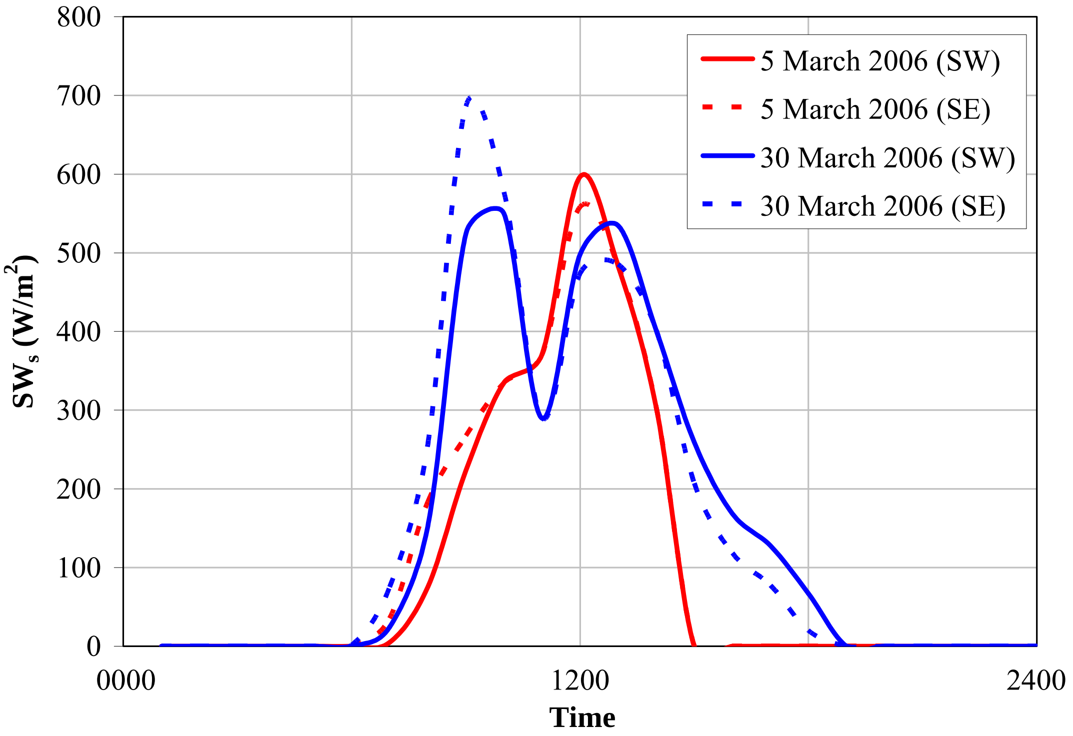

Figure 4.7: *Comparison of incident short wave radiation (*SW_s*) for southeast (*SE*) and southwest (*SW*) array locations on 5 March 2006 and 30 March 2006.*

facing slope, the reverse is true for the early to mid-morning values. One limitation to this analysis relates to the aforementioned observations of thin cloud on 5 March. Aspect-dependent differences in incoming short wave radiation may be greater than indicated in Figure 4.7, as the method used to split incoming short wave radiation does not consider the opacity of the observed cloud cover.

Temperature measurements made at 10 cm depth on 30 March 2006 indicated that the magnitude of daytime warming was greater on the southeast-facing slope than on the southwest-facing slope. Incoming short wave radiations values projected onto each slope (Figure 4.7) support this observation. The timing of the cloud cover, in combination with the position of the sun relative to each slope, resulted in higher incoming short wave radiation inputs on the southeast-facing slope throughout the morning. The short wave radiation calculations show differences of more than 150 W/m^2. Although the incoming short wave radiation values became stronger on the southwest-facing slope in the afternoon, the differences were noticeably smaller.

4.5 Summary

Based on the field data collected for this study during the winters of 2005 and 2006, the following observations regarding variability in near-surface warming can be made:

- The magnitude of daytime temperature fluctuations typically decreased with depth below the snow surface.
- Even small changes in aspect resulted in substantial differences in near-surface warming.
- As cloud cover increased, aspect-dependent differences in daytime warming were observed to decrease.
- Because thin cloud enhanced incoming long wave radiation without substantially reducing incoming short wave radiation, the upper snowpack underwent substantial daytime warming under thin cloud conditions.
- While the magnitude of daytime warming typically increased with incoming short wave radiation as the winter season progressed, variability over terrain appeared to decrease.
- In addition to resultant differences in radiation input, aspect may have influenced near-surface warming through variation in snowpack properties

that affect the surface energy balance. These upper snowpack properties varied both over time and terrain.

- Variable cloud cover, in combination with the changing solar position over the day, was observed to alter the distribution of daytime warming over terrain.

CHAPTER FIVE: SNOWPACK MODEL COMPARISON

The primary objective of this chapter is to compare field measurements of near-surface temperature with output data from the SNOWPACK model. To date, little verification of SNOWPACK has been undertaken with specific attention to near-surface temperatures. None has been completed with data collected in the Columbia Mountains of British Columbia.

While inaccurate modelling of snowpack properties like density and grain type will impact the modelled surface energy balance, this assessment of the SNOWPACK model is limited specifically to near-surface temperatures. For each model run, a brief visual check of the initial model profile was undertaken to confirm that it was a reasonable representation of the observed profile. No further comparison of modelled snowpack properties (e.g. grain type, density, etc.) other than near-surface temperatures was completed.

Dr. Charles Fierz of the SLF visited the University of Calgary in March 2006 to install SNOWPACK and provide training. Additional information regarding use of the SNOWPACK model was obtained from Spreitzhofer et al. (2004) and Spreitzhofer et al. (2006).

This chapter begins with a section summarizing SNOWPACK data input requirements and outlining how these were derived from the field data. A short discussion of model settings used during this comparison follows in Section 5.2. Sections 5.3 and 5.4 present results of the near-surface temperature comparison between field measurements and SNOWPACK output data for the knoll top and knoll slope arrays, respectively. A brief summary is included in Section 5.5

5.1 Input data

To run the SNOWPACK model, the user must input meteorological data and an initial snow profile. Table 5.1 summarizes the meteorological data provided, on an hourly interval, for each SNOWPACK model run. The five in-snow temperatures included in the meteorological input file were not used in the model calculations, but were provided for comparison with the model output data.

Table 5.1: *Meteorological input data required for SNOWPACK modelling.*

Parameter	Units	Measurement location
air temperature	ºC	Mount Fidelity study plot (ACS)
relative humidity	percent	Mount Fidelity study plot (ACS)
wind speed	m/s	Mount Fidelity study plot (ASARC)
wind direction	degrees	Mount Fidelity study plot (ASARC)
incoming short wave radiation	W/m^2	Mount Fidelity study plot (ASARC)
incoming long wave radiation	W/m^2	Mount Fidelity study plot (ASARC)
ground surface temperature	ºC	assumed 0 ºC
precipitation	kg/m^2	Mount Fidelity study plot (ACS)
in-snow temperature (× 5)	ºC	Gopher Butte knoll

It is worth emphasizing that the meteorological data input to SNOWPACK were measured in the Mount Fidelity study plot, not on Gopher Butte knoll. Because the two locations are not far apart, values measured in the study plot were expected to be reasonable estimations; however, some discrepancies between measured near-surface temperatures and SNOWPACK output data may result from inaccurate representation of meteorological conditions on Gopher Butte by the input data.

General information required for each initial snow profile includes the date and time of observation, height of snow and location (latitude, longitude, elevation, slope angle and aspect). Because the manual snow profiles completed at each array site were shallow (approximately 40 cm in depth), a simplified representation of the lower snowpack layers was developed from full snow profile observations made nearby for other research projects.

To create an initial model profile, the user must provide information about each layer identified in the manual snow profile. The following points summarize the parameters required to create the model profile and how they were extracted from the field observations:

- *Layer thickness:* Slope normal measurement calculated from manual field measurements of layer thickness (vertical) and slope angle.
- *Temperature at top of layer:* The temperature at the top of each snow layer identified within the upper portion of the snowpack was interpolated linearly from thermocouple measurements corresponding to the manual snow profile observation time. Below 40 cm, temperatures at the top of each snow layer were interpolated linearly from a manual temperature measurement at 40 cm depth and an assumed temperature of 0 ºC at the base of the snowpack. Where a key temperature measurement did not correspond with a layer boundary, a 'dummy' layer boundary was created.
- *Volumetric fraction of water:* Estimated from field observations of liquid water content, as per the classification system outlined in the Canadian Avalanche Association Observation Guidelines and Recording Standards (CAA, 2002, p. 18). Snow layers identified as dry, moist and wet were estimated to have volumetric water contents of 0%, 1% and 5%, respectively.
- *Volumetric fraction of ice:* Calculated from the measured snow density and estimated volumetric fraction of water using the known densities of water

(1000 kg/m^3) and ice (917 kg/m^3). Where manual density measurements were not available for thin snow layers, values were estimated using grain type and hand hardness observations (Geldsetzer and Jamieson, 2001a).

- *Volumetric fraction of air:* Calculated from the volumetric fractions of water and ice (sum of volumetric fractions of water, ice and air must equal 1).
- *Date of layer formation:* Estimated from known burial dates of distinctive snowpack layers and daily snow depth measurements from the Mount Fidelity study plot.
- *Grain radius:* Determined from the average of maximum and minimum grain sizes observed in the field.
- *Bond radius:* For wet grains, assumed to be half of the grain radius. For all other grain types, assumed to be one-quarter of the grain radius (C. Fierz, personal communication, March 2006).
- *Sphericity, dendricity and grain marker:* Estimated from the observed grain type using SNOWPACK-specific guidelines provided for these parameters (Figure 5.1).

5.2 Model settings

SNOWPACK has some flexibility with respect to input data requirements and model boundary conditions. This section will provide a brief summary of relevant settings used during SNOWPACK modelling for this project.

- *Calculation time step:* Hourly thermocouple temperature measurements were extracted from data collected at 10 or 15 minute intervals. The remainder of

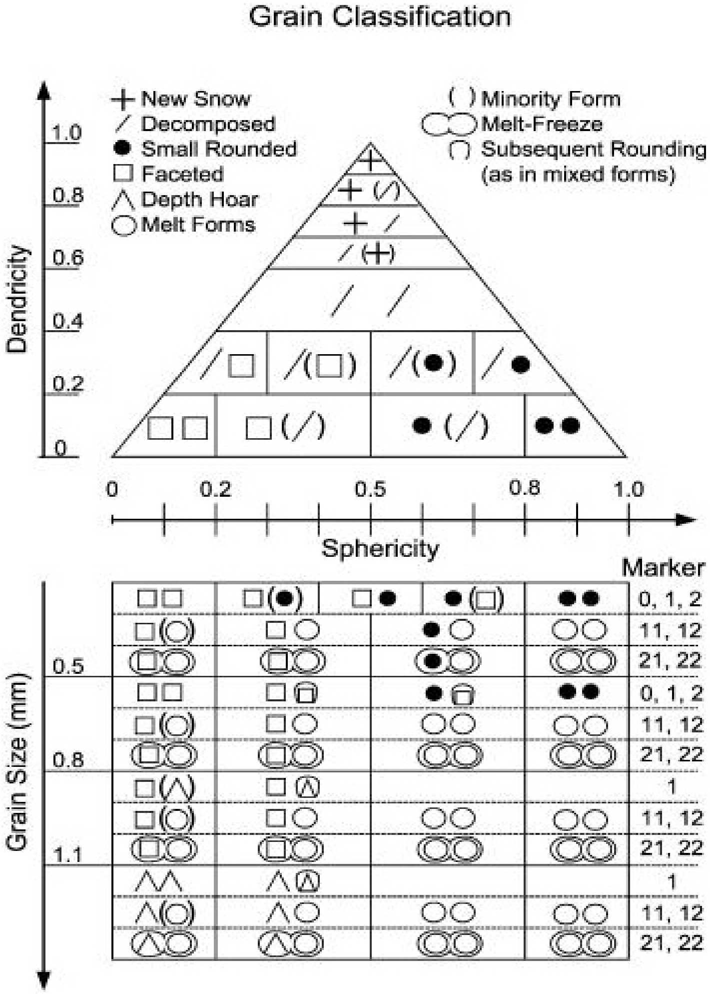

Figure 5.1: *Illustration of parameters (sphericity, dendricity and grain marker) used by SNOWPACK to define snow grain type (Spreitzhofer et al., 2006).*

the meteorological data were available hourly. A calculation time step of fifteen minutes was used, with hourly input data, for all model runs.

- *Short wave radiation:* SNOWPACK can use measurements of either, or both, incoming and reflected short wave radiation. Only incoming short wave radiation data were available for this study, requiring SNOWPACK to estimate a value for snow surface albedo. Lehning et al. (2002a) describe the empirically-derived equation included in SNOWPACK for albedo estimation.

- *Upper boundary condition:* Because consistent snow surface temperature measurements were not available throughout all of the field experiments, snow surface temperature values were not included in the meteorological input file. Without this information, SNOWPACK calculated snow surface temperatures from surface energy fluxes (Neumann boundary condition).
- *Lower boundary condition:* The bottom boundary condition was defined by a specified ground temperature (assumed 0 ºC).
- *Atmospheric stability:* SNOWPACK can be set to determine stratification of the atmospheric boundary layer either by assuming neutral stratification (i.e. logarithmic profile) or using Monin-Obukhov similarity theory. The Monin-Obukhov iteration is typically recommended when the Neumann boundary condition is applied at the snow surface (Spreitzhofer et al., 2006; C. Fierz, personal communication, March 2006). For four of the field experiments, modelling was completed using both options; SNOWPACK output data compared better with the field measurements when neutral stratification was specified. All model results presented in this document were obtained using the neutral stratification setting.
- *Canopy analysis:* Although SNOWPACK has the capability of considering the effects of tree cover on surface energy balance inputs, this functionality was not used in any of the model runs.

With the exception of the limited evaluation of the atmospheric stability setting noted above, no calibration of SNOWPACK model settings or parameters was completed prior to modelling.

5.3 Knoll top arrays

For an initial evaluation of near-surface temperature modelling, SNOWPACK output data was compared with knoll top temperature measurements made during nine of the eleven field experiments (Table 5.2). The experiment starting on 10 March 2005 was excluded because less than 24 hours of temperature measurements were collected. As incoming short and long wave radiation measurements were not available for the 25-26 April 2005 experiment, it was also excluded. For this comparison, SNOWPACK was set to output modelled temperatures at 5, 10, 15, 20 and 25 cm below the snow surface. Measured temperatures at corresponding depths were interpolated linearly from the field data. Aside from application of a calibration offset for each thermocouple (Section 3.2.2), no adjustment of the measured temperatures was made.

Table 5.2: *Summary of SNOWPACK modelling completed for knoll top arrays.*

Model start		**Duration of model run**
Date	***Time* (PST)**	**(hours)**
27 February 2005	1500	32
13 March 2005	1215	45
6 February 2006	1330	72
18 February 2006	1430	47
4 March 2006	1400	25
27 March 2006	1030	46
29 March 2006	1145	48
3 April 2006	1200	49
21 April 2006	1200	51

Discussion of the SNOWPACK model comparison begins with a qualitative assessment and moves on to a quantitative evaluation.

5.3.1 Qualitative comparison of model results with field measurements

Figure 5.2 illustrates SNOWPACK's graphical output display for snow temperature. Measured and modelled temperatures, at 10 and 15 cm depth, for the 6-12 February 2006 field experiment are plotted over time. SNOWPACK output data and measured temperatures agree quite well near the beginning of this period, with the model indicating slightly cooler temperatures at both depths. For the last few days of this run, which correspond with field observations of decreased cloud cover, there are greater differences between the modelled and measured values; SNOWPACK output data tends

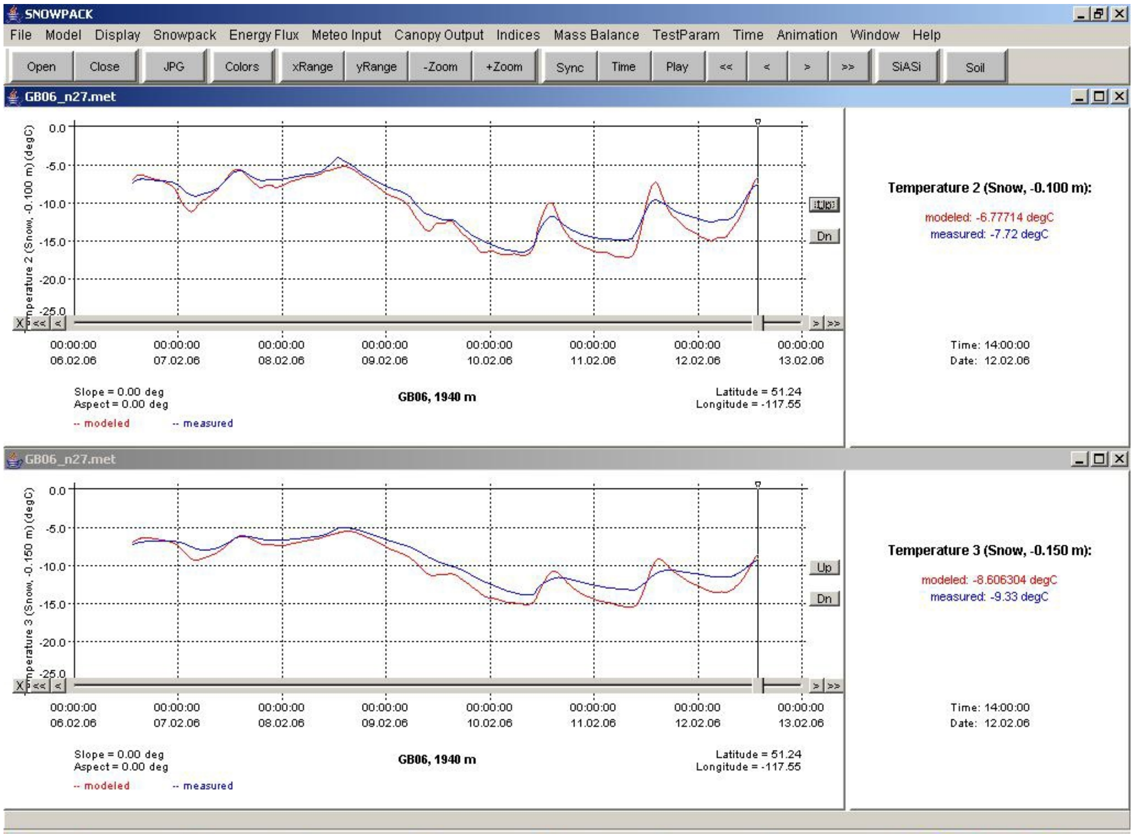

Slope = 0.00 deg
Aspect = 0.00 deg
Latitude = 51.24
Longitude = -117.55

Temperature 2 (Snow, -0.100 m):
modeled: -6.77714 degC
measured: -7.72 degC
Time: 14:00:00
Date: 12.02.06

Slope = 0.00 deg
Aspect = 0.00 deg
Latitude = 51.24
Longitude = -117.55

Temperature 3 (Snow, -0.150 m):
modeled: -8.606304 degC
measured: -9.33 degC
Time: 14:00:00
Date: 12.02.06

Figure 5.2: *SNOWPACK model output for measured and modelled temperatures (6-12 February 2006). Temperatures are shown at 10 cm (top) and 15 cm (bottom) depth. The temperatures, time and date displayed on the right-hand side of each graph correspond to the solid vertical 'slider' bar on the graph.*

to be warmer during the day and cooler overnight. These trends are apparent at both depths, as is a decrease in the magnitude of both measured and modelled daytime warming with depth. The length of this particular model run may also have contributed to decreased agreement between measured and modelled temperatures in the latter half of the simulation; because there are no other field experiments of comparable duration, the effect of model run length cannot be evaluated.

All of the SNOWPACK output data show a similar decrease in daytime warming with depth (consistent with the field measurements) and there is generally better agreement between measured and modelled temperatures deeper in the snowpack. Throughout four of the model runs, the modelled values are primarily cooler than the measured temperatures, while the reverse is the case for three runs. Results of the remaining two model runs do not show SNOWPACK output data to be consistently warmer or cooler than the measured temperatures. Notably, the model output data includes above-zero temperatures at 5 cm depth for short intervals during the experiments starting on 27 February 2005, 13 March 2005, 4 March 2006, 29 March 2006 and 21 April 2006.

The relationship between measured temperatures and SNOWPACK output data is not the same for all of the model runs. Although some show better agreement than others, no obvious trends in agreement are noted with variation in time of year or observed weather conditions. Based simply on a visual comparison of the plotted temperatures, SNOWPACK output data appears to compare best with field measurements made starting on 13 March 2005 and 3 April 2006 (assuming all measured temperatures above 0 ºC indicate snowpack temperatures of 0 ºC). Model output data for these two runs are included in Figures 5.3 and 5.4. Greater discrepancies between measured temperatures and SNOWPACK output data are noted for the field experiments starting on 18 February 2006 and 21 April 2006 (Figures 5.5 and 5.6).

As an indication of how much the SNOWPACK output data differs from the measured temperatures, Table 5.3 gives the maximum difference between measured and modelled temperatures at each depth, over all 9 model runs. These results also illustrate better agreement between measured and modelled values with increasing depth below the snow surface.

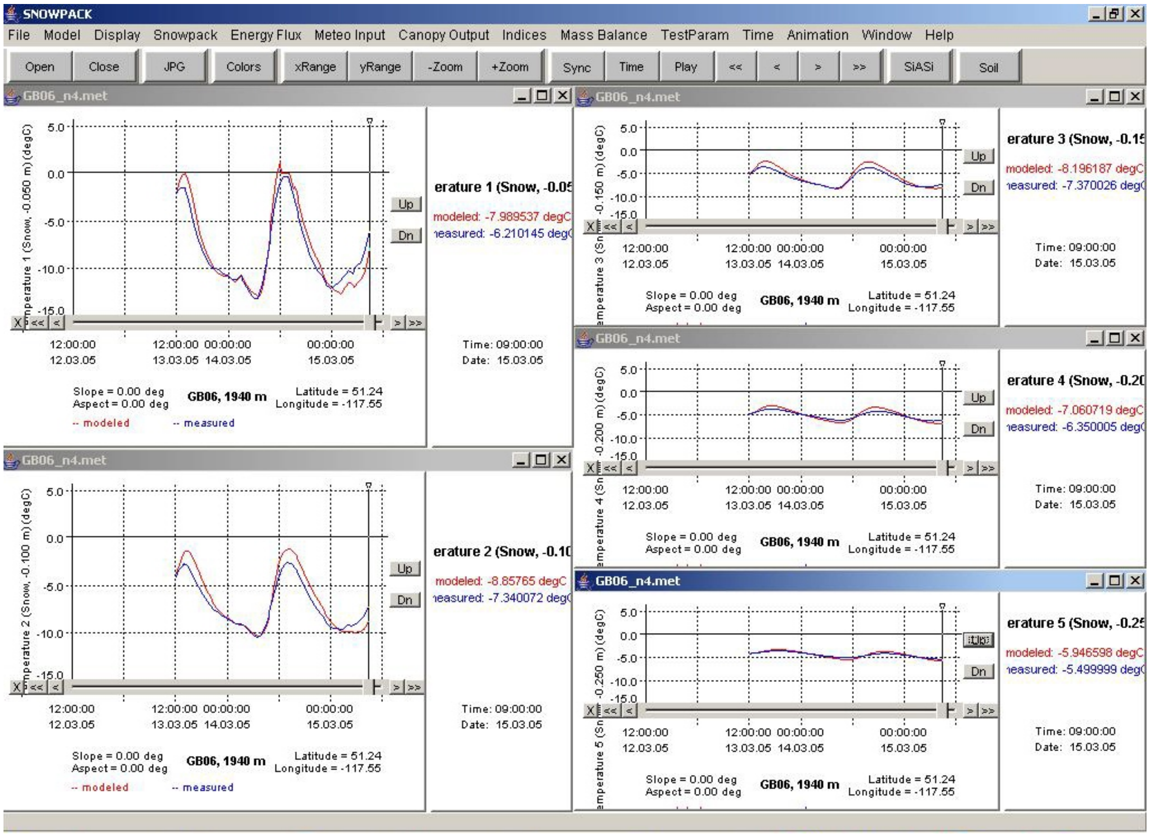

Figure 5.3: *SNOWPACK model output for measured and modelled temperatures that show good visual agreement (13-15 March 2005).*

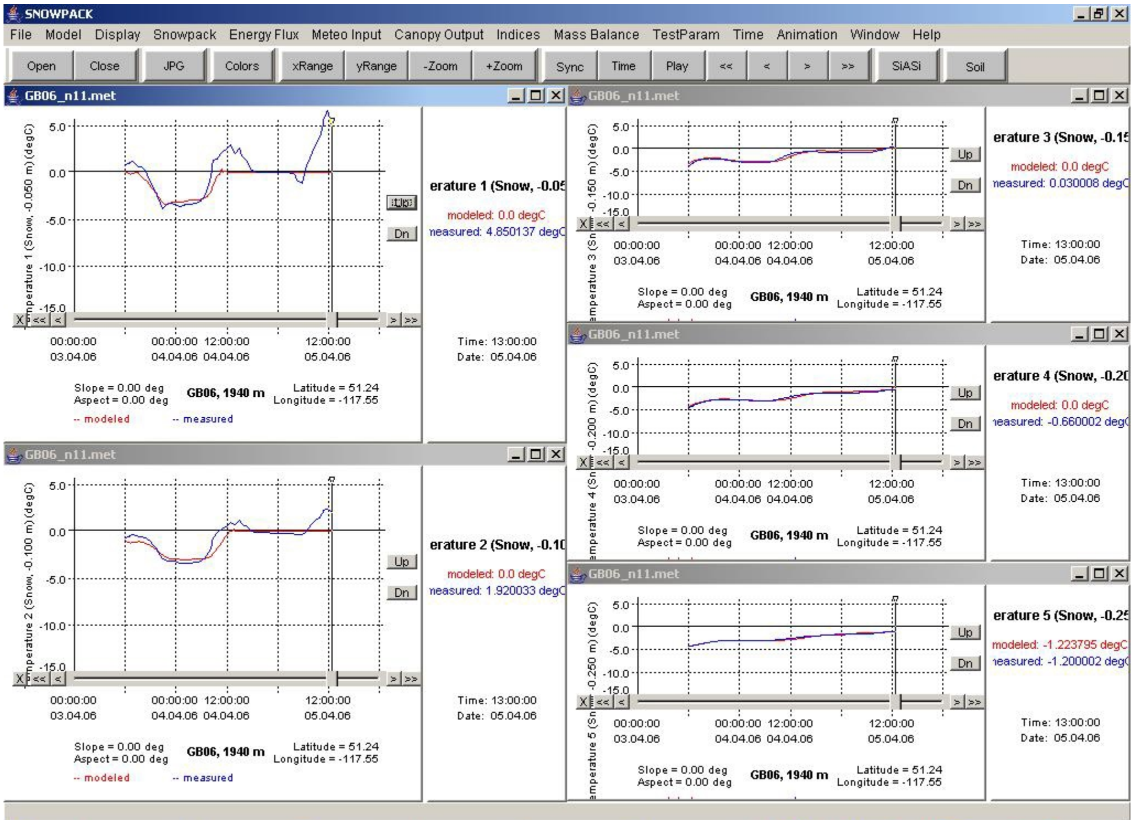

erature 1 (Snow, -0.05

modeled: 0.0 degC

neasured: 4.850137 degC

erature 2 (Snow, -0.10

modeled: 0.0 degC

neasured: 1.920033 degC

erature 3 (Snow, -0.15

modeled: 0.0 degC

neasured: 0.030008 degC

erature 4 (Snow, -0.20

modeled: 0.0 degC

neasured: -0.660002 degC

erature 5 (Snow, -0.25

modeled: -1.223795 degC

neasured: -1.200002 degC

Figure 5.4: *SNOWPACK model output for measured and modelled temperatures that show good visual agreement (3-5 April 2006). All measured temperatures above 0 ºC are assumed to be 0 ºC.*

Table 5.3: *Summary of maximum differences between SNOWPACK model results and measured temperatures. The maximum difference between the measured (T_{meas}) and modelled (T_{mod}) values, over all 9 model runs, is given at each comparison depth. The 'model direction' column indicates whether this difference relates to a modelled temperature that is warmer or cooler than the measured temperature.*

Depth (cm)	**Maximum $\lvert T_{\text{meas}} - T_{\text{mod}} \rvert$ (ºC)**	**Model direction**	**Model start**	
			Date	***Time***
5	6.8	warmer	29 March 2006	20:45
10	5.0	warmer	23 April 2006	6:00
15	4.2	warmer	5 March 2006	14:15
20	2.9	warmer	5 March 2006	15:00 *
25	2.3	cooler	10 February 2006	11:30

* *This difference corresponds to the last pair of measured/modelled temperatures in this model run.*

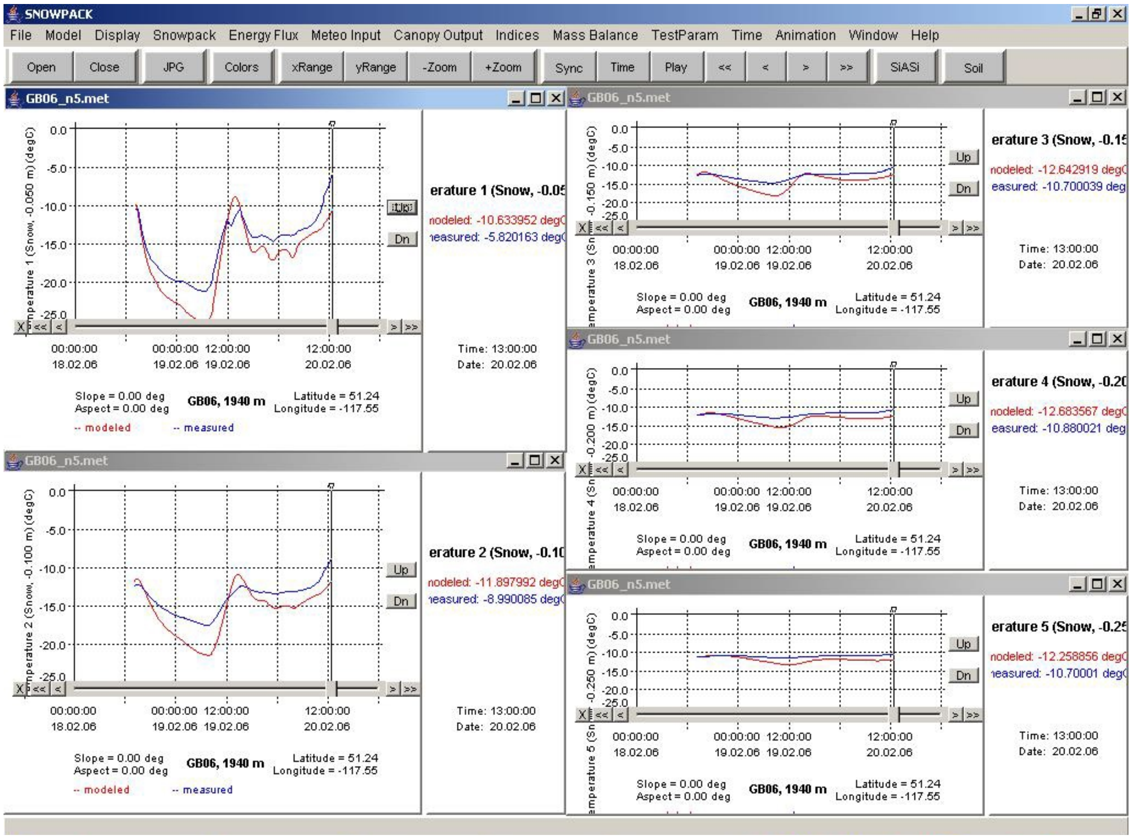

Figure 5.5: *SNOWPACK model output for measured and modelled temperatures that show greater discrepancies (18-20 February 2006).*

It is interesting to note that, at the four depths closest to the snow surface, the greatest difference between measured temperatures and SNOWPACK output data is associated with model results that are warmer than the measured temperatures. Prior to modelling, there was concern that differences between measured and modelled values would be biased by measurement errors (see Appendix A). Because the magnitude of the measurement errors was expected to increase near the snow surface and at times of peak incoming short wave radiation, it was anticipated that, particularly at 5 and 10 cm depth, the greatest differences would occur near midday and result in measured values warmer than the SNOWPACK model output. The fact that the data in Table 5.3 do not follow

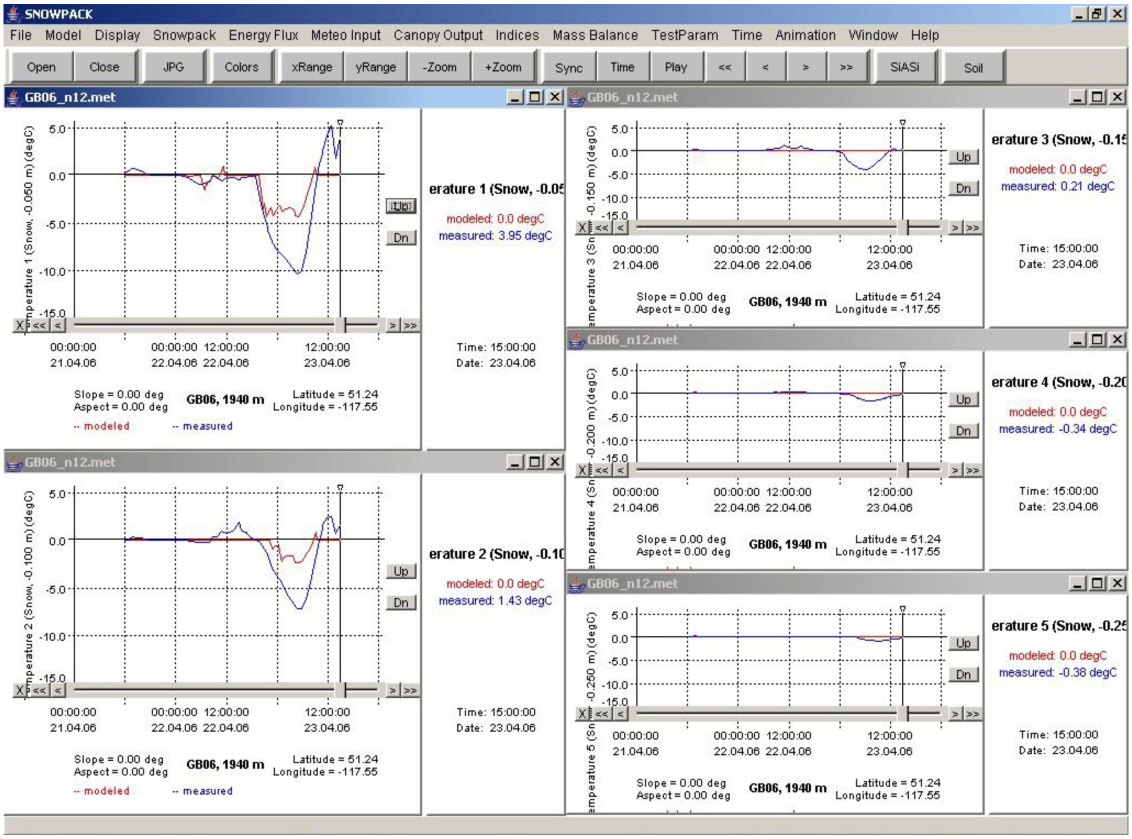

Figure 5.6: *SNOWPACK model output for measured and modelled temperatures that show greater discrepancies (21-23 April 2006).*

this pattern is encouraging as an indication of the absence of substantial measurement errors. Visual comparison of the temperature data also shows that, in most cases, the magnitude of modelled daytime warming is greater than measured (see the latter portion of Figure 5.2 for an example).

The field experiment spanning 6-12 February 2006, because of its length, was one for which a second snow profile was completed at each array location. Surface hoar was observed on the surface in the manual snow profile completed on 10 February 2006, and is shown in the SNOWPACK output (Figure 5.7). Because surface hoar formation

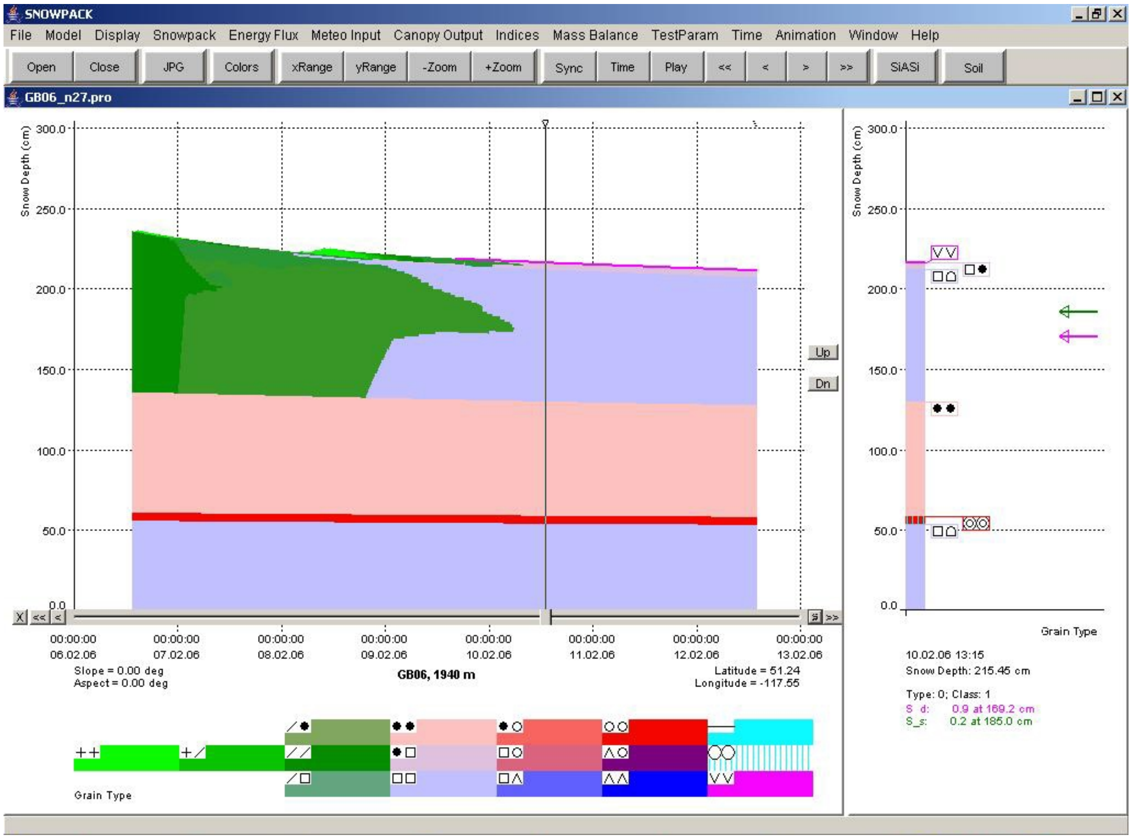

Figure 5.7: *SNOWPACK modelled grain type for 6-12 February 2006. As noted in the colour legend at the bottom of the image, surface hoar (VV) is represented by magenta shading. The profile displayed on the right-hand side of the graph corresponds to manual profile observations made at 1315 on 10 February 2006. Surface hoar was observed at this time in the field, consistent with the model output.*

requires a strong temperature gradient in the air above a cold snow surface (McClung and Schaerer, 1993, p. 44), it is quite sensitive to the surface energy balance and its presence in the model output suggests realistic modelling of surface energy fluxes. Modelled grain metamorphism in the near-surface snow layers does not compare as well with the manual profile, indicating a combination of facets, rounds and mixed forms on 10 February. Field observations showed decomposing fragments to a depth of at least 40 cm on this date. This discrepancy could result from the lack of sensitivity in manual field observations of grain type, unrealistic modelling of near-surface temperature gradients or difficulties in modelling grain metamorphism.

5.3.2 Quantitative comparison of model results with field measurements

As noted in Section 2.2.3, Lundy et al. (2001) used several statistical descriptors to compare SNOWPACK model output data to field observations. To provide a quantitative assessment of the SNOWPACK results, four of the same descriptors were applied (Table 5.4).

Table 5.4: *Statistical descriptors used to assess SNOWPACK model performance (after Lundy et al., 2001).*

Statistical parameter	**Symbol**	**Calculation**	**Interpretation**
Mean bias	MB	$\sum_{i=1}^{n} \frac{(T_{\mathrm{mod}(i)} - T_{meas(i)})}{n}$	indicates direction of error
Root mean square error	RMSE	$\sqrt{\frac{\sum_{i=1}^{n} (T_{\mathrm{mod}(i)} - T_{meas(i)})^2}{n}}$	value indicates expected magnitude of error
Pearson correlation coefficient	*r*	$\frac{\sum_{i=1}^{n} \left[\left(T_{\mathrm{mod}(i)} - \mu_{\mathrm{mod}} \right) \cdot \left(T_{meas(i)} - \mu_{meas} \right) \right]}{\sqrt{\sum_{i=1}^{n} \left(T_{\mathrm{mod}(i)} - \mu_{\mathrm{mod}} \right)^2 \cdot \sum_{i=1}^{n} \left(T_{meas(i)} - \mu_{meas} \right)^2}}$	value (0 to 1) indicates strength of linear correlation, sign indicates direction
Willmott and Wicks index of agreement	WW	$1 - \frac{\sum_{i=1}^{n} (T_{meas(i)} - T_{\mathrm{mod}(i)})^2}{\sum_{i=1}^{n} (\lvert T_{\mathrm{mod}(i)} - \mu_{meas} \rvert + \lvert T_{meas(i)} - \mu_{meas} \rvert)^2}$	value (0 to 1) indicates strength of agreement

SNOWPACK output data were paired with measured values interpolated by SNOWPACK at a 15 minute interval from the hourly input measurements. The mean bias (MB), root mean square error (RMSE), Pearson correlation coefficient (*r*) and Willmott and Wicks index of agreement (WW) were calculated for each of the nine model runs at all five comparison depths (Table 5.5). All measured temperatures greater than 0 ºC were set equal to 0 ºC prior to these calculations, but no adjustments were made to the modelled values.

Table 5.5: *Results of quantitative comparison between SNOWPACK output data and measured temperatures. Mean bias (*MB*), root mean square error (*RMSE*), Pearson Correlation Coefficient (r) and Willmott and Wicks Index of Agreement (*WW*) were calculated for each of the nine model runs at all five comparison depths.*

	Depth	**2005**		**2006**						
	(cm)	***27 Feb***	***13 Mar***	***6 Feb***	***18 Feb***	***4 Mar***	***27 Mar***	***29 Mar***	***3 Apr***	***21 Apr***
	n	129	180	579	187	101	187	190	197	205
MB	5	1.50	0.26	-0.49	-2.09	-1.69	-1.53	-0.83	0.00	1.24
	10	1.02	0.50	-0.78	-1.69	-0.70	-0.93	-0.55	-0.07	0.90
	15	0.73	0.46	-0.87	-1.50	-0.29	-0.66	-0.33	0.13	0.63
	20	0.35	0.11	-0.95	-1.25	-0.20	-0.48	-0.10	0.06	0.32
	25	0.16	0.01	-1.01	-0.98	-0.04	-0.34	0.00	-0.01	0.19
RMSE	5	1.71	1.14	1.23	2.59	2.44	1.85	2.15	0.44	2.35
	10	1.25	0.98	1.23	2.23	2.01	1.16	1.24	0.50	1.81
	15	1.02	0.71	1.22	1.83	1.98	0.97	0.95	0.29	1.36
	20	0.53	0.46	1.18	1.46	1.27	0.75	0.59	0.20	0.60
	25	0.31	0.24	1.22	1.15	0.71	0.49	0.39	0.12	0.33
r	5	0.98	0.98	0.97	0.96	0.98	0.95	0.89	0.95	0.94
	10	0.96	0.98	0.97	0.93	0.98	0.98	0.95	0.92	0.95
	15	0.93	0.99	0.97	0.89	0.96	0.97	0.95	0.97	0.34
	20	0.95	0.99	0.98	0.76	0.94	0.94	0.96	0.98	--- *
	25	0.95	0.98	0.98	0.54	0.96	0.91	0.90	0.99	--- *
WW	5	0.95	0.98	0.98	0.91	0.95	0.93	0.92	0.97	0.78
	10	0.93	0.97	0.97	0.82	0.93	0.94	0.94	0.96	0.65
	15	0.84	0.96	0.96	0.68	0.79	0.89	0.91	0.98	0.38
	20	0.88	0.95	0.94	0.53	0.75	0.82	0.90	0.99	0.41
	25	0.86	0.96	0.92	0.35	0.77	0.80	0.86	0.99	0.42

* *Because SNOWPACK modelled temperatures remain at 0 ºC for the entire model period, a Pearson correlation coefficient could not be calculated.*

The mean bias calculations, which indicate the expected direction of modelling errors, show similar results to observations noted in the previous section. Three of the

SNOWPACK runs result in temperatures warmer than the measured values at all five depths (27 February 2005, 13 March 2005 and 21 April 2006); five runs show modelled temperatures typically cooler than the measured values (6 February 2006, 18 February 2006, 4 March 2006, 27 March 2006 and 29 March 2006). The experiment starting on 3 April 2006 is the only one for which these results do not show a consistent trend of warmer or cooler SNOWPACK output data at all five depths.

The average, maximum and minimum root mean square error calculated at each depth are included in Table 5.6. These results, as well as the root mean square error calculations summarized in Table 5.5, indicate that modelling errors typically decrease with depth. The exception to this trend is the model run for 6-12 February 2006, which showed a root mean square error of approximately 1.2 ºC at all five depths.

The model period starting on 3 April 2006 results in the minimum root mean square error at all depths, suggesting the best fit between SNOWPACK output data and measured values. High root mean square errors were calculated at all depths for the 18-20 February 2006 model period. These results are consistent with the visual comparison of SNOWPACK output data with measured temperatures values. Note that the root mean square error results do not take into account the direction of the model error.

Table 5.6: *Summary of root mean square error results over all 9 model runs.*

Depth (cm)	**Minimum RMSE (ºC)**	**Average RMSE (ºC)**	**Maximum RMSE (ºC)**
5	0.44	1.8	2.59
10	0.50	1.4	2.23
15	0.29	1.2	1.98
20	0.20	0.8	1.46
25	0.12	0.6	1.22

Both the Pearson correlation coefficient and Willmott and Wicks index of agreement are statistical measures which indicate the strength of agreement between two sets of data. The two parameters do not entirely agree with each other; however, model runs identified as a good fit to the measured values through visual comparison or the root mean square error calculations typically show high values for both parameters. Similarly, lower values are common when SNOWPACK output data appeared to differ more from the measured temperatures.

5.3.3 Daytime warming comparison

From a research perspective, one benefit of SNOWPACK modelling is the possibility of supplementing field measurements with modelled data. It was hoped that, during development of the warming model presented in Chapter 6, daytime warming values could be generated for time periods and aspects without field measurements. For this approach to be valid, SNOWPACK modelled temperature values must show satisfactory agreement with the existing field measurements. As noted in Section 5.3.1, visual inspection of plotted data indicates that the magnitude of SNOWPACK modelled daytime warming is typically greater than measured.

A dataset consisting of measured and SNOWPACK modelled daytime warming (ΔT_d) values for the knoll top arrays was assembled to assess the suitability of SNOWPACK model output data for use in development of a simple warming model. This dataset included ΔT_d values at depths of 5, 10, 15, 20 and 25 cm depth below the snow surface. Any pairs in which either the SNOWPACK modelled value or measured temperature reached 0 ºC were excluded from the dataset. One additional pair, in which the SNOWPACK modelled ΔT_d value was 0 °C, was also excluded; this left 41 pairs for comparison. While a significant coefficient of determination ($r^2 = 0.85$, $p < 0.001$) was found in the dataset, linear regression results indicate that SNOWPACK tends to overestimate the magnitude of ΔT_d relative to the field measurements (Figure 5.8). A significant intercept was not identified in the linear regression analysis. ΔT_d values calculated using the regression equation are approximately 24% higher than measured values.

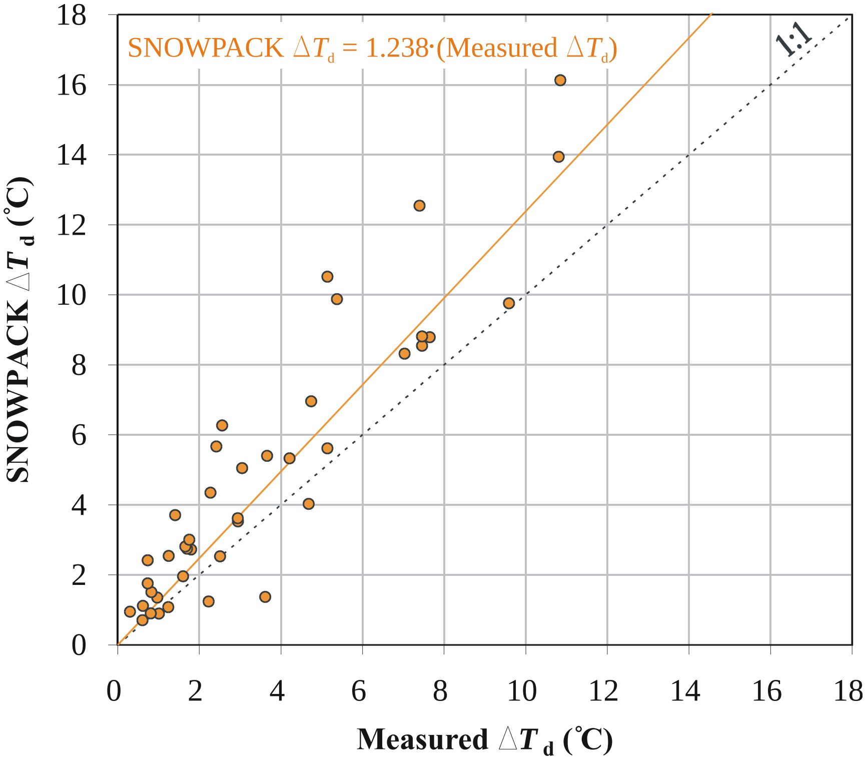

Figure 5.8: *Comparison of measured and SNOWPACK modelled daytime warming (ΔT_d). A significant coefficient of determination ($r^2 = 0.85$, $p < 0.001$) was found in the dataset ($n = 41$). The solid line illustrates the linear regression equation (displayed in upper left corner) that best fits the data points.*

For interest, Figure 5.9 was prepared to illustrate variations in the magnitude of different surface energy balance components. For each of the days included in the ΔT_d comparison, hourly values of net short wave radiation, net long wave radiation, sensible turbulent and latent turbulent fluxes were extracted from the SNOWPACK output file. These hourly values were summed from sunrise to the time at which the maximum temperature at 10 cm depth was measured. While radiation fluxes typically have the greatest magnitude, the SNOWPACK output data indicate that sensible and latent convective fluxes were not insignificant.

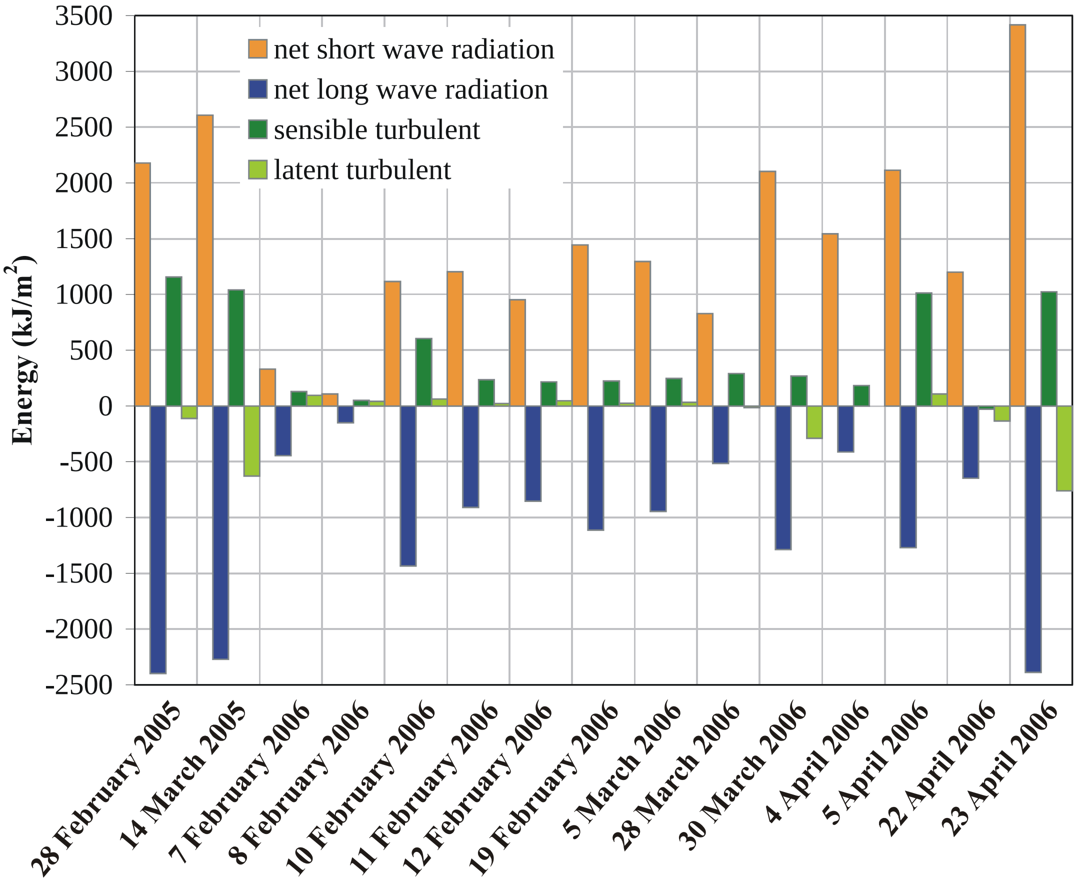

Figure 5.9: *SNOWPACK modelled surface energy for days included in the daytime warming* (ΔT_d) *comparison. Columns indicate total energy from sunrise to the time at which the maximum temperature was measured at 10 cm depth for: net short wave radiation, net long wave radiation, sensible turbulent and latent turbulent fluxes.*

Because of limited data for verification and the noted discrepancy between measured and SNOWPACK modelled ΔT_d, SNOWPACK generated data was not included in the development of the spatial warming model.

5.4 Knoll slope arrays

As a means of evaluating the effect of tree cover on field temperature measurements, a limited comparison of SNOWPACK modelled temperatures with values measured on the knoll slopes was undertaken. The objective was to determine whether greater differences between SNOWPACK output data and measurements made in areas with more tree cover (specifically, the southwest and west-facing knoll slopes) could identify where and when field measurements were strongly influenced by the tree cover. Note that, although SNOWPACK can be set to adjust surface energy fluxes based on user-supplied tree canopy information, this functionality was not used in any of the model runs.

Of the nine modelled experiments, five included measurements made on the southwest or west-facing slopes with more tree cover. Two of these were excluded from subsequent SNOWPACK modelling because manual profiles on the knoll slopes were observed midway through the field experiment; the time remaining in each experiment was considered too short for a model run. For the three experiment periods left, each knoll slope array was modelled as a separate run using the manual snow profile observations completed at each array location to create the initial profile. Table 5.7 summarizes the knoll slope model runs, including the mean bias and root mean square error statistics calculated for each. As noted in the previous section, all above-freezing field measurements were set to 0 ºC prior to calculation of the statistical parameters.

Table 5.7: *Comparison of knoll slope SNOWPACK output data with measured values. Mean bias (*MB*) and root mean square error (*RMSE*) were calculated for each array location at all five comparison depths.*

Model start date	Array	*n*	Aspect	Statistical parameter	Depth (cm)				
					5	*10*	*15*	*20*	*25*
18 February 2006	1	187	TOP	MB	-2.09	-1.69	-1.50	-1.25	-0.98
				RMSE	2.59	2.23	1.83	1.46	1.15
	2	190	SW (212)	MB	-4.85	-3.82	-2.89	-2.04	-1.98
				RMSE	5.12	4.12	3.24	2.46	2.31
	3	196	E (108)	MB	1.78	1.82	1.68	1.36	-0.08
				RMSE	3.88	3.43	2.71	1.96	3.88
	4	193	NE (41)	MB	-2.31	-2.00	-1.51	-1.33	-1.34
				RMSE	2.49	2.24	1.73	1.55	1.54
3 April 2006	1	197	TOP	MB	0.00	-0.07	0.13	0.06	-0.01
				RMSE	0.44	0.50	0.29	0.20	0.12
	2	197	SW (204)	MB	1.42	0.14	0.21	0.01	-0.15
				RMSE	2.50	0.55	0.64	0.56	0.59
	3	197	E (91)	MB	-0.30	-0.29	-0.29	-0.47	-0.57
				RMSE	0.80	0.87	0.98	1.04	1.07
	4	197	NE (35)	MB	0.01	0.08	0.26	0.21	0.08
				RMSE	0.24	0.22	0.39	0.31	0.18
21 April 2006	1	205	TOP	MB	1.24	0.90	0.63	0.32	0.19
				RMSE	2.35	1.81	1.36	0.60	0.33
	2	205	E (96)	MB	-0.06	-0.06	0.07	0.00	0.00
				RMSE	0.53	0.24	0.22	0.00	0.00
	3	201	TOP	MB	0.68	0.75	0.59	0.30	0.10
				RMSE	1.67	1.51	1.24	0.57	0.19
	4	201	W (264)	MB	0.76	0.31	0.09	0.00	0.00
				RMSE	1.76	0.70	0.28	0.00	0.00

5.4.1 18-20 February 2006

For the SNOWPACK model runs starting on 18 February 2006, mean bias calculations indicate that SNOWPACK typically underestimates temperatures relative to the measured values on the knoll top, southwest and northeast-facing slopes. On the east-facing slope the model results are generally higher than the measured values. The magnitude of the difference between measured and modelled values appears to be greatest on the southwest-facing slope at most depths. Results for both the southwest and east-facing slopes indicate modelling errors greater than the maximums identified during analysis of the knoll top model results. For this field experiment, an array with nearby trees (southwest) shows measured temperatures consistently higher than predicted by the SNOWPACK. For an array in a relatively open area (east), measured temperatures are consistently lower than predicted by SNOWPACK.

5.4.2 3-5 April 2006

With the exception of a relatively high root mean square error at 5 cm depth for the southwest array, neither the mean bias nor root mean square error values calculated for the period beginning on 3 April 2006 suggest distinctive modelling errors associated with measurements made on the southwest-facing slope (more tree cover).

Figure 5.10 illustrates the measured temperatures and SNOWPACK output data at 10 cm depth for this experiment period. Good agreement can be seen for the knoll top and northeast-facing slope, while results for both the east and southwest-facing slopes show periods where the measured temperature values diverged from the SNOWPACK output data. At the southwest array location, shading by nearby trees is a likely explanation for lower measured temperature on the afternoon of 3 April (temperatures were lower by approximately 3 ºC).

Discrepancies on the east-facing slope are more difficult to account for. The greatest differences, associated with measured temperatures warmer than SNOWPACK modelled values, occurred mid-afternoon on 3 April and from approximately 0100 to

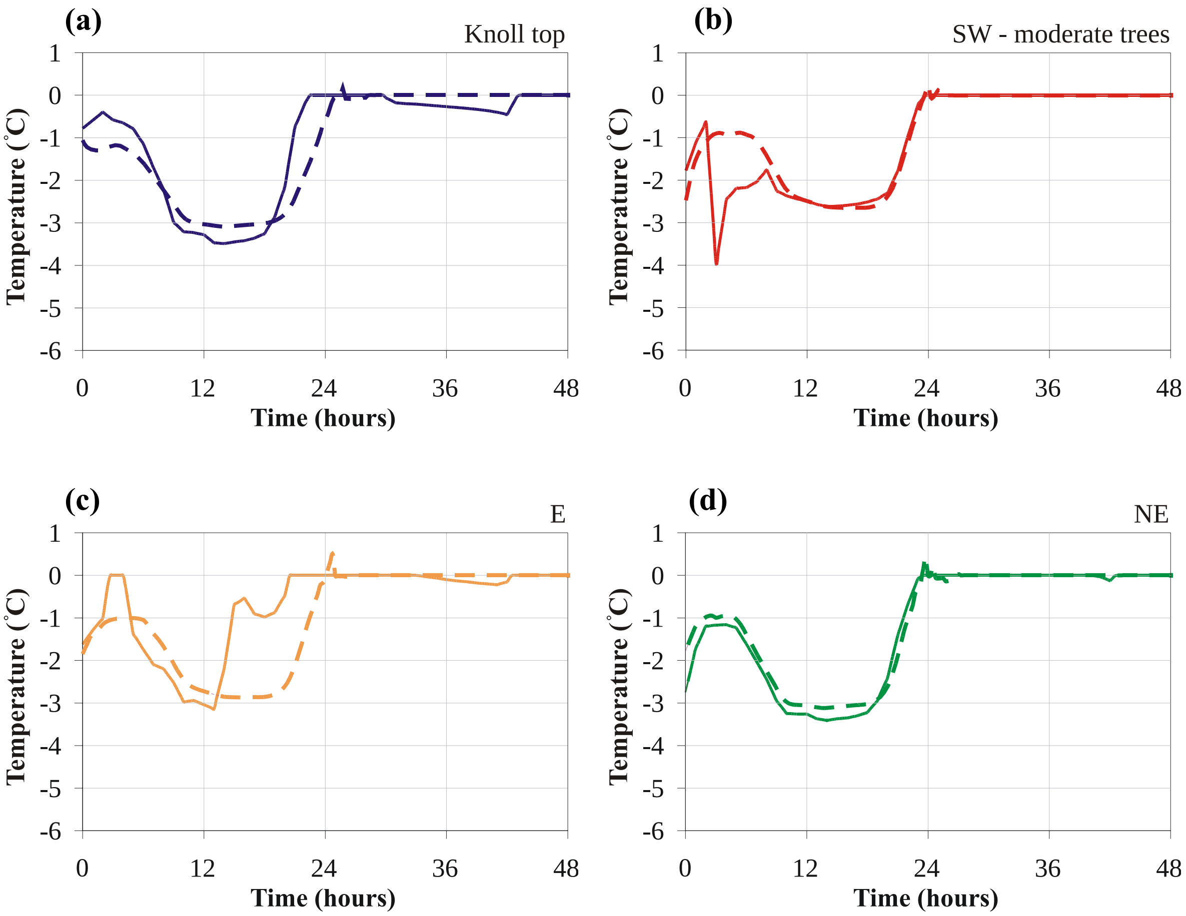

Figure 5.10: *Plots of measured (solid line) and SNOWPACK modelled (dashed line) temperature values, at 10 cm depth, for the measurement period starting on 3 April 2006: (a) knoll top, (b) southwest, (c) east and (d) northeast. Zero on the time axes corresponds with 12:00 noon on 3 April 2006. All measured values greater than 0 ºC have been set to 0 ºC.*

0800 the following night. The mid-afternoon increase in measured temperature is possibly the result of melting in the upper snowpack layers at that time. Meteorological data from the Fidelity study plot indicated a relatively constant temperature (approximately -2 ºC) and a slight increase in wind speed (0.1 to 1.6 m/s) overnight on 4 April. A speculative explanation is that the relatively open, east-facing array site experienced stronger winds and slightly warmer air temperatures than measured in the study plot and that the observed warming resulted from convective heat transfer.

5.4.3 21-23 April

For the final field experiment, 21-23 April 2006, the four arrays were set up as follows: two on the knoll top, one on the relatively open, east-facing knoll slope and one on the west-facing knoll slope with more tree cover. The two knoll top array sites were selected to have tree cover similar to each of the knoll slope arrays. The statistical parameters included in Table 5.7 are somewhat skewed for this experiment because both the measured and modelled temperatures were at 0 ºC for a good portion of the measurement period, but they show that SNOWPACK output data tends to be warmer than the measured temperatures at all four array locations. Comparison of the root mean square error values indicates that the knoll top measurements made under more tree cover typically agree better with the SNOWPACK output data than those made at the relatively open knoll top site. Conversely, the knoll slope measurements corresponding to more tree cover (west) show greater differences from the SNOWPACK output data than those made on the open (east) knoll slope. Tree cover appears to affect agreement between measured temperatures and SNOWPACK output data more on the knoll slopes that on the knoll top.

Figure 5.11 shows the measured and modelled temperatures, at 10 cm depth, for the 21 April 2006 experiment. At all locations other than the east-facing slope, measured temperatures are noticeably cooler than the SNOWPACK modelled values on the morning of 23 April 2006. Better agreement between measured and modelled values for

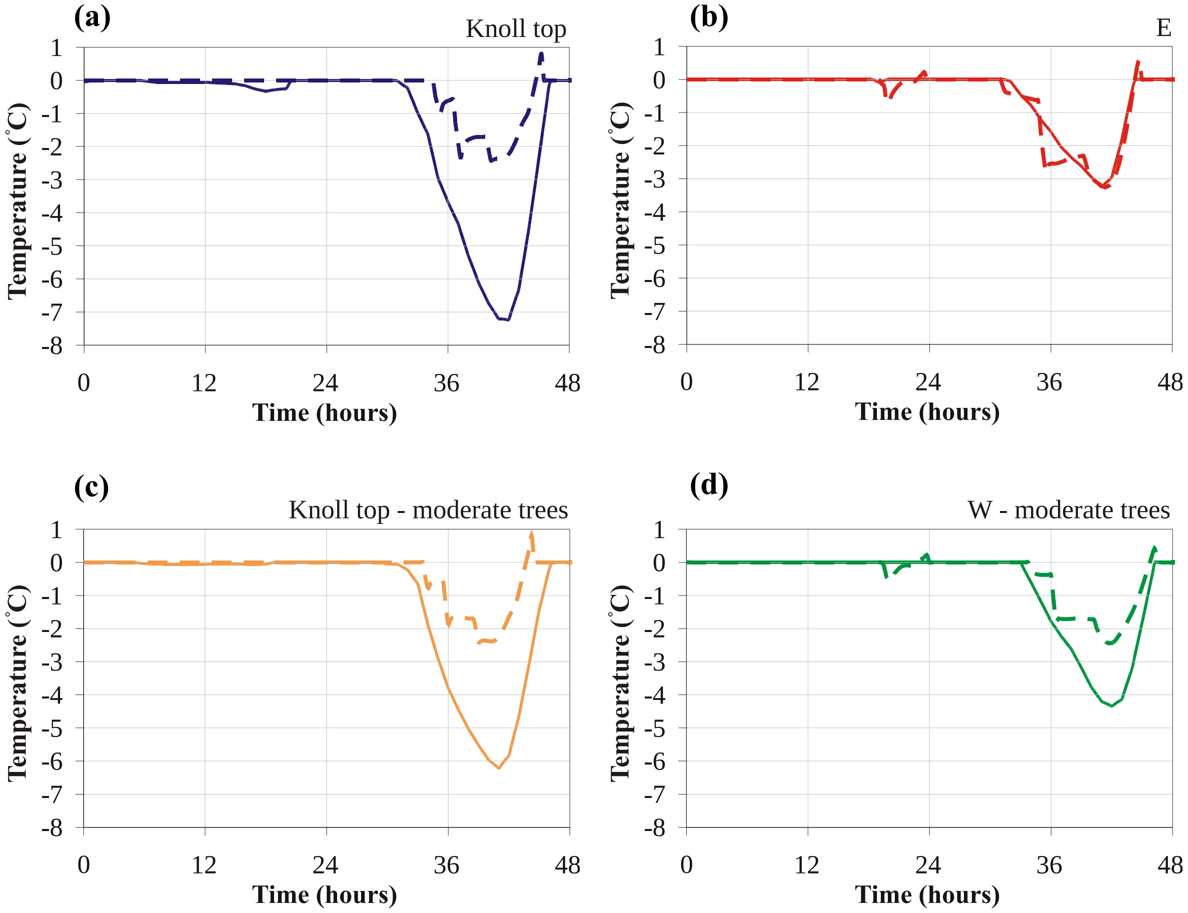

Figure 5.11: *Plots of measured (solid line) and SNOWPACK modelled (dashed line) temperature values, at 10 cm depth, for the measurement period starting on 21 April 2006: (a) knoll top, (b) east, (c) knoll top with greater tree cover and (d) west with greater tree cover. Zero on the time axes corresponds with 12:00 noon on 21 April 2006. All measured values greater than 0 ºC have been set to 0 ºC.*

the knoll top site with more tree cover than for the more open knoll top site result from a slight difference (approximately 1 ºC) in minimum measured temperature.

Measured temperature minimums on the morning of 23 April 2006 show greater variation between array sites than the SNOWPACK output data. The early-morning timing suggests that the differences between measured values and model results relate more to long wave radiation fluxes than short-wave radiation fluxes.

5.5 Summary

Overall, comparison of SNOWPACK modelled near-surface temperatures with field measurements indicates fairly good agreement. The average difference between measured and modelled values, approximately 1.5 ºC at 10 cm, typically decreases with depth. SNOWPACK does not consistently over or underestimate near-surface temperatures, and differences between measured and modelled values do not show obvious relationships with time of year, aspect or weather conditions. Measurement errors related to absorption of excess short wave radiation by the field equipment do not appear to contribute to differences between field measurements and SNOWPACK model output data.

Daytime warming values calculated from SNOWPACK model output data are typically larger than those measured during the field experiments. For this reason, and because verification of SNOWPACK modelled near-surface temperatures is limited, additional data were not generated for inclusion in the dataset for development of the simple warming model. Results of limited SNOWPACK modelling on the knoll slopes are not conclusive enough to draw conclusions regarding the effect of tree cover on the field measurements.

CHAPTER SIX: WARMING MODEL

6.1 Objective

The intent of the proposed warming model is to provide spatial information about daytime warming for forecasters to include in their snow stability evaluation. The model does not include the effects of daytime warming on stability; this is left to the forecasters' experience and knowledge. In order for the model to be useful, it must be easy to apply and interpret. As such, keeping the data input requirements simple and providing visual model output are desirable. Development of a model that will provide useful accuracy, while still maintaining simple input data requirements, is a challenge given the complexity of the surface energy balance and the spatially variable nature of the mountain snowpack.

Figure 6.1 illustrates a conceptual plan for the proposed semi-empirical warming model. The dependent variable, daytime warming (ΔT_d) is described in Section 6.2. Potential predictor variables are discussed in Section 6.3, while Section 6.4 summarizes how these were selected through a series of correlation analyses with ΔT_d. Section 6.5 outlines creation of the warming model using multivariate linear regression. Limited verification of the semi-empirical warming model is presented in 6.6. Some model limitations and an example of graphical output display are provided in Sections 6.7 and 6.8.

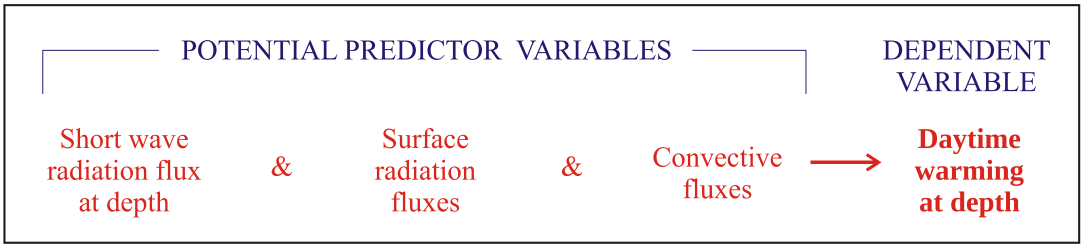

Figure 6.1: *Conceptual plan of semi-empirical warming model.*

6.2 Dependent variable

The parameter chosen to represent temperature fluctuations in the upper portion of the snowpack is the magnitude of daytime warming at a given depth (ΔT_d). This is the difference, at depth *d*, between the temperature at sunrise and the maximum afternoon temperature (Figure 4.1). Daytime warming values are given in ºC throughout this work.

All days for which field measurements did not span the sunrise to afternoon peak time period were excluded from the dataset. Data collected during the period starting on 25 April 2005 were also excluded because no radiation measurements were recorded and because of isothermal conditions in the upper snowpack. In addition, data collected on 9 February 2006 were excluded because a substantial decrease in air temperature and variable cloud cover resulted in a daytime decrease in snow temperature on this particular day. The remaining data are summarized in Table 6.1. The time of sunrise for each day was calculated using methods outlined by the U.S. National Oceanic and Atmospheric Administration Surface Radiation Research Branch (n.d.).

For each day included in the analysis, temperatures at 5, 10, 15, 20 and 25 cm depth were linearly interpolated from the thermocouple measurements. The only correction applied to the field temperature measurements prior to interpolation was the calibration offset measured for each thermocouple (Section 3.2.2). At each of the interpolated depths, the temperature at sunrise and the afternoon peak temperature were then extracted and used to calculate ΔT_d. In some cases, field measurements did not capture the afternoon maximum at all depths; data at depths for which this was the case were excluded from the analysis.

Table 6.1: *Summary of field data included in the warming model analysis.*

Measurement date	**Calculated time of sunrise (PST)**	**Average sky condition**	**Aspects**	**# of useable data**
28 February 2005	0640	FEW	TOP, S (162), NE 63), NE (32)	19
14 March 2005	0610	FEW	TOP, S (180), N (7), E (100)	19
7 February 2006	0720	BKN	TOP, S (164), N (5) *	15
8 February 2006	0718	OVC	TOP, S (164), E (86), N (5)	19
10 February 2006	0715	FEW	TOP, S (164), E (86), N (5)	17
11 February 2006	0713	CLR	TOP, S (164), E (86), N (5)	17
12 February 2006	0711	SCT	TOP, S (164), E (86), N (5)	11
19 February 2006	0658	BKN	TOP, SW (212), E(108), NE(41)	15
5 March 2006	0629	BKN	TOP, SW (216), SE (116), NE (43)	7
28 March 2006	0538	OVC	TOP, S (168), E (80), NW (336)	18
30 March 2006	0533	BKN	TOP, SW (213), SE (114), NE (48)	16
4 April 2006	0522	BKN	TOP, SW (204), E (91), NE (35)	6
5 April 2006	0520	SCT	TOP, SW (204), E (91), NE (35)	8
22 April 2006	0443	BKN	TOP, E (96), TOP, W (264) **	4
23 April 2006	0441	CLR	TOP, E (96), TOP, W (264) **	5
			TOTAL	**196**

* *No measurements for fourth array due to loose multiplexer connection.*

** *One knoll top array in a relatively open area and one knoll top array in a more treed area for comparison.*

Because energy input to the snowpack after it reaches 0 ºC contributes to melting rather than temperature change, the magnitude of daytime warming measured in these cases is not comparable to daytime warming measurements made in a sub-zero snowpack. Any data for which the measured maximum afternoon temperature reached 0 ºC were also excluded. The final dataset consisted of 196 measurements of ΔT_d at depths varying in 5 cm increments from 5 to 25 cm.

One assumption of multivariate linear regression is the independence of prediction errors. If autocorrelation of errors is significant, the rate of Type I errors (i.e. incorrect rejection of a null hypothesis) increases (Tabachnick and Fidell, 2001, 121-122). Because this dataset includes ΔT_d measurements collected at the same depth on adjacent days and on the same day at adjacent depths, autocorrelation of errors may be present. The effect is expected to be small because the dataset includes measurements made at different locations over nine different field experiment periods.

6.3 Predictor variables

Surface energy flux variables included in the early stages of warming model development are listed in Table 6.2, with brief descriptions provided in the following sections. Units of W/m^2 were used for all energy flux values included in the analysis. Potential predictor variables including either incoming short or long wave radiation values were determined using both measured and estimated values. Calculation methods used for all estimated values are summarized in Appendix B. Although heat can also be added to the snowpack through liquid precipitation, the conditions under which this occurs are quite specific. This process did not occur during the field experiments and was not incorporated into the warming model.

6.3.1 Incoming short wave radiation

Three different variables representing incoming short wave radiation were tested during model development. The first was simply the daily maximum short wave radiation value (SW_{max}). The other two included sums of hourly incoming short wave radiation fluxes; from sunrise to the time of peak incoming short wave radiation (SW_{Σ_SWmax}), and from sunrise to the time at which the maximum temperature was measured at the associated depth ($SW_{\Sigma\_T max}$). All three variables were calculated from data measured in the Mount Fidelity study plot and from estimated values. For ΔT_d measurements made on the knoll side slopes, measured and estimated short wave radiation values were projected accordingly (Section B.1.1).

Table 6.2: *Summary of surface energy flux variables included for consideration as predictor variables in the warming model.*

Surface energy flux	**Variables considered**	**Determined from**	**Section reference**
incoming short wave radiation *	SW_{max} SW_{Σ_SWmax} SW_{Σ_Tmax}	measured and estimated hourly values	6.3.1
incoming long wave radiation	iLW_{avg_SWmax} [a] iLW_{Σ_SWmax} [a] iLW_{avg_Tmax} [a] iLW_{Σ_Tmax} [a] iLW_{avg} [b]	[a] measured and estimated hourly values [b] average estimated values	6.3.2
outgoing long wave radiation	oLW_{avg} oLW_{Σ_SWmax} oLW_{Σ_Tmax}	estimated average surface temperature (two calculation methods assessed)	6.3.3
combined surface radiation term *	$[0.5 \cdot SW_{max} \cdot (1-\alpha) + iLW_{avg\_SWmax} - oLW_{avg}]$ $[SW_{\Sigma\ SWmax} \cdot (1-\alpha) + iLW_{\Sigma\ SWmax} - oLW_{\Sigma\_SWmax}]$ $[SW_{\Sigma\ Tmax} \cdot (1-\alpha) + iLW_{\Sigma\ Tmax} - oLW_{\Sigma\_Tmax}]$	measured hourly short and incoming long wave values, estimated outgoing long wave values (two calculation methods assessed)	6.3.4
convective heat flux	u_{avg} $(T_a - T_s)_{avg}$ $u_{avg} \cdot (T_a - T_s)_{avg}$	measured u, T_a values, estimated T_s values (two calculation methods assessed)	6.3.5

* *Selection of albedo (α) estimation method is discussed in Section 6.4.1.*

6.3.2 Incoming long wave radiation

Several variables representing incoming long wave radiation were tested during model development. An average incoming long wave radiation value (iLW_{avg_SWmax}) and a sum of incoming long wave radiation (iLW_{Σ_SWmax}) were calculated from both measured and estimated (Section B.1.2) hourly values for the sunrise to peak incoming short wave radiation time period. Similarly, an average value ($\mathrm{iLW}_{\mathrm{avg}\_T\mathrm{max}}$) and a sum ($\mathrm{iLW}_{\Sigma\_T\mathrm{max}}$) were calculated for the time period spanning sunrise to the time at which the maximum snow temperature at the associated depth was measured. In addition, an average incoming long wave radiation value was estimated from the daily average of cloud cover observations and the averages of air temperature and relative humidity measurements made in the Fidelity study plot at 0700 and 1200 ($\mathrm{iLW}_{\mathrm{avg}}$).

6.3.3 Outgoing long wave radiation

Similar variables representing outgoing long wave radiation were also developed. Because neither measurements of outgoing radiation nor consistent surface temperature measurements were available, calculated outgoing long wave radiation values could not be verified prior to inclusion in the model development process. Two methods of estimating snow surface temperature, described in detail in Section B.1.3, were used to calculate a daily average outgoing long wave radiation value ($\mathrm{oLW}_{\mathrm{avg}}$). Sums were determined by multiplying this value by either the number of hours from sunrise to the peak short wave radiation value ($\mathrm{oLW}_{\Sigma\_\mathrm{SWmax}}$) or the number of hours from sunrise to the time at which the maximum temperature at depth was measured ($\mathrm{oLW}_{\Sigma\_T\mathrm{max}}$). Outgoing long wave radiation variables based on both surface temperature estimation methods were assessed as potential predictors of ΔT_{d}.

6.3.4 Combined surface radiation

The individual radiation terms contributing to the surface energy balance were also combined into a single surface radiation term. Three possible combinations, representing average values ($[0.5 \cdot SW_{max} \cdot (1-\alpha)+iLW_{avg\_SWmax}-oLW_{avg}]$) and two sums ($[SW_{\Sigma\_SWmax} \cdot (1-\alpha)+iLW_{\Sigma\_SWmax}-oLW_{\Sigma\_SWmax}]$ and $[SW_{\Sigma\_Tmax} \cdot (1-\alpha)+iLW_{\Sigma\_Tmax}-oLW_{\Sigma\_Tmax}]$) were included. Two sets of the combined surface radiation variables were assessed, based on measured short and long wave radiation values with outgoing long wave radiation estimates calculated using each surface temperature estimation method.

6.3.5 Convective heat flux

Equations used to calculate sensible convective heat fluxes show that heat transfer is proportional to wind speed and to the difference in temperature between the air and the snow surface (Section 1.5.2). These parameters were considered both individually and as a combined product (u_{avg}, $(T_a-T_s)_{avg}$ and $u_{avg} \cdot (T_a-T_s)_{avg}$). Wind speed values were based on a daily average of measurements from the Mount Fidelity study plot, while the average difference between air and snow surface temperature values was determined from measurements made in the study plot at 0700 and 1200. Two sets of variables were assessed, each using a different surface temperature estimation method (Section B.1.3). Because the magnitude of energy exchange resulting from latent convective heat fluxes is typically small (Plüss and Mazzoni, 1994), latent heat fluxes were not considered other than through inclusion of wind speed as a variable on its own in the analysis.

6.4 Correlation analyses

To determine which predictor variables to incorporate into the warming model, a series of correlation analyses with the dependent variable, ΔT_d, were carried out. All data included were measured on either an interval or ratio scale, indicating that Pearson correlations would be appropriate; however, questionable normality of some variables suggested the use of non-parametric methods. Spearman rank correlations, which are based on the assumption of monotonic, but not necessarily linear, relationship between two variables, are an appropriate alternative. In most cases, Pearson and Spearman rank correlations were calculated; both methods typically identified the same strongest potential predictor variable within each set, based on the relative strengths of correlations with ΔT_d. For this reason, and because sample sizes were large enough to reduce concerns regarding serious biases due to non-normality of residuals (Statsoft, 2006), only the Pearson correlation coefficients (r) are reported. Correlation coefficients with $p < 0.05$ were considered significant.

6.4.1 Albedo and extinction coefficient

The magnitude of short wave radiation at depth within the snowpack is often modelled using Equation 6.1 (e.g. Male and Granger, 1981).

$$\mathrm{SW_d} = \mathrm{SW_s}\cdot(1 - \alpha)\cdot\exp(-\beta\cdot d) \qquad (6.1)$$

where $\mathrm{SW_d}$ = short wave radiation at depth d (W/m^2)
$\mathrm{SW_s}$ = short wave radiation incident on the snow surface (W/m^2)
α = albedo
β = short wave radiation extinction coefficient (m^{-1})
d = depth below snow surface (m)

Appendix B outlines five methods for estimating albedo (Section B.2.1) and two methods for estimating the short wave radiation extinction coefficient (Section B.2.2). For each of the 196 ΔT_d measurements included in the dataset, ten values of short wave radiation flux at depth were calculated, using all possible combinations of the albedo and extinction coefficient estimates. The sum of hourly incoming short wave radiation measurements, calculated from sunrise to the time at which the maximum temperature was measured, was used as the value of short wave radiation incident on the snow surface. The highest significant Pearson correlation with ΔT_d ($r = 0.77$, $p < 0.001$) corresponded to the method obtained from Baker et al. (1990) for calculating albedo (Equation B.20) and the constants provided by Lehning et al. (2002a) for calculating extinction coefficient (Appendix B.2.2).

6.4.2 Short wave radiation at depth

In addition to Equation 6.1, the following simple approximation of short wave radiation at depth below the snow surface was included in the correlation analysis.

$$\mathrm{SW_d} = \mathrm{SW_s} \cdot (1 - \alpha) / d \qquad (6.2)$$

where $\mathrm{SW_d}$ = short wave radiation at depth d (W/m^2)
$\mathrm{SW_s}$ = short wave radiation incident on the snow surface (W/m^2)
α = albedo
d = depth below snow surface (m)

To estimate the magnitude of directly penetrating short wave radiation at depth below the snow surface, each of the three surface short wave radiation flux variables discussed in Section 6.3.1 was calculated using measured hourly values and combined with both of the depth approximations. Albedo was estimated as per Baker et al. (1990) and extinction coefficient as per Lehning et al. (2002a). Of the six combinations evaluated, the daily maximum short wave radiation value used with Equation 6.2, subsequently referred to as $SW_{max} \cdot (1-\alpha)/d$, provided the highest significant Pearson correlation with ΔT_d ($r = 0.84$, $p < 0.001$). An analysis undertaken with estimated hourly short wave radiation values showed a similar result ($r = 0.83$).

At this stage, data collected at 5 cm depth were excluded from the model because they were subject to greater temperature and depth measurement errors than data collected at or below 10 cm depth (Appendix A). As daytime temperature fluctuations decrease with depth below the snow surface, they are of lower magnitude and less likely to impact stability; consequently, data at depths 20 cm or greater were also excluded from the dataset at this stage. A comparison of Pearson correlations between ΔT_d and measured $SW_{max} \cdot (1-\alpha)/d$ at each depth interval showed much lower correlations at depths of 5, 20 and 25 cm ($r = 0.56$, $p < 0.001$; $r = 0.36$, $p < 0.015$; $r = 0.25$, $p < 0.16$; respectively) than at 10 and 15 cm ($r = 0.81$, $p < 0.001$; $r = 0.78$, $p < 0.001$; respectively). Approximately forty data points were included in the correlation analysis at each depth.

To check that reduction of the dataset did not affect results to this point in the analysis, evaluation of the three short wave radiation variables with each depth approximation was repeated using only data from 10 and 15 cm depths ($n = 80$). Analyses done with both measured and estimated short wave radiation parameters again showed the strongest significant correlations between $SW_{max} \cdot (1-\alpha)/d$ and ΔT_d ($r = 0.84$, $p < 0.001$ for measured values; $r = 0.79$, $p < 0.001$ for estimated values). A subsequent correlation analysis using measured maximum short wave radiation values with each of the previously noted albedo estimates to calculate $SW_{max}\cdot(1-\alpha)/d$ confirmed that, with the smaller dataset, the albedo estimation method of Baker et al. (1990) still provided the best correlation with ΔT_d.

As mentioned in Section 3.1, tree cover was not consistent across Gopher Butte knoll and there was some concern that denser tree cover may have influenced temperature measurements made on the northwest, west and southwest knoll slopes. Tree cover can influence the amount of short wave radiation incident on the snow surface through shading (Section 2.1.2); neither the measured nor estimated incoming short wave radiation values include tree shading effects. After splitting the dataset into three categories by amount of tree cover (Table 6.3), scatterplots of $SW_{max}\cdot(1-\alpha)/d$ against ΔT_d were visually examined. Using only data from 10 and 15 cm depth, the number of data points within the moderate tree cover category (n = 6) was too small to conduct a statistical comparison of the three groups. Figure 6.2 is the scatterplot based on measured maximum short wave radiation values; a similar plot was prepared based on estimated maximum short wave radiation values. As there is no visible difference between the tree cover categories in either scatterplot, and therefore no indication that the measured ΔT_d values were affected by changes in incoming short wave radiation as a result of tree cover, no additional data were excluded from the dataset.

Table 6.3: *Division of model building dataset for tree cover comparison.*

Category	**Tree cover**	**Aspects**	***n***
1	mostly open	NE, E, SE	26
2	light	N, TOP, S	48
3	moderate	NW, W, SW	6

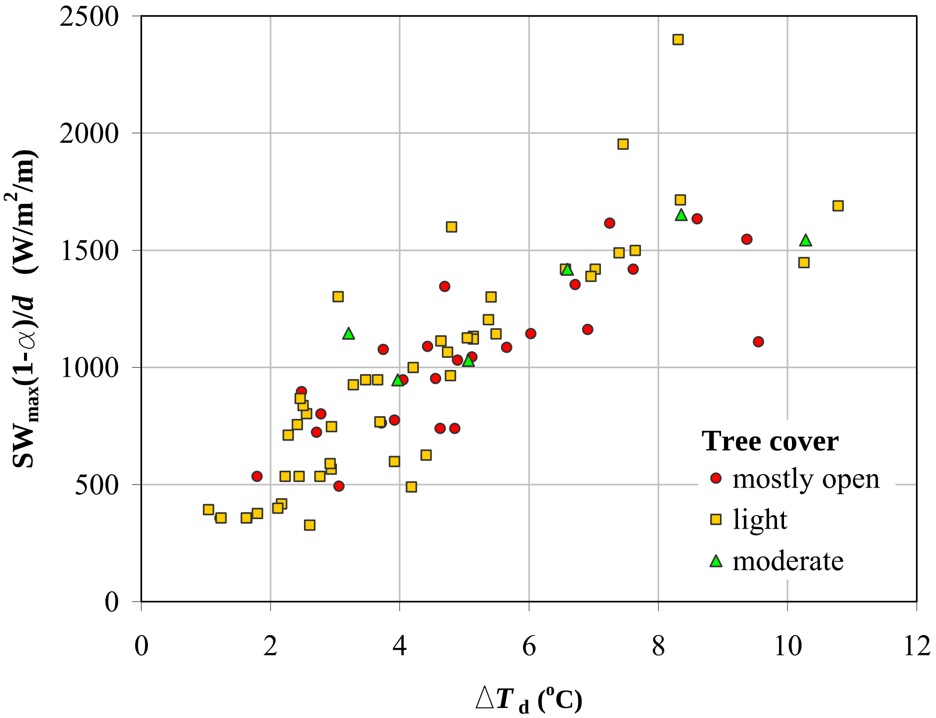

Figure 6.2: *Scatterplot of* SW_{max}·(1-α)/*d*, *calculated from measured short wave radiation values, against daytime warming* (ΔT_d) *measured at 10 and 15 cm depths (n = 80). Points have been divided into three categories (mostly open, light, moderate) based on the amount of tree cover at the array site.*

6.4.3 Individual surface fluxes

Using the 10 and 15 cm depth dataset (n = 80), correlation analyses with ΔT_d were completed for the individual surface energy flux variables presented in Table 6.2. Three variations were evaluated with each:

1. (variable)
2. (variable) / d
3. (variable)·(k / d)

where d = depth below snow surface (m)
k = effective conductivity of snow (W/m·ºC)

Conductive heat flux across a layer of snow can be calculated by multiplying the thermal conductivity of snow by the temperature gradient across that layer (Section 1.5.3). The third noted variation was evaluated as a means of incorporating a measure of conductive heat transfer from the snow surface to the depth of interest. The method developed by Sturm et al. (1997) was used to calculate the effective thermal conductivity corresponding to each data point (Section B.2.3). Results of the individual surface flux analyses are summarized in Table 6.4 and Figure 6.3.

Table 6.4: *Summary of Pearson correlation analyses between daytime warming (ΔT_d) measurements and potential surface energy flux variables. The datasets consisted of measurements made at 10 and 15 cm depth (n = 80).*

Surface energy flux		**Highest significant Pearson correlation with daytime warming (ΔT_d)**		
		Variable	***p***	***r***
incoming short wave radiation	measured	$SW_{max} \cdot (1-\alpha)/d$	< 0.001	0.84
	estimated	$SW_{max} \cdot (1-\alpha)/d$	< 0.001	0.79
incoming long wave radiation	measured	$iLW_{avg\_T max} \cdot (k/d)$	< 0.003	0.33
	estimated	$iLW_{avg\_T max} \cdot (k/d)$	< 0.001	0.43
outgoing long wave radiation		$oLW_{avg} \cdot (k/d)$ *	< 0.001	0.57
convective heat flux		u_{avg}	< 0.001	-0.46

* *Corresponds to calculation of surface temperature using the regression equation developed from field measurements (Equation B.17, Section B.1.3).*

For the short wave radiation variable comparison, results are the same as those reported in Section 6.4.2. For both measured and estimated short wave radiation values, the maximum daily short wave radiation value, combined with the simple depth approximation method, correlated best with ΔT_d. Given the simplicity of this variable, the magnitude of the Pearson correlation is encouraging for development of a simple

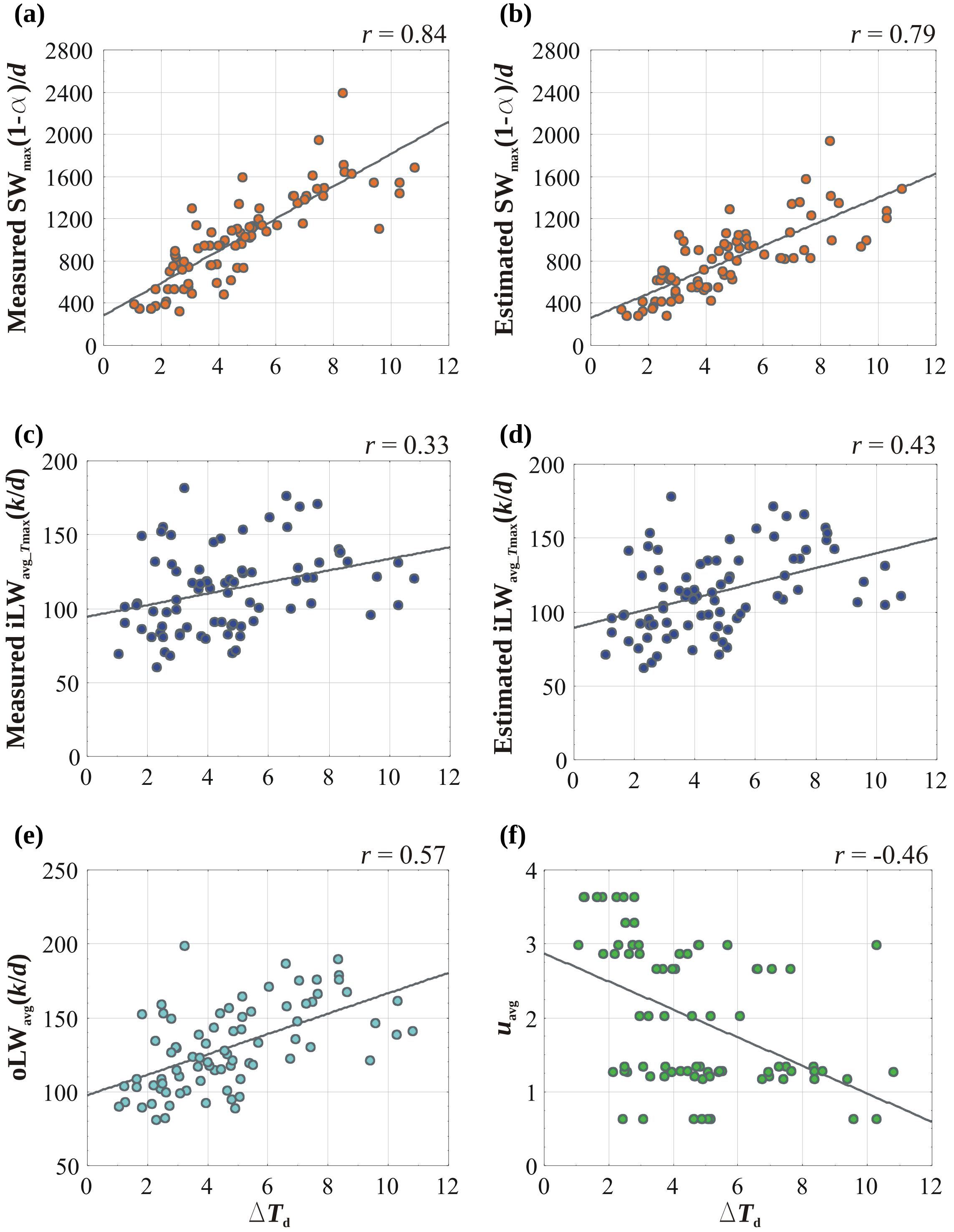

Figure 6.3: *Scatterplots of individual surface energy flux variables having the highest significant Pearson correlations with daytime warming* (ΔT_d). *(a) Measured* $SW_{max} \cdot (1-\alpha)/d$, *(b) Estimated* $SW_{max} \cdot (1-\alpha)/d$, *(c) Measured* $iLW_{avg\_T_{max}} \cdot (k/d)$, *(d) Estimated* $iLW_{avg\_T_{max}} \cdot (k/d)$, *(e)* $oLW_{avg} \cdot (k/d)$ *and (f)* u_{avg}. *The datasets consisted of measurements made at 10 and 15 cm depth (n = 80).*

warming model. Scatterplots of measured and estimated $\mathrm{SW}_{\mathrm{max}} \cdot (1-\alpha)/d$ against ΔT_{d} are shown in Figure 6.3(a) and Figure 6.3(b), respectively.

The measured incoming long wave radiation variable showing the strongest correlation with ΔT_{d} is an average value, calculated over the sunrise to maximum temperature at depth time period, combined with the conductivity approximation (Table 6.4, Figure 6.3(c)). A similar result is observed for variables calculated from hourly estimated incoming long wave radiation values (Table 6.4, Figure 6.3(d)). Somewhat surprisingly, the correlations are typically stronger for the estimated values than for the measured values. Calculating average incoming long wave radiation from average temperature and relative humidity measurements rather than hourly estimates ($\mathrm{iLW}_{\mathrm{avg}} \cdot (k/d)$) resulted in only a slight decrease in the Pearson correlation with ΔT_{d} ($r = 0.42$).

Tree cover can also affect incoming long wave radiation (Section 2.1.2); visual comparison of incoming long wave radiation against ΔT_{d}, again divided into categories by amount of tree cover, was also completed at this stage. No difference between the tree cover categories was apparent in scatterplots prepared using both measured and estimated hourly incoming long wave radiation values, again providing no indication that tree cover affected the measured ΔT_{d} values in the 10 and 15 cm depth dataset ($n = 80$).

Outgoing long wave radiation variables calculated from surface temperature estimated with the linear regression (Equation B.17) consistently had higher correlations with ΔT_{d} than those based on Equation B.18. Again, the average value combined with the conductivity term provided the strongest significant correlation (Table 6.4, Figure 6.3(e)). The positive sign of the correlation between $\mathrm{oLW}_{\mathrm{avg}} \cdot (k/d)$ and ΔT_{d}, however, does not initially seem to make physical sense. Because outgoing long wave radiation acts to cool the snow surface, one would expect increases in outgoing long wave radiation to correspond with decreases in daytime warming. Outgoing long wave radiation, however, is strongly dependant on the snow surface temperature. In this case, snow surface temperature was calculated from a regression equation that includes air temperature and cloudiness as input variables. These parameters also have a strong effect on incoming long wave radiation, for which a positive correlation with ΔT_d is both expected and observed. Analysis shows a strong significant Pearson correlation (r = 0.91, $p < 0.001$) between measured $\mathrm{iLW}_{\mathrm{avg}\_T\mathrm{max}}\cdot(k/d)$ and estimated $\mathrm{oLW}_{\mathrm{avg}}\cdot(k/d)$. Cross-correlation between incoming and outgoing long wave radiation parameters will be a concern if both are identified as significant predictors of ΔT_d in the regression analysis used to build the warming model.

The negative correlation between the strongest convective heat flux variable, u_avg, and ΔT_d also seems counterintuitive (Table 6.4). Increased wind speed, which suggests increased convective heat transfer, would contribute to cooling of the snow surface if the surface temperature was warmer than the air temperature. Depending on which surface temperature estimation method is used, average values indicate that this is the case for 20 to 50% of the data points included in the analysis. The magnitude of the Pearson correlation (r = -0.46, $p < 0.001$) does not suggest a strong relationship between these two variables (Figure 6.3(f)). Because wind was light during the field experiments (the maximum average daily wind speed measured was only 3.6 m/s) and because wind speed on its own, without consideration of depth below the snow surface, does not seem a logical predictor of ΔT_d, the correlation appears to lack a physical explanation.

After wind speed, the highest significant Pearson correlation ($r = 0.26$, $p < 0.021$) in the convective heat flux analysis was between ΔT_d and $(T_a\text{-}T_s)_{avg}\cdot(k/d)$. Contrary to the outgoing long wave radiation results, variables based on surface temperatures calculated with Equation B.18 performed the best. No significant correlations were found between ΔT_d and any convective flux variables based on surface temperatures calculated with the regression equation (B.17).

It is interesting to note that, for most of the individual surface flux terms, the strongest correlations with ΔT_d are for variables that included a measure of average snow conductivity from the snow surface to the depth of interest (Table 6.4). Given that these terms only contribute to the energy balance at the snow surface and ΔT_d is a measure of temperature change at depth, this is not a surprising result. The obvious exception is incoming short wave radiation, which likely has the strongest effect on ΔT_d through direct penetration to the depth of interest.

6.4.4 Combined surface radiation

The three variations assessed for each individual surface flux (i.e. (variable), (variable)/d, (variable)$\cdot$(k/d)) were also applied with the combined surface radiation variables listed in Table 6.2. The combined surface radiation terms that showed the strongest significant correlations with ΔT_d, for both measured and estimated incoming radiation values, are based on radiation sums calculated from sunrise to the time at which the maximum snow temperature was measured (Table 6.5). Scatterplots against ΔT_d are included in Figure 6.4. In contrast to the note at the end of the previous section, the inclusion of conductivity with the combined surface radiation variables did not strengthen the correlations with ΔT_d.

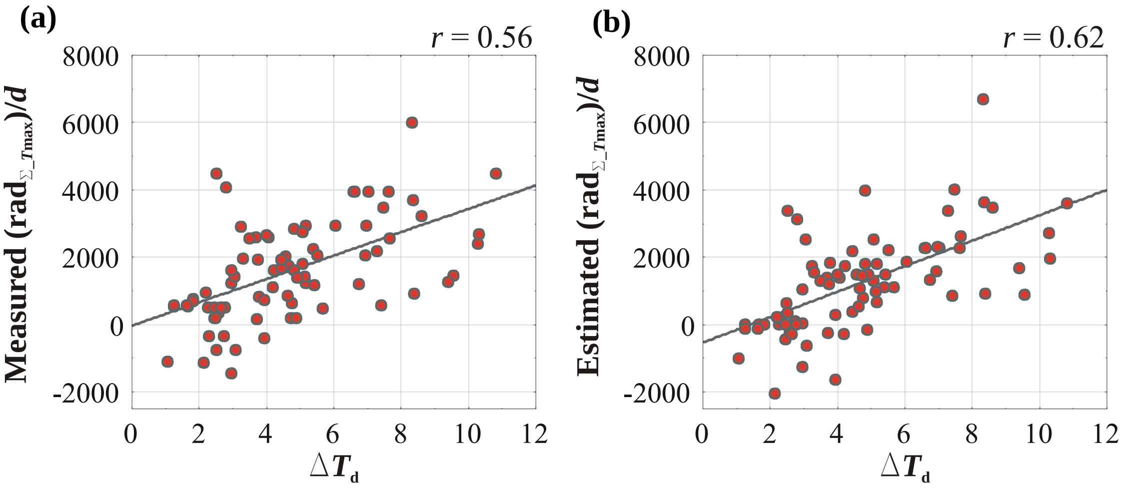

Figure 6.4: *Scatterplots of combined surface radiation terms having the highest significant Pearson correlations with daytime warming (ΔT_d). (a)* [ΣSW_$T_{\max}\cdot$(1-α)+ΣiLW_$T_{\max}$-ΣoLW_$T_{\max}$]/*d calculated from measured incoming radiation values and (b)* [ΣSW_$T_{\max}\cdot$(1-α)+ΣiLW_$T_{\max}$-ΣoLW_$T_{\max}$]/*d calculated from estimated incoming radiation values. Both surface radiation sums include outgoing long wave radiation values calculated from surface temperatures estimated using Equation B.18. The datasets consisted of measurements made at 10 and 15 cm depth (n = 80).*

Table 6.5: *Summary of Pearson correlation analysis between daytime warming* (ΔT_d) *measurements and combined surface radiation variables. The datasets consisted of measurements made at 10 and 15 cm depth (n = 80).*

Incoming radiation values	**Highest significant Pearson correlation with daytime warming (ΔT_d)**		
	Variable	***p***	***r***
Measured	[SW$_{\Sigma\_T\max}\cdot$(1-α) + iLW$_{\Sigma\_T\max}$ - oLW$_{\Sigma\_T\max}$]/*d* *	< 0.001	0.56
Estimated	[SW$_{\Sigma\_T\max}\cdot$(1-α) + iLW$_{\Sigma\_T\max}$ - oLW$_{\Sigma\_T\max}$]/*d* *	< 0.001	0.62

* *Combined term included outgoing long wave radiation values based on surface temperatures estimated using Equation B.18.*

6.5 Multivariate linear regression

After narrowing down potential predictor variables with correlation analyses, several combinations were assessed through multivariate linear regression against ΔT_d (Figure 6.5). Because the 10 and 15 cm depth dataset was not large enough to set aside a portion for model testing (n = 80), all data were included in the multivariate regression analysis. Predictor variables were removed from each combination if a significant ($p <$ 0.05) regression coefficient (B_i) was not identified during initial standard regression. The remaining predictor variables were then manually removed from the analysis one at a time to evaluate their effect on regression equation performance. Sections 6.5.1 and 6.5.2 summarize the multivariate linear regression results for variables based on measured and estimated incoming radiation values, respectively.

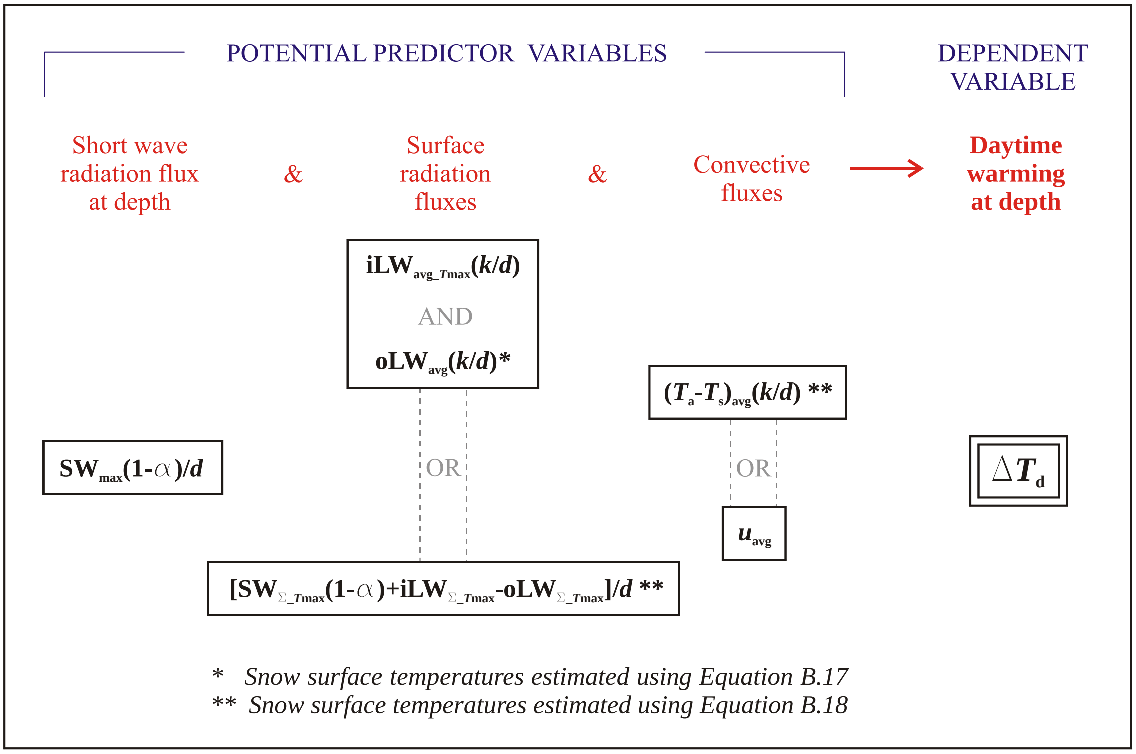

Figure 6.5: *Conceptual plan illustrating variables included in the multivariate linear regression analysis.*

6.5.1 Regression with measured incoming radiation values

For all combinations of predictor variables which included measured incoming short and long wave radiation values, the only significant term ($p < 0.05$) identified by multivariate regression analysis was $SW_{max} \cdot (1-\alpha)/d$. Regression results are summarized in Table 6.6. The regression intercept (B_0) is not included because it was small in magnitude (0.0441) and not significant ($p = 0.905$).

The statistical software used for this analysis, Statistica (Statsoft Inc.), reports the significance (p) of both the Kolmogorov-Smirnov (K-S) and the Lilliefors tests for normality in one of several ranges. The Lilliefors test adjusts the K-S p-value to account for estimation of the mean and standard deviation from the sample (Lilliefors, 1967). Normality of the regression residuals is not rejected at $p = 0.05$ using the K-S test ($D = 0.128$, $p < 0.15$), but is rejected with the Lilliefors test ($p < 0.01$). A scatterplot of residuals against predicted values and a normal probability plot of residuals are shown in Figure 6.6. The residual scatterplot (Figure 6.6(a)) indicates heteroscedasticity of the regression residuals.

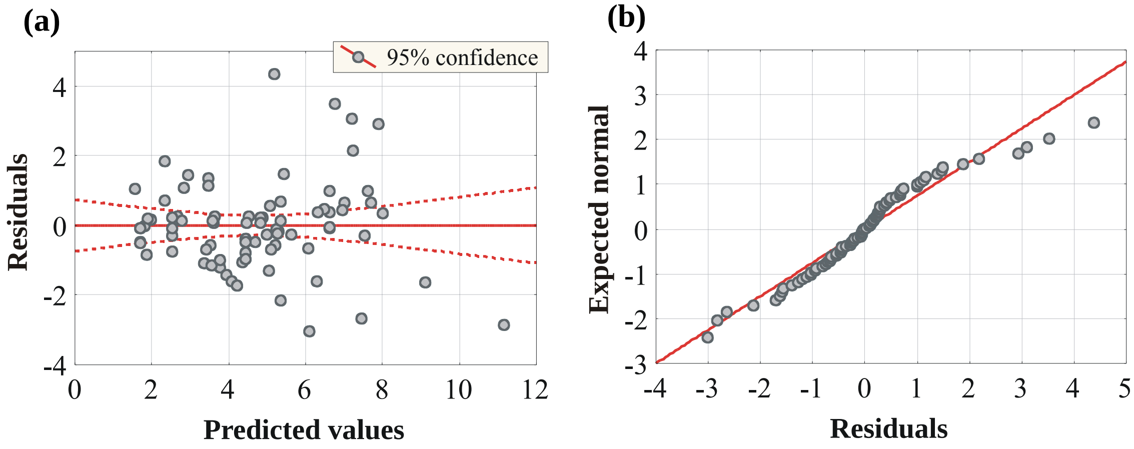

Figure 6.6: *Evaluation of residuals for multivariate regression based on measured incoming radiation values. (a) Scatterplot and (b) normal probability plot. These plots include all data in the 10 and 15 cm depth dataset (n = 80).*

Because the results of residual normality testing are ambiguous, the effect of outliers within the dataset was examined. Outliers were identified in terms of the standard deviation of the residuals (sigma). Table 6.6 includes regression coefficients (B_i), coefficients of determination (r^2) and standard errors of estimation (SEE) for the dataset with statistically identified outliers (residual > 3·sigma; residual > 2·sigma) removed ($n = 79$; $n = 73$). Results indicate that the regression coefficients are not sensitive to outliers in the dataset. For the $n = 79$ dataset, normality of the residuals is not rejected using the K-S test ($D = 0.109$, $p > 0.20$), but is again rejected with the Lilliefors test ($p < 0.05$). With all statistically identified outliers removed ($n = 73$), normality of the regression residuals is not rejected with either the K-S or Lilliefors tests ($D = 0.073$, $p > 0.20$; $p > 0.20$).

Table 6.6: *Summary of multivariate linear regression results for predictor variables based on measured incoming radiation values. The only significant term identified by multivariate regression analysis was* $SW_{max}\cdot(1-\alpha)/d$. *Results are presented for the complete dataset and for the dataset with statistically identified outliers removed.*

Outliers removed	***n***	**B_i**	**Standard error of B_i**	**p of B_i**	**Adjusted r^2**	**SEE (°C)**
none	80	0.00463	0.000336	< 0.001	0.70	1.28
residual > 3·sigma	79	0.00460	0.000312	< 0.001	0.74	1.19
residual > 2·sigma	73	0.00468	0.000264	< 0.001	0.81	0.87

The statistically identified outliers were examined to see if they represent physically anomalous conditions (Table 6.7). The outliers displayed no trends in measurement depth, Julian day, slope, aspect, sky condition or average wind speed that were unexpected or inconsistent with the distribution of these parameters within the entire 10 and 15 cm depth dataset. The occurrence of surface hoar (SH) crystals as the surface form for all of the outliers is conspicuous; however, surface hoar is present in 50% of data. Visual examination of the data points (Figure 6.7) does not indicate any substantial trends other than, perhaps, greater scatter in measured ΔT_d when surface hoar was present. Other factors like changing sky conditions over the day or changing snowpack characteristics over terrain may account for some or much of this variability; the increased scatter is not clearly associated with surface grain form.

Table 6.7: *Summary of outlier parameters examined for physically-based trends. Outliers were identified statistically (residual* > 2·sigma*).*

Outlier	**ΔT_d**	**d (cm)**	**Year**	**Julian day**	**Slope (º)**	**Aspect (º)**	**Average sky condition**	**Surface grain form**	**u_{avg} (m/s)**
1 *	9.55	10	2006	50	20	108 (E)	BKN	SH	0.18
2	3.05	15	2005	59	0	TOP	FEW	SH	0.37
3	4.80	15	2005	59	12	162 (S)	FEW	SH	0.37
4	8.31	10	2005	59	12	162 (S)	FEW	SH	0.37
5	10.26	10	2006	41	14	164 (S)	FEW	SH	0.83
6	10.28	10	2006	50	23	212 (SW)	BKN	SH	0.18
7	10.79	10	2006	42	14	164 (S)	CLR	SH	0.35

* *Residual* > 3·sigma.

The most interesting result to come out of the outlier analysis pertains to the year in which the data were measured. From Table 6.7, it is apparent that the outliers associated with lower values of ΔT_d were collected in 2005, while those associated with higher values of ΔT_d were collected in 2006. When the data are plotted, a general trend of lower ΔT_d measurements in 2005 is noticeable. Figure 6.8 illustrates the complete dataset, split by year, and includes regression lines based on data from both years (n = 79), data from 2005 (n = 16) and data from 2006 (n = 63).

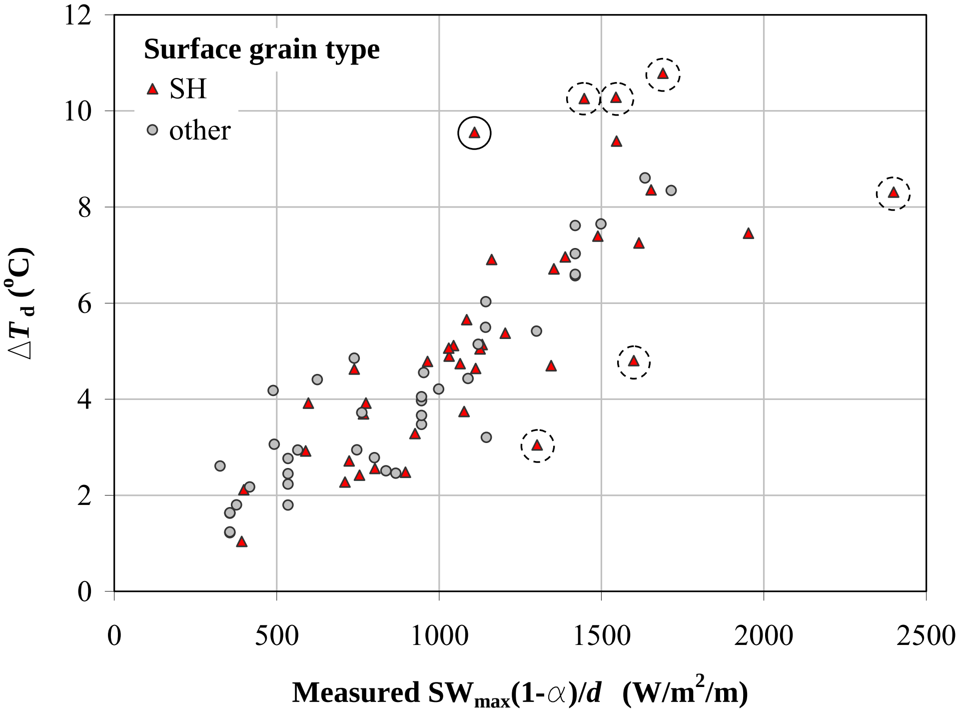

Figure 6.7: *Scatterplot of daytime warming* (ΔT_d) *against measured* $SW_{max}\cdot(1-\alpha)/d$, *grouped by surface grain type (surface hoar (*SH*) or other). This plot includes all data in the 10 and 15 cm depth dataset (n = 80). Statistical outliers are identified by dashed (residual > 2**sigma*) and solid (residual > 3**sigma*) circles.*

While general differences in weather patterns or snowpack characteristics could contribute to differences in the ΔT_d data collected each year, the change in field equipment is also a possible explanation. The measurement error analysis (Appendix A) indicated that the magnitude of temperature measurements was similar in each year, but a detailed comparison of side by side measurements made with both sets of field equipment was not undertaken. A Mann-Whitney *U*-test on the 10 and 15 cm depth dataset, using ΔT_d divided by measured $SW_{max}\cdot(1-\alpha)/d$ as the comparison variable, indicated a significant difference ($z = -2.86$, $p = 0.004$) between the 2005 and 2006 data groups. The division of ΔT_d by the short wave radiation parameter normalizes the data, at least

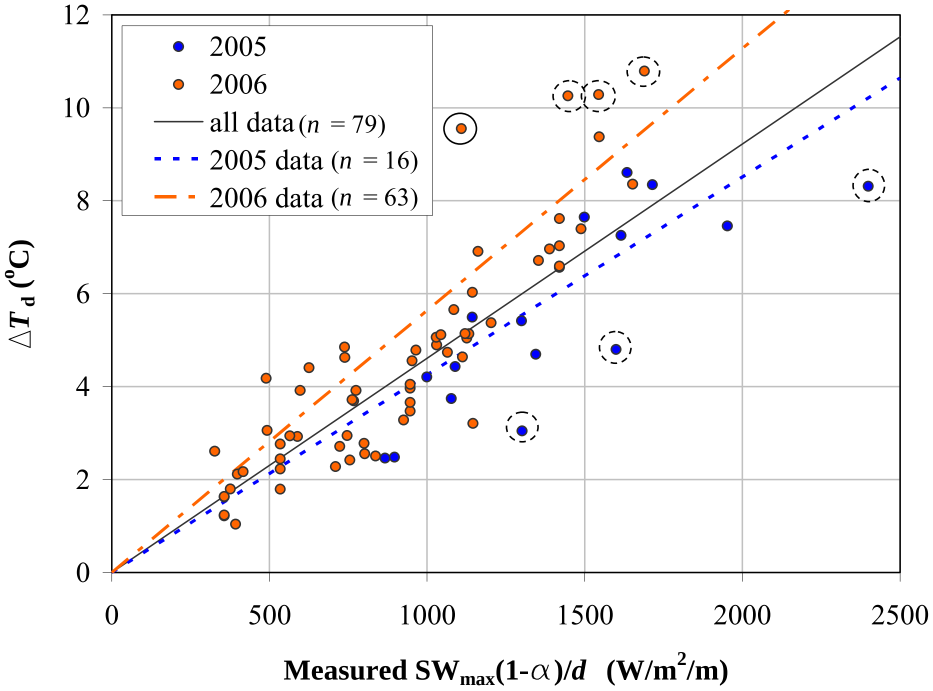

Figure 6.8: *Scatterplot of daytime warming* (ΔT_d) *against measured* $\mathrm{SW}_{\max}\cdot(1-\alpha)/d$, *grouped by year. This plot includes all data in the 10 and 15 cm depth dataset (n = 80). Statistical outliers are identified by dashed (residual > 2*sigma) and solid (residual > 3*sigma) circles. The solid line illustrates the regression equation for all data, with one outlier (residual > 3*sigma) removed (n = 79). The dashed lines illustrate the regression equations for data collected in 2005 (n = 16) and for data collected in 2006 with the same outlier removed (n = 63).*

partially, for differences in depth, slope, aspect, time of year and sky condition. As noted previously, however, other parameters that vary from year to year, such as the properties of the upper snowpack layers, have not been considered in this analysis and may also have contributed to yearly differences in ΔT_d.

Probable measurement errors associated with the field equipment typically correspond to temperature measurements warmer than the actual snow temperature (Section 2.1, Section A.1). The data suggest that temperature measurement errors may have been higher with the 2006 equipment than with the 2005 equipment; some ideas as to why this may be the case are presented in Section 7.1. As the 2005 dataset is very small, warming model development based only on these data is not feasible. Figure 6.8 illustrates the approximate variation in the magnitude of modelled ΔT_d as a result of yearly data differences. The combined data model would overestimate ΔT_d by less than 1 ºC relative to the value estimated from the 2005 data alone

6.5.2 Regression with estimated incoming radiation values

When predictor variables that included estimated incoming short and long wave radiation values were combined with wind speed, the only significant term ($p < 0.05$) identified by multivariate regression analysis was again $SW_{max} \cdot (1-\alpha)/d$. The regression intercept (B_0) was not significant ($p = 0.448$) and had a standard error larger than the magnitude of B_0. Normality of the regression residuals is not rejected at $p = 0.05$ using either the K-S test ($D = 0.096$, $p > 0.20$) or the Lilliefors test ($p < 0.10$). A scatterplot of residuals against predicted values and a normal probability plot of residuals are included in Figure 6.9. The residual scatterplot (Figure 6.9(a)) again indicates heteroscedasticity of the regression residuals.

Statistical methods did not identify any outliers with a regression residual greater than 3·sigma. Of the five statistically identified outliers (residual > 2·sigma), four correspond to cases that were identified and discussed in the previous section. The exception is a ΔT_d measurement made on a southeast slope on 5 March 2006, a day on which variable thin cloud cover was observed. Although other measurements made on this day do not show up as outliers, the estimated maximum incoming short wave radiation values are approximately 60% of the measured values. This case illustrates sky

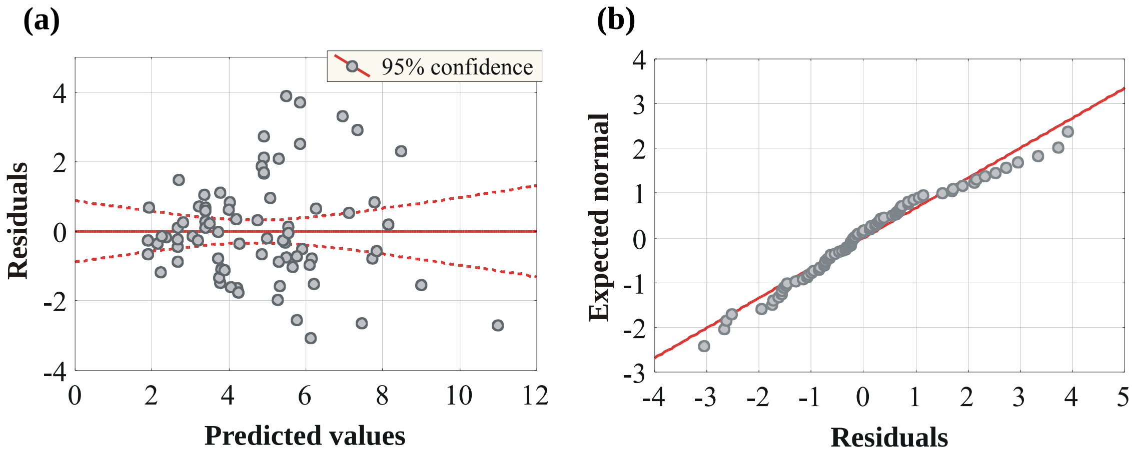

Figure 6.9: *Evaluation of residuals for multivariate regression based on estimated incoming radiation values. (a) Scatterplot and (b) normal probability plot. These plots include all data in the 10 and 15 cm depth dataset (n = 80).*

conditions (variable thin cloud) for which it is difficult to accurately estimate incoming short wave radiation with a simple parameterization.

Comparison of the regression results based on estimated incoming short wave radiation values with and without statistically identified outliers (Table 6.8) indicates a little more sensitivity to outliers than observed with the measured incoming short wave radiation values (Table 6.6). The estimated incoming short wave radiation regression equation based on the complete dataset (n = 80) results in slightly warmer ΔT_d estimates than that based on the dataset with all outliers removed (n = 75); the maximum difference within the typical range of the dataset is approximately 1 ºC.

Combining the predictor variables based on estimated incoming short and long wave radiation values with $(T_a\text{-}T_s)_{avg}\cdot(k/d)$ in the regression analysis produced additional significant regression terms. This occurred with individual surface radiation fluxes and with the combined surface radiation flux (Table 6.9). The adjusted r^2 and standard error of estimate (SEE) values are very similar for both equations.

Table 6.8: *Summary of multivariate linear regression results for predictor variables based on estimated radiation fluxes in combination with wind speed. The only significant term identified by multivariate regression analysis was* $\mathrm{SW}_{\mathrm{max}}\cdot(1\text{-}\alpha)/d$. *Results are presented for the complete dataset and for the dataset with statistically identified outliers removed.*

Outliers removed	***n***	$\boldsymbol{B_{\mathrm{i}}}$	**Standard error of** $\boldsymbol{B_{\mathrm{i}}}$	***p* of** $\boldsymbol{B_{\mathrm{i}}}$	**Adjusted** $\boldsymbol{r^2}$	**SEE (ºC)**
none	80	0.00549	0.000482	< 0.001	0.62	1.46
residual > 2·sigma	75	0.00508	0.000408	< 0.001	0.68	1.19

Table 6.9: *Summary of multivariate linear regression results for predictor variables based on estimated radiation fluxes in combination with* $(T_{\mathrm{a}}\text{-}T_{\mathrm{s}})_{\mathrm{avg}}\cdot(k/d)$. *The analysis was undertaken with the complete 10 and 15 cm depth dataset (n = 80).*

Significant predictor variables	$\boldsymbol{B_{\mathrm{i}}}$	**Standard error of** $\boldsymbol{B_{\mathrm{i}}}$	***p* of** $\boldsymbol{B_{\mathrm{i}}}$	**Adjusted** $\boldsymbol{r^2}$	**SEE (ºC)**
$\mathrm{SW}_{\mathrm{max}}\cdot(1\text{-}\alpha)/d$	0.00562	0.000745	< 0.001	0.72	1.26
$\mathrm{iLW}_{\mathrm{avg}\ T\mathrm{max}}\cdot(k/d)$	-0.0910	0.0292	0.003		
$\mathrm{oLW}_{\mathrm{avg}}\cdot(k/d)$	0.0952	0.0292	0.002		
$(T_{\mathrm{a}}\text{-}T_{\mathrm{s}})_{\mathrm{avg}}\cdot(k/d)$ *	-0.714	0.168	0.002		
B_0	-1.40	0.696	0.047		
$\mathrm{SW}_{\mathrm{max}}\cdot(1\text{-}\alpha)/d$	0.00910	0.000958	< 0.001	0.71	1.27
$[\mathrm{SW}_{\Sigma\ T\mathrm{max}}\cdot(1\text{-}\alpha) + \mathrm{iLW}_{\Sigma\ T\mathrm{max}} - \mathrm{oLW}_{\Sigma\ T\mathrm{max}}]/d$	-0.00054	0.000191	0.006		
$(T_{\mathrm{a}}\text{-}T_{\mathrm{s}})_{\mathrm{avg}}\cdot(k/d)$ *	-0.717	0.141	< 0.001		
B_0	-1.409	0.539	0.011		

* *Snow surface temperature estimated using Equation B.18.*

As noted previously, there is a cross-correlation problem with incoming and outgoing long wave radiation; for the estimated values, the Pearson correlation between these variables is 0.96. If either parameter is removed from the individual surface flux analysis, only estimated $\mathrm{SW}_{\mathrm{max}}\cdot(1\text{-}\alpha)/d$ and $(T_{\mathrm{a}}\text{-}T_{\mathrm{s}})_{\mathrm{avg}}\cdot(k/d)$ remain as significant predictor variables.

While inclusion of the combined surface radiation flux term appears to improve regression model performance, it also complicates the input data requirements. Because the radiation sums are based on the sunrise to maximum snow temperature time period, calculation of the combined term requires some knowledge of the time at which the peak snow temperature will occur. Before attempting to develop a method to estimate the 'T_{max}' time, the regression was repeated without the combined surface radiation flux term to evaluate its importance.

Table 6.10 includes the results of the regression analysis with $\mathrm{SW}_{\mathrm{max}} \cdot (1-\alpha)/d$ and $(T_a - T_s)_{\mathrm{avg}} \cdot (k/d)$ as predictor variables. The regression intercept (B_0) was not significant ($p = 0.375$) and had a standard error larger than the magnitude of B_0. While the adjusted r^2 and SEE values show some decrease in fit relative to the regression equation including the combined surface radiation term, the difference is limited (adjusted r^2 decreased from 0.71 to 0.68, SEE increased from 1.27 to 1.33 ºC). The fact that the combined surface radiation term did not show up as a significant predictor variable in the analysis using measured incoming radiation values suggests that performance of the 'estimated radiation' model may benefit more from improving the incoming short wave radiation parameterization than from inclusion of a combined surface radiation term. For these reasons, the combined surface radiation term was not investigated further as a predictor variable.

Table 6.10: *Summary of multivariate linear regression results with estimated* $SW_{max} \cdot (1-\alpha)/d$ *and* $(T_a\text{-}T_s)_{avg} \cdot (k/d)$ *as predictor variables. The analysis was undertaken with the complete 10 and 15 cm depth dataset (n = 80).*

Significant predictor variables	B_i	Standard error of B_i	p of B_i	Adjusted r^2	SEE (ºC)
$SW_{max} \cdot (1-\alpha)/d$	0.00681	0.000545	< 0.001	0.68	1.33
$(T_a\text{-}T_s)_{avg} \cdot (k/d)$ *	-0.550	0.134	<0.001		

* *Snow surface temperature estimated using Equation B.18.*

Table 6.11 includes the results of a regression analysis with $SW_{max} \cdot (1-\alpha)/d$ and $(T_a\text{-}T_s)_{avg}/d$ as predictor variables. Again, the regression intercept (B_0) was not significant (p = 0.531) and had a standard error larger than the magnitude of B_0. The resultant changes in adjusted r^2 and SEE are quite small (adjusted r^2 decreased from 0.68 to 0.67, SEE increased from 1.33 to 1.35 ºC). Although inclusion of some measure of snow conductivity with surface energy flux parameters makes physical sense, removing k from the warming model simplifies the input requirements. Without k, the only remaining snowpack parameter is albedo (α), which is determined from the number of days since snowfall. Difficulty in estimating k from limited and spatially variable snowpack observations is avoided.

Table 6.11: *Summary of multivariate linear regression results with estimated* $SW_{max} \cdot (1-\alpha)/d$ *and* $(T_a\text{-}T_s)_{avg}/d$ *as predictor variables. The analysis was undertaken for the complete 10 and 15 cm dataset (n = 80) and with statistically identified outliers (residual > 2·sigma) removed from the dataset (n = 74).*

n	Significant predictor variables	B_i	Standard error of B_i	p of B_i	Adjusted r^2	SEE (ºC)
80	$SW_{max} \cdot (1-\alpha)/d$	0.00661	0.000543	< 0.001	0.67	1.35
	$(T_a\text{-}T_s)_{avg} / d$ *	-0.0276	0.00756	< 0.001		
74	$SW_{max} \cdot (1-\alpha)/d$	0.00691	0.000478	< 0.001	0.76	1.07
	$(T_a\text{-}T_s)_{avg} / d$ *	-0.0277	0.00618	< 0.001		

* *Snow surface temperature estimated using Equation B.18.*

Normality of the residuals from the $SW_{max}\cdot(1-\alpha)/d$ and $(T_a-T_s)_{avg}/d$ regression is not rejected at $p = 0.05$ using either the K-S test ($D = 0.084$, $p > 0.20$) or the Lilliefors test ($p < 0.20$). A scatterplot of residuals against predicted values and a normal probability plot of residuals are included in Figure 6.10. The residual scatterplot (Figure 6.10(a)) again indicates heteroscedasticity of the regression residuals. Statistical methods identified six outliers (residual > 2·sigma); none have a regression residual greater than 2.5·sigma. Five of the outliers correspond to cases which were analyzed previously, and a physical explanation for the sixth was not apparent. Regression analysis repeated with the six statistically identified outliers removed resulted in small changes to the regression coefficients (Table 6.11).

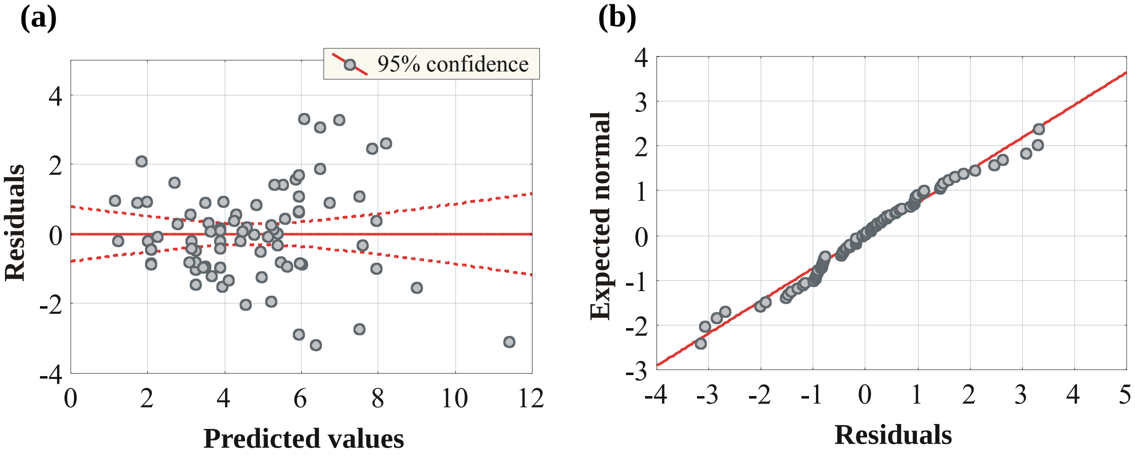

Figure 6.10: *Evaluation of residuals for multivariate regression based on estimated* $SW_{max}\cdot(1-\alpha)/d$ *and* $(T_a-T_s)_{avg}/d$. *(a) Scatterplot and (b) normal probability plot. These plots include all data in the 10 and 15 cm depth dataset (n = 80).*

6.5.3 Additional predictor variables

To confirm that no strong, readily available predictor variables had been missed in the regression analysis, a few additional parameters were tested individually with measured $SW_{max} \cdot (1-\alpha)/d$. Examples are Julian day, average relative humidity, aspect and a dichotomous measure of snow surface grain form (i.e. SH = 1, other = 0). Most of these parameters were considered indirectly in the previous analyses through their influence on the key surface energy flux variables. None were identified as a significant ($p < 0.05$) predictor variable for ΔT_d when combined with measured $SW_{max} \cdot (1-\alpha)/d$.

6.6 Warming model verification

Because the dataset was not large enough to set aside a portion for model testing, options for model verification were limited. Two comparisons were undertaken; one based on field data and the other on output from the SNOWPACK model.

6.6.1 Field data interpolated at 12.5 cm depth

The warming model was developed using data interpolated at 10 and 15 cm depth. To generate some data for model testing purposes, temperature measurements were subsequently interpolated at 12.5 cm depth. Because the actual measurement interval (2 to 3 cm) was less than the original 5 cm interpolation interval, the 12.5 cm data should be somewhat independent of the model building dataset. Three versions of the warming model were tested, as summarized in Table 6.12; in all cases, regression coefficients used for this comparison reflect those determined from the original 10 and 15 cm depth dataset with any outliers identified by residual values greater than 3·sigma removed. As for model development, the maximum incoming short wave radiation value was determined from hourly measurements or hourly estimated values. The average difference between air and surface temperatures was calculated from air temperature measurements made in the Mount Fidelity study plot (0700 and 1200) and Equation B.18. Although the adjusted r^2 values are lower than for the original regression analysis, the SEE values are indicative of reasonable model performance.

Table 6.12: *Evaluation of warming model performance with data interpolated at 12.5 cm depth from field measurements (n = 39).*

Predictor variables	B_i **	**Initial reference**	**adjusted r^2**	**SEE (°C)**
$m\mathrm{SW}_{max}\cdot(1-\alpha)/d$ *	0.00460	Table 6.6	0.57	1.09
$e\mathrm{SW}_{max}\cdot(1-\alpha)/d$ *	0.00549	Table 6.8	0.48	1.15
$e\mathrm{SW}_{max}\cdot(1-\alpha)/d$ *	0.00661	Table 6.11	0.53	1.11
$(T_a-T_s)_{avg}$ / d	-0.0276			

* *Prefixes refer to the use of (m)easured or (e)stimated hourly incoming short wave radiation values to determine* SW_{max}.

** *Coefficients determined during regression analysis with 10 and 15 cm dataset (outliers with residual > 3·sigma removed).*

6.6.2 SNOWPACK output

Using SNOWPACK output for verification of the warming models is appealing because ΔT_d values can be generated for aspects on which no field data were collected. With limited verification of the near surface temperatures modelled by SNOWPACK, however, it will not be possible to determine whether discrepancies result from inaccuracy originating with SNOWPACK, the semi-empirical models, or both. Comparison of SNOWPACK model output with knoll top field measurements (Section 5.3.3) indicated that SNOWPACK had a tendency to overestimate ΔT_d by approximately 24%.

Assuming a homogeneous snow profile over the entire knoll (based on knoll top observations made on 6 February 2006), SNOWPACK modelling was completed for the knoll top and eight different aspects. The slope angle was set to 30º for all knoll slopes. Snow temperatures at 10 and 15 cm depth were extracted from the SNOWPACK output and ΔT_d values were calculated at both depths for 7, 8, 10 and 11 February 2006. This resulted in 72 data points. A SNOWPACK model run based on data from the early February 2006 field experiment was selected because of its length and because it included days with different cloud cover conditions.

Results are summarized in Table 6.13 for the three versions of the semi-empirical warming model discussed in Section 6.6.1. The adjusted r^2 values indicate strong correlations between SNOWPACK output and the semi-empirical warming models. If the SNOWPACK generated ΔT_d values are reduced by 24% (as suggested by the knoll top field data comparison), improvement in the SEE values is observed. Inclusion of the $(T_a\text{-}T_s)_{avg}/d$ term in the semi-empirical warming model did not improve fit relative to the SNOWPACK generated data.

Table 6.13: *Evaluation of warming model performance with SNOWPACK generated data (n = 72). The adjusted r^2 values are the same with the scaled and unscaled SNOWPACK data.*

Predictor variables	**adjusted r^2**	**SEE (ºC)**	
		SNOWPACK ΔT_d	**scaled SNOWPACK ΔT_d ****
$m\mathrm{SW}_{max}\cdot(1\text{-}\alpha)/d$ *	0.88	1.35	1.09
$e\mathrm{SW}_{max}\cdot(1\text{-}\alpha)/d$ *	0.91	1.19	0.96
$e\mathrm{SW}_{max}\cdot(1\text{-}\alpha)/d$ * $(T_a\text{-}T_s)_{avg} / d$	0.76	1.93	1.56

* *Prefixes refer to the use of (m)easured or (e)stimated hourly incoming short wave radiation values to determine* SW_{max}.

** SNOWPACK *data which have been reduced by 24%.*

The ΔT_d values calculated with the semi-empirical warming model based on measured short wave radiation values (Table 6.6) are plotted against the scaled SNOWPACK values in Figure 6.11. No trends are apparent when the data are grouped by aspect (Figure 6.11(a)), which suggests that the uneven distribution of aspects within the model development dataset did not bias the model. Because projection of the incoming short wave radiation values accounts for slope angle and aspect, this is an encouraging, but not unexpected, result.

The semi-empirical warming model provides ΔT_d values that are consistently lower than the SNOWPACK model output, even with the 24% reduction. When the data are grouped by sky condition (Figure 6.11(b)), it appears that the difference increases as the cloud cover decreases. As noted previously, further field data and verification of both models is required to determine why the results differ.

6.7 Warming model limitations

Limitations to the semi-empirical warming models arise both from the simplicity of their data input requirements and from limitations in the dataset. Factors which will affect performance of the semi-empirical models, some of which have been noted previously, are discussed below.

Because incoming short wave radiation is the primary (and in most cases only) significant predictor variable, modelled ΔT_d values are sensitive to the accuracy of the incoming short wave radiation estimate. Neither thin cloud nor variation in cloud cover over the day are well represented by the simple incoming short wave parameterization used for model development. For the linear regression analysis, the maximum estimated

(a)

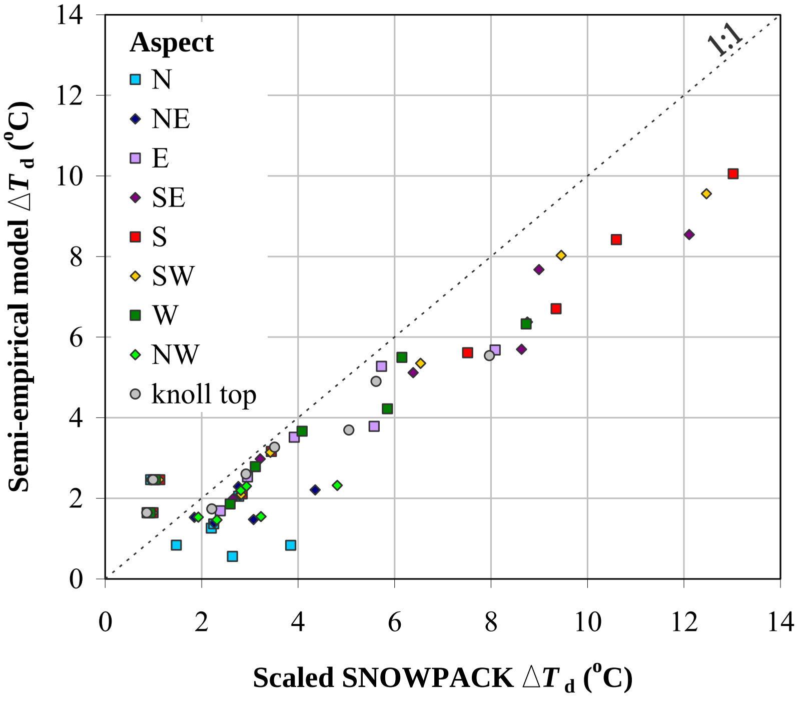

(b)

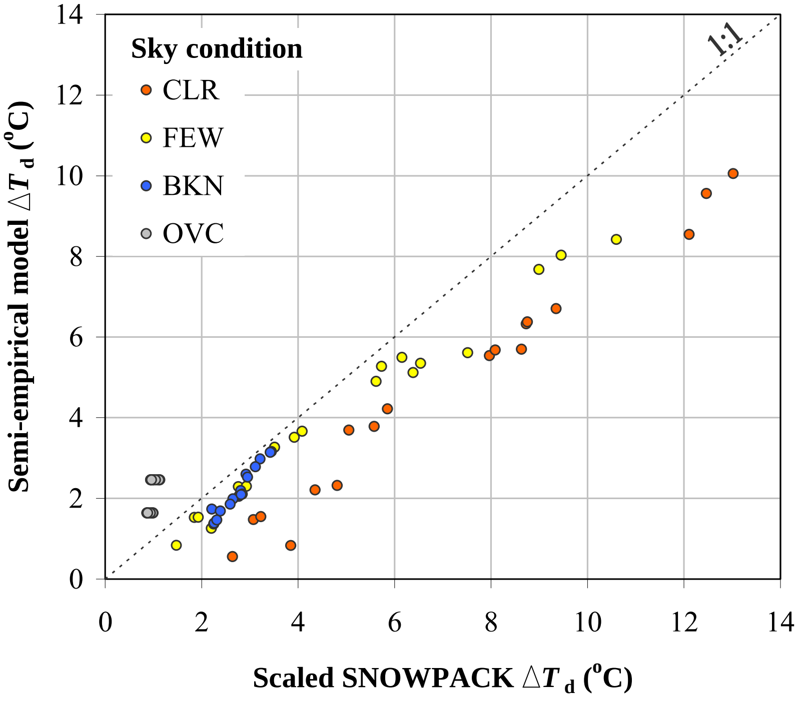

Figure 6.11: *Comparison between scaled SNOWPACK model output (ΔT_d reduced by 22%) and the semi-empirical warming model based on measured incoming short wave radiation values (n = 72). Data have been grouped by (a) aspect and (b) sky condition.*

incoming short wave radiation value was determined from hourly cloud cover observations. If a single average cloudiness value, calculated from the hourly observations, is used instead, model performance decreases slightly (adjusted r^2 decreases from 0.62 to 0.54, SEE increases from 1.46 to 1.60 ºC). The results based on a daily average cloudiness value are more indicative of how the model will perform during operational use, although errors will vary in magnitude depending on how variable the cloud conditions are. As the incoming short wave radiation calculations do not account for the opacity of the cloud cover, the model will have a tendency to overestimate the effect of the cloud cover and underestimate daytime warming on days with thin cloud.

Eliminating snowpack parameters like conductivity and the short wave radiation extinction coefficient from the warming model simplified the model input. The fact that model performance did not decrease substantially without these parameters suggests that they did not have a strong influence on ΔT_d measurements made during the field experiments. As noted in Section 4.3, however, the methods used to estimate these snowpack dependent properties may not be applicable for snow layers like melt freeze crusts. In addition, the field data were not exhaustive with respect to the variation in near-surface snowpack layers observed in mountainous terrain. Under some conditions not represented in the dataset, like the presence of a thick near-surface crust, the effects of conductivity or short wave radiation extinction with depth may be critical.

On a similar note, the albedo estimate which worked best with the field dataset did not distinguish between wet or dry snow crystals on the surface. After removing cases in which melting was identified at 10 and 15 cm depths, no data corresponding to wet surface snow grains remained. Additional data are required to verify whether the albedo parameterization used is adequate when wet snow grains are present on the snow surface.

Because the semi-empirical models do not consider the initial snow temperature at depth and have no way to distinguish between energy that contributes to melting rather than temperature change, results are not valid when isothermal (0 ºC) conditions are encountered in the upper snowpack layers.

All of the field data were collected on days without substantial wind or precipitation. Heat exchange at the snow surface resulting from precipitation or convection, neither of which is considered in the semi-empirical models, may become important under these weather conditions. Again, additional data are required to assess the implications with respect to performance of the semi-empirical models.

The semi-empirical models were developed using temperature data measured at 10 and 15 cm depth. As noted in Section 6.4.2, the correlation coefficients between ΔT_d and measured $SW_{max} \cdot (1-\alpha)/d$ decreased considerably at 20 and 25 cm depth. Performance of the semi-empirical models is expected to decrease accordingly at these depths. Due to concerns regarding temperature measurement errors at depths less than 10 cm, data collected close to the snow surface were excluded from the analysis. Improvements in field measurement methods are required before performance of the simple models can be assessed at depths less than 10 cm.

Although variation in tree cover on Gopher Butte knoll did not appear to affect the ΔT_d measurements at 10 and 15 cm depths, insufficient data were collected to suggest that tree cover does not influence the surface energy balance; modelled values may be suspect in thickly treed areas. Because the magnitude of incoming short wave radiation can be adjusted for the effects of tree cover (i.e. Koivusalo and Kokkonen, 2002; Sicart et al., 2003) the potential to account for tree cover in the semi-empirical models is there. The same is true for adjustment of incoming short wave radiation values to account for shading by nearby terrain features.

6.8 Output display

As noted in the introduction to this chapter, ease of use and ease of output interpretation are important if the simple warming model is to be applied operationally. Although display of the warming model output over terrain using Geographic Information Systems (GIS) was considered initially, it was rejected at this stage. The calculation requirements are simple enough that a spreadsheet is sufficient for model application and has the advantage of not requiring any specialized software. This is a benefit both in accessibility and in user-friendliness. The example shown in Figure 6.12, prepared using a standard Microsoft Excel chart option, provides the output visually and in tabular form. Generalized model output, like the example, also avoids the suggestion of greater model complexity than is actually present. Until further data are available for verification and additional factors like terrain effects, spatial variability in snowpack characteristics and tree cover are better accounted for in the model, display over detailed topography is not warranted.

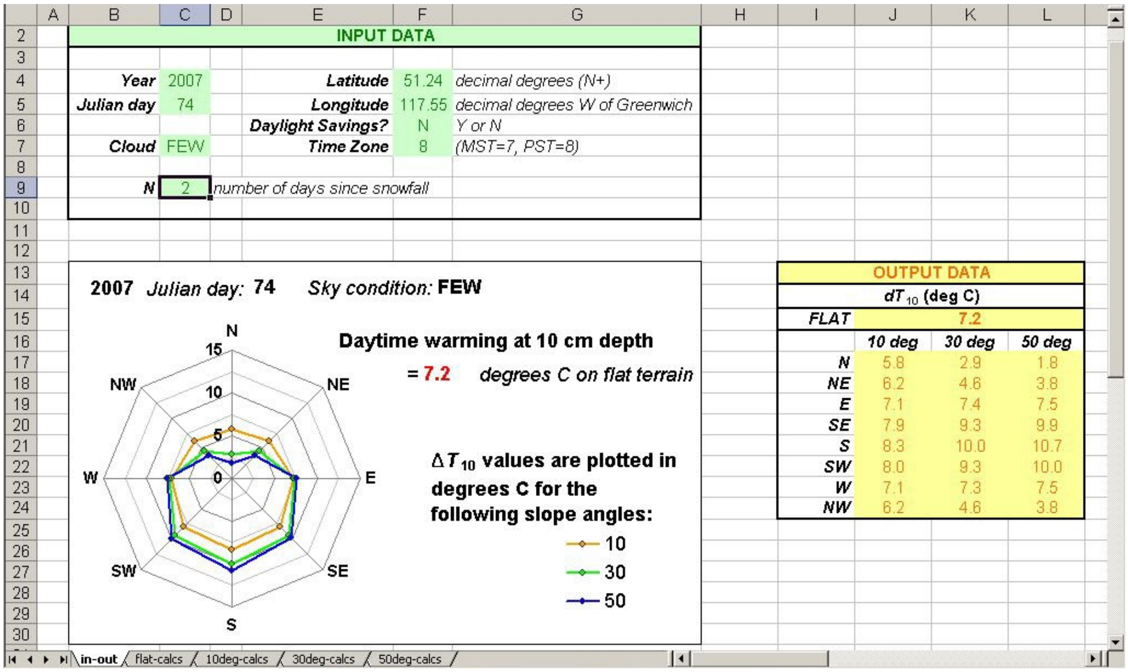

INPUT DATA

Year 2007
Julian day 74
Cloud FEW
Latitude 51.24 decimal degrees (N+)
Longitude 117.55 decimal degrees W of Greenwich
Daylight Savings? N Y or N
Time Zone 8 (MST=7, PST=8)
N 2 number of days since snowfall

2007 *Julian day:* **74** *Sky condition:* **FEW**

Daytime warming at 10 cm depth

= **7.2** *degrees C on flat terrain*

ΔT_{10} values are plotted in degrees C for the following slope angles:

OUTPUT DATA

***dT*₁₀ (deg C)**			
FLAT	**7.2**		
	10 deg	***30 deg***	***50 deg***
N	5.8	2.9	1.8
NE	6.2	4.6	3.8
E	7.1	7.4	7.5
SE	7.9	9.3	9.9
S	8.3	10.0	10.7
SW	8.0	9.3	10.0
W	7.1	7.3	7.5
NW	6.2	4.6	3.8

Figure 6.12: *Model output example based on a Microsoft Excel spreadsheet.*

CHAPTER SEVEN: CONCLUSIONS

7.1 Conclusions

The snow surface energy balance has been the focus of much research, particularly with respect to snowmelt applications. This study is one of few in which field measurements of near-surface snow temperatures were made. No references to previous studies that included measuring or modelling the distribution of daytime warming over terrain were found in the literature review.

Despite steps taken to match equipment properties to those of snow, near-surface temperature data collected during this study indicated that measurement errors were present. The magnitude of these errors was estimated to be less than 0.3 ºC at 10 cm depth. Analysis of the daytime warming data suggested that measurements made in 2005 were subject to smaller errors than those measured in 2006. Following the hypothesis of Rowlands et al. (2002), who suggested that tree needles remained relatively cool when exposed to solar radiation because of their high surface area to mass ratio, the higher surface area to mass ratio of the balsa wood covers used in 2005 may have contributed to better measurement accuracy. Setting the thermocouple tips slightly under the end of the covers may also have helped to reduce measurement errors.

Based on evaluation of the near-surface temperature data collected in the winters of 2005 and 2006, the following observations regarding variation in daytime warming were made:

- The magnitude of measured daytime warming typically decreased with depth below the snow surface.

- Effects of aspect were observed in the daytime warming measurements; these were attributed to variation in radiation input and to variation in snowpack properties, both over time and over terrain.
- Aspect-dependent differences in daytime warming were observed to decrease with increasing cloud cover and as the February to April measurement period progressed.
- Observations indicated that variation in cloud cover over the day altered the distribution of daytime warming over terrain.
- The upper snowpack exhibited substantial daytime warming under thin cloud conditions.

A comparison of the field data with near-surface temperatures modelled using the Swiss snowpack evolution model SNOWPACK indicated reasonable agreement. The average difference between measured and modelled values at 10 cm depth was approximately 1.5 ºC. Daytime warming values generated using SNOWPACK were not used in subsequent development of the simpler semi-empirical warming models because SNOWPACK tended to overestimate the magnitude of daytime warming relative to the field data.

Semi-empirical models were developed from the field measurements of daytime warming. Data for verification were limited, but the simple models showed promise. With simple input requirements of Julian day, latitude, longitude, aspect, slope angle, number of days since snowfall and estimated daily cloudiness, the magnitude of daytime warming, at depths of 10 to 15 cm, was predicted with a standard error of estimation of approximately 1.6 ºC. Although many different potential predictor variables were included in the model building process, the maximum daily incoming short wave radiation value proved to be, by far, the strongest.

7.2 Recommendations for further research

Further field data are required for verification of the semi-empirical warming models. Data collected under the following conditions would be particularly useful to supplement gaps in the current dataset:

- thick near-surface crusts
- wet grains on the snow surface
- west-facing slopes
- steep north-facing slopes
- slopes with varying tree cover
- moderate to strong wind

Additional field measurements made closer to the snow surface (< 10 cm depth) are also necessary before the semi-empirical models can be applied with confidence at shallower depths. Collection of accurate data closer to the snow surface will require improvement in field techniques for near-surface temperature measurement.

Because the semi-empirical models are strongly dependent on incoming short wave radiation values, better estimates of incoming short wave radiation would also be beneficial. Areas of potential improvement include the following:

- adjustment for cloud opacity

- adjustment for cloud cover variation over the day
- adjustment for tree cover
- adjustment for shading by and long wave radiation emission from nearby terrain

Spatial variability in the upper snowpack layers appeared to explain some of the aspect-dependent differences observed in the measured daytime warming values. Although parameters like the short wave radiation extinction coefficient and conductivity were not identified as useful predictor variables in the model building process, this may have resulted from difficulty in determining realistic values from standard snowpack observations. Use of a distributed snowpack evolution model in combination with a distributed energy balance model seems the ideal approach for accurate modelling of near-surface temperatures. Complex models like SNOWPACK and CROCUS have potential, but further development and verification with field data are required. Operational use in western Canada is currently limited by availability of input data.

Field measurements of near-surface temperature, like those collected for this study, will allow examination of other processes driven by near-surface temperature fluctuations. Examples are spatial variation in crust formation/deterioration and the distribution of near-surface facets over terrain. Further study regarding variation in the timing of near-surface warming would also be useful. Avalanche forecasters are concerned with snowpack stability and, ultimately, information and observations linking daytime warming directly to avalanche activity will be of most value for stability evaluation.

REFERENCES

Adams, E.E., and Sato, A. (1993). Model for effective thermal conductivity of a dry snow cover composed of uniform ice spheres. *Annals of Glaciolgy*, 18, 300-304.

Aggarwal, R.K., Ravi, M.R., and Mahajan, P. (2006). A snow microstructure supplement to SNTHERM model. *Proceedings of the 2006 International Snow Science Workshop, Telluride, CO, October 1-6, 2006*, 117-126.

Anderson, E.A. (1976). A point energy balance model of a snow cover. *NOAA Technical Report NWS 19*. Office of Hydrology, National Weather Service. (Not seen; cited in Plüss, 1997.)

Andreas, E.L. (1986). A new method of measuring the snow-surface temperature. *Cold Regions Science and Technology*, 12, 139-156.

Bader, H.-P., and Weilenmann, P. (1992). Modeling temperature distribution, energy and mass flow in a (phase-changing) snowpack. I. Model and case studies. *Cold Regions Science and Technology*, 20, 157-181.

Baker, D.G., Ruschy, D.L., and Wall, B.B. (1990). The albedo decay of prairie snows. *Journal of Applied Meteorology*, 29, 179-187.

Balsa Sales Ltd. (2003). *End Grain Balsa Wood and Balsa Core - Balsa Technical Information*. Retrieved 9 July 2006, from Balsa Sales Ltd. web site: http://www.balsasales.co.uk/technical_info.html

Bartelt, P., and Lehning, M. (2002). A physical SNOWPACK model for the Swiss avalanche warning. Part I: Numerical model. C*old Regions Science and Technology*, 35, 123-145.

Bennett, T.J. (1982). A coupled atmosphere-sea ice model study of the role of sea ice in climatic predictability. *Journal of the Atmospheric Sciences*, 39, 1456-1465.

Berliand, T.C. (1960). Method of climatological estimation of global radiation. *Meteorologiya i Gidrologiya*, 6, 9-12. (Not seen; cited in Niemelä et al., 2001a.)

Birkeland, K.W. (1998). Terminology and predominant processes associated with the formation of weak layers of near-surface faceted crystals in the mountain snowpack. *Arctic and Alpine Research*, 30 (2), 193-199.

Birkeland, K.W., Johnson, R.F., and Schmidt, D.S. (1998). Near-surface faceted crystals formed by diurnal Recrystallization: A case study of weak layer formation in the mountain Snowpack and its contribution to snow avalanches. *Arctic and Alpine Research*, 30 (2), 200-204.

Bohren, C.R. and Barkstrom, B.R. (1974). Theory of the optical properties of snow. *Journal of Geophysical Research*, 79 (30), 4527-4535.

Brandt, R.E., and Warren, S.G. (1993). Solar-heating rates and temperature profiles in Antarctic snow and ice. *Journal of Glaciology*, 39 (131), 99-110.

Brock, B.W., and Arnold, N.S. (2000). A spreadsheet-based (Microsoft Excel) point surface energy balance model for glacier and snow melt studies. *Earth Surface Processes and Landforms*, 25, 649-658.

Brun, E., David, P., Sudul, M., and Brunot, G. (1992). A numerical model to simulate snow-cover stratigraphy for operational avalanche forecasting. *Journal of Glaciology*, 38 (128), 13-22.

Buck, A.L. (1981). New equation for computing water vapour pressure and enhancement factor. *Journal of Applied Meteorology*, 20, 1527-1532. (Not seen; cited in Dürr and Philipona, 2004.)

Canadian Avalanche Association (CAA). (2002). *Observation Guidelines and Recording Standards for Weather, Snowpack and Avalanches*. Revelstoke, British Columbia: Canadian Avalanche Association.

Canadian Avalanche Association (CAA). (2003). *Trends and Patterns in Avalanche Aaccidents*. Retrieved 21 November 2004, from Canadian Avalanche Association web site: http://www.avalanche.ca/accident/index.html

Colbeck, S. (1991). The layered character of snow covers. *Reviews of Geophysics*, 29 (1), 81-96.

Colbeck, S., Akitaya, E., Armstrong, R., Gubler, H., Lafeuille, J., Lied, K., McClung, D., and Morris, E. (1990). *The International Classification for Seasonal Snow on the Ground.* Issued by The International Commission on Snow and Ice of the International Association of Scientific Hydrology and Co-Issued by the International Glaciological Society.

Cooperstein, M.S., Birkeland, K.W., and Hansen, K.J. (2004). The effects of slope aspect on the formation of surface hoar and diurnally recrystalized near-surface faceted crystals: Implications for avalanche forecasting. *Proceedings of the 2004 International Snow Science Workshop, Jackson Hole Wyoming*, 83-93.

Deems, J.S., Birkeland, K.W., and Hansen, K.J. (2002). Topographic influence on the spatial patterns of snow temperature gradients in a mountain snowpack. *Proceedings of the International Snow Science Workshop, Penticton, BC, Canada, 29 September-4 October 2002*.

Dilley, A.C., and O'Brien, D.M. (1998). Estimating downward clear sky long-wave irradiance at the surface from screen temperature and precipitable water. *Quarterly Journal of the Royal Meteorological Society*, 124, 1391-1401. (Not seen; cited in Niemelä et al., 2001b.)

Dow Chemical Company (2002). *ETHAFOAM 220 - Technical Data Sheet*. Retrieved 15 September 2006, from The Dow Chemical Company web site: http://www.dow.com/perfoam/market/products/

Durand, Y., Giraud, G., Brun, E., Merindol, L., and Martin, E. (1999). A computer-based system simulating snowpack structures as a tool for regional avalanche forecasting. *Journal of Glaciology*, 44 (151), 469-484.

Dürr, B., and Philipona, R. (2004). Automatic cloud amount detection by surface longwave downward radiation measurements. *Journal of Geophysical Research*, 109, D05201, 1-9.

Etchevers, P., Martin, E., Brown, R., Fierz, C., Lejeune, Y., Bazile, E., Boone, A., Dai, Y., Essery, R., Fernandez, A., Gusev, Y., Jordan, R., Koren, V., Kowalczyk, E., Nasonova, N.O., Pyles, R.D., Schlosser, A., Shmakin, A.B., Smirnova, T.G., Strasser, U., Verseghy, D., Yamazaki, T., & Yang, Z. (2004). Validation of the energy budget of an alpine snowpack simulated by several snow models (SnowMIP project). *Annals of Glaciology*, 38, 150-158.

Fierz, C., Riber, P., Adams, E.E., Curran, A.R., Föhn, P.M.B., Lehning, M., and Plüss, C. (2003). Evaluation of snow-surface energy balance models in alpine terrain. *Journal of Hydrology*, 282, 76-94.

Geldsetzer, T. and Jamieson, B. (2001a). Estimating dry snow density from grain form and hand hardness. *Proceedings of the International Snow Science Workshop in Big Sky Montana, October 2000*, 121-127.

Geldsetzer, T. and Jamieson, B. (2001b). Preliminary testing of the CROCUS snow cover model at Mount Fidelity. ASARC internal report, Department of Civil Engineering, University of Calgary, Calgary, Canada.

Giesbrecht, M.A. and Woo, M. (2000). Simulation of snowmelt in a subarctic spruce woodland: 2. Open woodland model. *Water Resources Research*, 36 (8), 2287-2295.

Glendinning, J.H.G., and Morris, E.M. (1999). Incorporation of spectral and directional radiative transfer in a snow model. *Hydrological Processes*, 13, 1761-1772.

Hägeli, P., and McClung, D. (2003). Avalanche characteristics of a transitional snow climate - Columbia Mountains, British Columbia, Canada. *Cold Regions Science and Technology*, 31, 255-276.

Henneman, H.E., and Stefan, H.G. (1999). Albedo models for snow and ice on a freshwater lake. *Cold Regions Science and Technology,* 29, 31-48.

Hirashima, H., Nishimura, K., Baba, E., Hachikubo, A., and Lehning, M. (2004). SNOWPACK model simulations for snow in Hokkaido, Japan. *Annals of Glaciology*, 38, 123-129.

Iziomon, M.G, Mayer, H., and Matzarakis, A. (2003). Downward atmospheric longwave irradiance under clear and cloudy skies: Measurement and parameterization. *Journal of Atmospheric and Solar-Terrestrial Physics*, 65, 1107-1116.

Jacobs, J.D. (1978). Radiation climate of Broughton Island. Energy budget studies in relation to fast-ice breakup processes in Davis Strait. *Occasional Paper 26, Institute of Arctic and Alpine Research, University of Colorado, Boulder, Colorado, USA*, 105-120. (Not seen; cited in Niemelä et al., 2001b.)

Jamieson, B., and Stethem, C. (2002). Snow avalanche hazards and management in Canada: Challenges and progress. *Natural Hazards*, 26, 35-53.

Jamieson, B., Campbell, C., and Jones, A. (2006). Spatial and time scale effects in Canadian avalanche bulletins. *Proceedings of the 2006 International Snow Science Workshop, Telluride, CO, October 1-6, 2006*, 394-402.

Jordan, R. (1991). A one-dimensional temperature model for a snow cover - Technical documentation for SNTHERM.89. *CRREL Special Report, 91-16*.

Koivusalo, H., and Heikinheimo, M. (1999). Surface energy exchange over a boreal snowpack: comparison of two snow energy balance models. *Hydrological Processes*, 13, 2395-2408.

Koivusalo, H., and Kokkonen, T. (2002). Snow processes in a forest clearing and in a coniferous forest. *Journal of Hydrology*, 262, 145-164.

Kondo, J., and Yamazaki, T. (1990). A prediction model for snowmelt, snow surface temperature and freezing depth using a heat balance model. *Journal of Applied Meteorology*, 29, 375-384.

Konzelmann, T., van der Wal, R.S.W., Greuell, W., Bintanja, R., Henneken, E.A.C., and Abe-Ouchi, A. (1994). Parameterization of global and longwave incoming radiation for the Greenland ice sheet. *Global and Planetary Change*, 9, 143-164.

Laevastu, T. (1960). Factors affecting the temperature of the surface layer of the sea. *Commentationes Physico-Mathematicae*, 25. (Not seen; cited in Niemelä et al., 2001a.)

Lehning, M., Bartelt, P., Brown, B., and Fierz, C. (2002a). A physical SNOWPACK model for the Swiss avalanche warning. Part III: Meteorological forcing, thin layer formation and evaluation. *Cold Regions Science and Technology*, 35, 169-184.

Lehning, M., Bartelt, P., Brown, B., Fierz, C., and Satyawali, P. (2002b). A physical SNOWPACK model for the Swiss avalanche warning. Part II. Snow microstructure. *Cold Regions Science and Technology*, 35, 147-167.

Lehning, M., Bartelt, P., Bethke, S., Fierz, C., Gustafsson, D., Landl, B., Lütschg, M., Martius, O., Meirold-Mautner, I., Raderschall, N., Rhyner, J., and Stähli, M. (2004). Review of SNOWPACK and ALPINE3D applications. *Proceedings, Snow Engineering 2004 Davos*, 299-307.

Lilliefors, H.W. (1967). On the Kolmogorov-Smirnov test for normality with mean and variance unknown. *Journal of the American Statistical Association*, 62 (318), 399-402.

Link, T.E., Marks, D. and Hardy, J.P. (2004). A deterministic method to characterize canopy radiative transfer properties. *Hydrological Processes*, 18, 3583-3594.

Lundy, C.C., Brown, R.L., Adams, E.E., Birkeland, K.W., and Lehning, M. (2001). A statistical validation of the SNOWPACK model in a Montana climate. *Cold Regions Science and Technology,* 33, 237-246.

Male, D.H., and Granger, R.J. (1981). Snow surface energy exchange. *Water Resources Research*, 17 (3), 609-627.

Male, D.H., and Gray, D.H. (1981). In Gray, D.M., and Male, D.H. *Handbook of Snow*. Toronto, Ontario: Pergamon Press.

Marks, D., Domingo, J., Susong, D., Link, T., and Garen, D. (1999). A spatially distributed energy balance snowmelt model for application in mountain basins. *Hydrological Processes*, 13, 1935-1959.

McClung, D.M. (1996). Effects of temperature on fracture in dry slab avalanche release. *Journal of Geophysical Research*, 101 (B10), 21907-21920.

McClung, D., and Schaerer, P. (1993). *The Avalanche Handbook.* Seattle, WA: The Mountaineers.

McClung, D.M., and Schweizer, J. (1997). Effect of snow temperature on skier triggering of dry snow slab avalanches. *Proceedings of the International Snow Science Workshop, Banff, Alberta, Canada, 6-10 October 1996*, 113-117.

Meirold-Mautner, I. (2004). A physical snow-radiation model: Measurements, model development and applications to the snow ecosystem. PhD thesis, Department of Meteorology and Geophysics, University of Innsbruck, Innsbruck, Austria.

Mellor, M. (1977). Engineering properties of snow. *Journal of Glaciology*, 19 (81), 15-66.

Moritz, R.E. (1978). A model for estimating global solar radiation. Energy budget studies in relation to fast-ice breakup processes in Davis Strait. *Occasional Paper 26, Institute of Arctic and Alpine Research, University of Colorado, Boulder, Colorado, USA*, 121-142. (Not seen; cited in Niemelä et al., 2001a.)

Morstad, B.W. (2004). Analytical and experimental study of radiation-recrystallized near-surface facets in snow. MSc thesis, Department of Mechanical Engineering, Montana State University, Bozeman, Montana, USA.

Niemelä, S., Räisänen, P., and Savijärvi, H. (2001a). Comparison of surface radiative flux parameterizations Part II. Shortwave radiation. *Atmospheric Research*, 58, 141-154.

Niemelä, S., Räisänen, P., and Savijärvi, H. (2001b). Comparison of surface radiative flux parameterizations. Part I: Longwave radiation. *Atmospheric Research*, 58, 1-18.

Obled, C., and Harder, H. (1978). A review of snow melt in the mountain environment. *Proceedings, Modeling of Snow Cover Runoff* (S.C. Colbeck and M. Ray, editors). Hanover, New Hampshire: U.S. Army Cold Regions Research and Engineering Laboratory, 179-204.

Ohmura, A. (2000). Physical basis for the temperature-based melt-index method. *Journal of Applied Meteorology*, 40, 753-761.

Omega Engineering Inc. (2004). *ANSI and IEC Color Codes for Thermocouples, Wire and Connectors*. Retrieved 9 July 2006, from Omega Engineering Inc. web site: http://www.omega.com/techref/colorcodes.html

Paltridge, G.W., and Platt, C.M.R. (1976). *Radiative Processes in Meteorology and Climatology*. Amsterdam: Elsevier. (Not seen; cited in Niemelä et al., 2001a.)

Plüss, C. (1997). The energy balance over an alpine snowcover: point measurements and areal distribution. *Zurcher Geographische Schriften*, 65, Verlag Geographisches Institut ETH, Zurich, Switzerland.

Plüss, C., and Mazzoni, R. (1994). The role of turbulent heat fluxes in the energy balance of high alpine snow cover. *Nordic Hydrology*, 25, 25-38.

Plüss, C., and Ohmura, A. (1996). Longwave radiation on snow-covered mountainous surfaces. *Journal of Applied Meteorology*, 36, 818-824.

Prata. A.J. (1996). A new long-wave formula for estimating downward clear-sky radiation at the surface. *Quarterly Journal of the Royal Meteorological Society*, 122, 1127-1151. (Not seen; cited in Niemelä et al., 2001b.)

Robinson, N. (1966). *Solar radiation*. New York, NY: American Elsevier Publishing Company.

Rowlands, A., Pomeroy, J., Hardy, J., Marks, D., Elder, K., and Melloh, R. (2002). Small-scale spatial variability of radiant energy for snowmelt in a mid-latitude sub-alpine forest. *59th Eastern Snow Conference, Stowe, Vermont, USA 2002*, 109-117.

Schweizer, J., Jamieson, J.B., and Schneebeli, M. (2003). Snow avalanche formation. *Reviews of Geophysics*, 41 (4), 2_1-2_25.

Sicart, J.E., Pomeroy, J., Essery, R., and Hardy, J. (2003). Snowmelt in a Canadian spruce forest: A sensitivity study to the canopy cover. *60th Eastern Snow Conference, Sherbrooke, Quebec, Canada 2003*, 99-110.

Spreitzhofer, G., Fierz, C., and Lehning, M. (2004). SN_GUI: a graphical user interface for snowpack modeling. *Computers & Geosciences*, 20, 809-816.

Spreitzhofer, G., Fierz, C., Lehning, M., and Schirmer, M. (2006). *Snowpack_Win User Manual, Version 26 July 2006*. Davos-Dorf, Switzerland: WSL Snow and Avalanche Research SLF.

Staples, J.M., Adams, E.E., Slaughter, A.E., and McKittrick, L.R. (2006). Slope scale modelling of snow surface temperature in topographically complex terrain. *Proceedings of the 2006 International Snow Science Workshop, Telluride, CO, October 1-5, 2006*, 806-814.

StatSoft, Inc. (2006). Electronic Statistics Textbook. Tulsa, OK: StatSoft.

Sturm, M., Holmgren, J., and Liston, G.E. (1995). A seasonal snow cover classification system for local to global applications. *Journal of Climate*, 8, 1261-1283.

Sturm, M., Holmgren, J., König, M., and Morris, K. (1997). The thermal conductivity of seasonal snow. *Journal of Glaciology*, 43 (143), 26-41.

Tabachnick, B.G. and Fidell, L.S. (2001). *Using Multivariate Statistics*. Toronto, ON: Allyn and Bacon.

U.S. National Oceanic and Atmospheric Administration Surface Radiation Research Branch. (n.d.). *Sunrise/Sunset Calculations*. Retrieved 12 June 2006, from U.S. National Oceanic and Atmospheric Administration Surface Radiation Research web site: http://www.srrb.noaa.gov/highlights/sunrise/solareqns.PDF

Walraven, R. (1978). Calculating the position of the sun. *Solar Energy*, 20, 393-397.

Warren, S.G. (1982). Optical properties of snow. *Reviews of Geophysics and Space Physics*, 20, 1, 67-89.

Wiscome, W.J., and Warren, S.G. (1980). A model for the spectral albedo of snow. I: Pure snow. *Journal of the Atmospheric Sciences*, 37, 2712-2733.

Woo, M., and Giesbrecht, M.A. (2000). Simulation of snowmelt in a subarctic spruce woodland: 1. Tree model. *Water Resources Research*, 36 (8), 2275-2286.

APPENDIX A: MEASUREMENT ERRORS

Field data collected for this study were subject to both errors in temperature measurement and errors in accurately determining thermocouple depths. The following sections outline estimates for the magnitude of both measurement error components.

A.1 Temperature measurement errors

As discussed in Section 2.1, it is difficult to eliminate temperature measurement errors that result from excess absorption of short wave radiation by the measurement equipment itself. Field data collected for this study included measured snowpack temperature values greater than 0 ºC, which is not physically possible at ambient pressure. From the point at which liquid water becomes present until the point at which all ice has completely melted, the snowpack temperature will remain at 0 ºC. Despite steps taken to match the properties of the measurement equipment to the snow, differences in the absorption and emission characteristics of the equipment resulted in temperature measurement errors.

As shown in Figure A.1(a), the percentage of temperature measurements greater than 0 ºC, over all of the field experiments, decreased with depth below the snow surface. When the temperature data for each field experiment are examined individually, however, the percentage of above-zero temperatures actually increased with depth in the field experiments beginning on 25 April 2005 and 21 April 2006 (Figure A.1(b)). In these cases, night-time cooling was insufficient to overcome the daytime temperature increases at depth. The temperatures closest to the surface cooled below 0 ºC overnight due to outgoing long wave radiation, but the cooling did not reach far below the surface

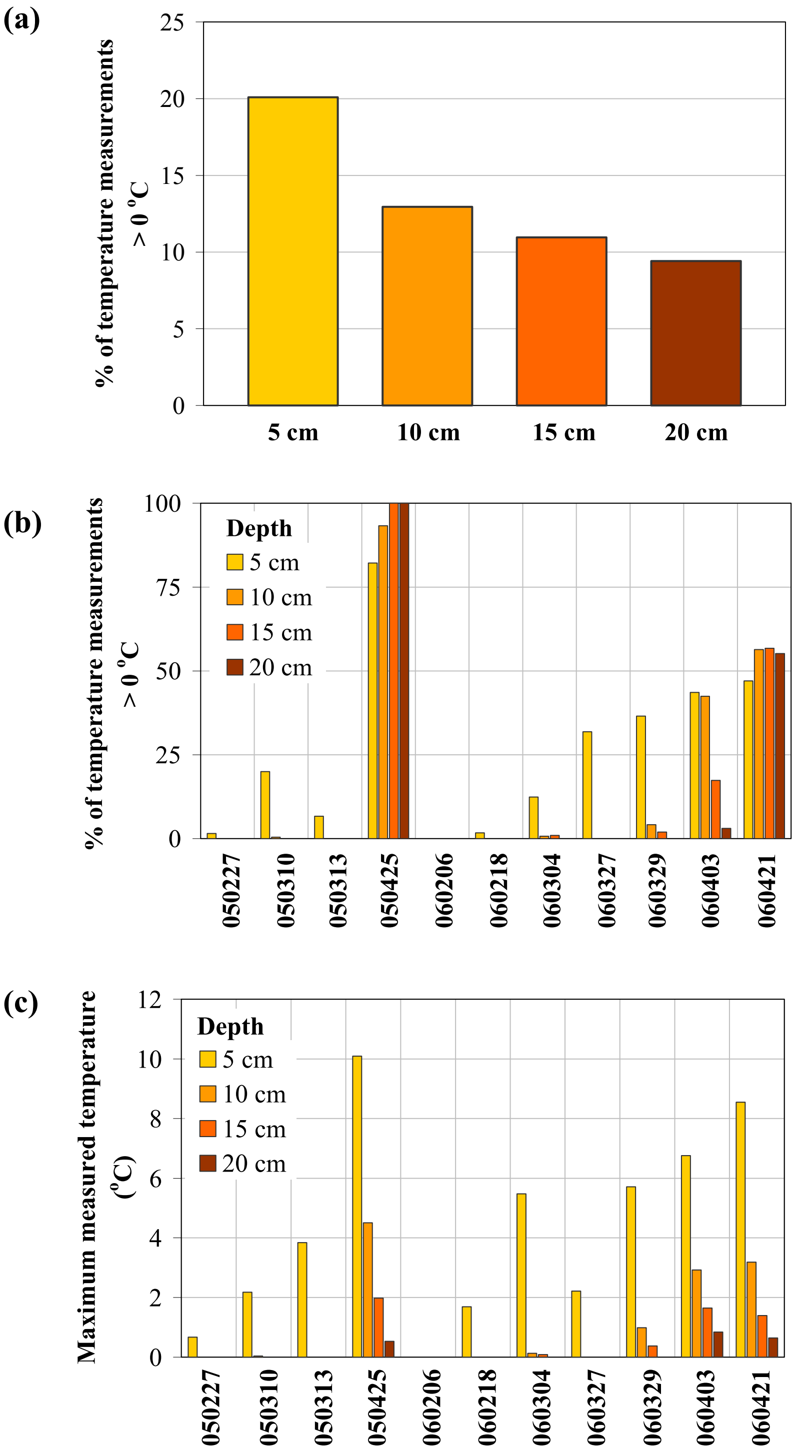

Figure A.1: *Summary of above-zero temperatures measured during the 2005 and 2006 field experiments: (a) percentage of total temperature measurements greater than 0 ºC, (b) percentage of temperature measurements greater than 0 ºC for each field experiment, and (c) maximum measured temperature for each field experiment.*

(in some cases to depths of only approximately 6 cm) and deeper measurements remained just above 0 ºC. The maximum measurement errors, assuming a corresponding snowpack temperature of 0 ºC, were 10.0 ºC at 5 cm depth, 4.5 ºC at 10 cm depth, 2.0 ºC at 15 cm depth, and 0.8 ºC at 20 cm depth (Figure A.1(c)). Given the decrease in short wave radiation flux with depth below the snow surface, the decreasing magnitude of measurement errors with depth is expected. Both the magnitude of the temperature measurement errors and the percentage of above-zero measurements showed an increasing trend as the winter season progressed.

A.1.1 Measurements in a melting snowpack

Many of the highest temperatures were measured during the field experiment starting on 25 April 2005. Field observations and manual snow temperature measurements confirmed that the top 30 cm of the snowpack was isothermal and melting throughout this measurement period. A known field temperature (0 ºC) allows for evaluation of the magnitude of the temperature measurement errors, which should be proportional to the magnitude of short wave radiation reaching the measurement point. Unfortunately, measurements of incoming short and long wave radiation are not available for this time period, as the radiometers had been removed for calibration. In order to complete this analysis, estimates for the magnitude of incoming short wave radiation were calculated based on the methods described in Section B.1.1.

Manual snow profiles completed on 25 April 2005 identified surface crystals as wet grain clusters at all four array sites, with a typical diameter of 5-10 mm. Male and Gray (1981) quote 0.61 as a typical albedo value for wet, clean, granular snow.

Extinction coefficient parameterizations based on snow density alone would indicate high values for the dense, wet snow observed at all array locations during this field experiment. However, Mellor, (1977) noted that the extinction coefficient also decreases with increasing grain size. The presence of water in the snowpack will act to increase the effective grain size (Wiscome and Warren, 1980), contributing to a decrease in extinction coefficient. Mellor (1977) provided a plot of extinction coefficient for different snow types which indicated an extinction coefficient of approximately 18 m^{-1} for wet coarse grained snow with a mean grain size of 1.0 mm. This value, which does not vary much within the wavelength range shown (0.4-0.7 µm), should be conservatively high for the large diameter grains observed in the field.

After projecting the hourly incoming short wave radiation estimates for the 25-26 April 2005 field experiment onto each array slope (Robinson, 1966, Chapter 2), the short wave radiation flux reaching 5, 10, 15, 20 and 25 cm depth at each array location was calculated using the above-noted estimates and Equation A.1.

$$SW_d = SW_s \cdot (1 - \alpha) \cdot \exp(-\beta \cdot d) \qquad \text{(A.1)}$$

where SW_d = short wave radiation at depth d (W/m^2)
SW_s = short wave radiation incident on the snow surface (W/m^2)
α = albedo (assumed to be 0.61)
β = short wave radiation extinction coefficient (assumed to be 18 m^{-1})
d = depth below snow surface (m)

Given field observations of an isothermal near-surface snowpack, the temperatures measured during the 25-26 April 2005 field experiment represent the magnitude of the measurement error. A significant coefficient of determination (r^2 = 0.65, $p < 0.001$) was found between the short wave radiation flux estimates and the magnitude of corresponding temperature measurement errors. The dataset used in this analysis included all positive hourly temperature measurements (at 5, 10, 15, 20 and 25 cm depths) with a corresponding positive short wave radiation flux estimate (n = 289). A linear regression resulted in the following equation relating the magnitude of the temperature measurement error (T_{err}) to the short wave radiation flux at the measurement point.

$$T_{\mathrm{err}} = 0.0245 \cdot \mathrm{SW_d} \tag{A.2}$$

A significant intercept was not identified in the linear regression analysis, which had a standard error of estimate (SEE) of 0.69 ºC. Data points used to develop the linear regression equation are plotted in Figure A.2.

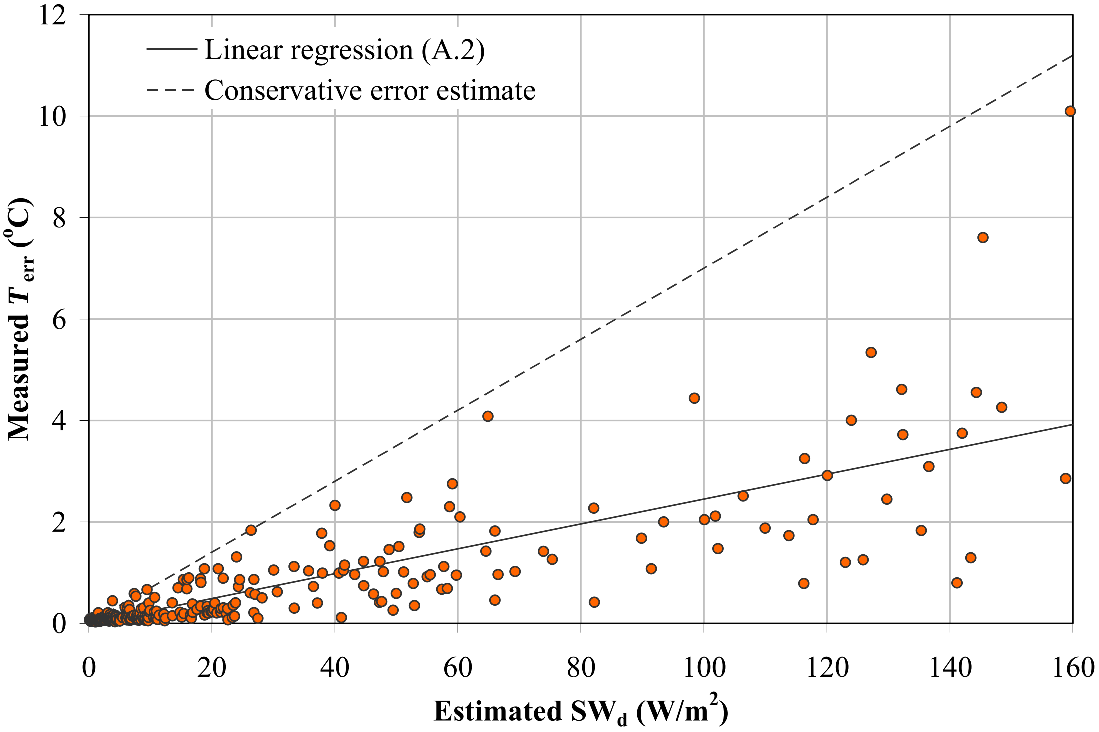

Figure A.2: *Temperature measurement error plotted against estimated short wave radiation flux. The linear regression (solid line) has an r^2 value of 0.65 (n = 289). The dashed line represents a conservative estimate of temperature measurement errors, which encompasses most of data points included in the linear regression analysis.*

The linear regression equation does not fully account for variation in the measured temperature errors, and it is apparent that the residuals increase with increasing values of the independent variable (heteroscedasticity). The regression equation, however, does provide a means of estimating the magnitude of temperature measurement errors. Note that the calculated short wave radiation flux is based on approximate values for incoming short wave radiation at the snow surface, albedo and extinction coefficient. Sources of error include variation in cloud opacity, differences in snow properties over terrain, changing snowpack characteristics with depth and limited availability of wet snow extinction coefficient data to verify the assumed value.

Wet grains, such as those present on 25-26 April 2005, are associated with values of albedo and extinction coefficient lower than those for dry snow. A reduction in the amount of short wave radiation reflected at the snow surface and less attenuation within the snowpack both correspond to more short wave radiation within the near-surface layers. The magnitude of short wave radiation reaching the thermocouple tips, and therefore the magnitude of the associated measurement error, should be at a maximum under these spring snow conditions.

To illustrate expected variation in temperature measurement errors under different snow conditions, short wave radiation flux values, assuming a high value of incoming short wave radiation (1000 W/m^2), were calculated at 5 and 10 cm depth for two hypothetical surface snowpack layers. The linear regression equation (A.2) was then used to estimate temperature measurement errors at these depths (Table A.1). Case 1 reflects the wet snow albedo and extinction coefficient estimates outlined above. An empirical equation developed by Baker et al. (1990) was used to calculate albedo for the hypothetical snow cases (Section B.2.1). The extinction coefficient was estimated using the equation presented in Section B.2.2 with the constant values obtained from Meirold-Mautner (2004). Snow density for cases 2 and 3 was determined from the hypothetical grain type and hand hardness using the empirical method developed by Geldsetzer and Jamieson (2001a).

Table A.1: *Comparison of estimated temperature measurement errors for different hypothetical near-surface snow characteristics.*

Case	**Description**	**SW_s (W/m^2)**	**α**	**β (m^{-1})**	***d* (cm)**	**SW_d (W/m^2)**	**estimated T_{err} (°C)**
1	wet grains	1000	0.61	18.0	5	126.8	3.9
					10	51.6	1.6
2	precipitation particles, F hardness, 0 days since new snow	1000	0.84	38.1	5	19.2	0.6
					10	2.8	0.1
3	decomposing fragments, 4F hardness, 5 days since new snow	1000	0.73	43.7	5	24.0	0.7
					10	2.7	0.1

Figure A.2 includes a second, more conservative, temperature measurement error estimate that encompasses most of the data points used in the linear regression analysis. Using the equation for the conservative line, the estimated temperature errors for cases 2 and 3 remain less than 0.25 ºC at 10 cm depth. The above calculations illustrate that the magnitude of temperature measurement errors under non-melt conditions are minimal at and below a depth of 10 cm.

A.1.2 Shading experiments

In a separate attempt to quantify the magnitude of temperature measurement errors, arrays were briefly shaded from direct short wave radiation during some of the 2006 field experiments (Figure A.3). These shading experiments were undertaken on different days throughout the season, at different times during the day, on different aspects and slope angles, with different snow conditions and under different weather conditions. The intent was to measure an initial rapid decrease in temperature due to elimination of excess absorption of short wave radiation, similar to the results reported by Brandt and Warren (1993) and Morstad (2004).

After setting the datalogger to measure and record temperature values once every minute, an array would be shaded from above for 15 seconds (10 seconds preceding and 5 seconds following a measurement). Figure A.4 illustrates the shading data collected during 2006, which included 93 shading periods completed under a variety of different conditions. Using temperature values interpolated at 5, 10, 15, 20 and 25 cm below the

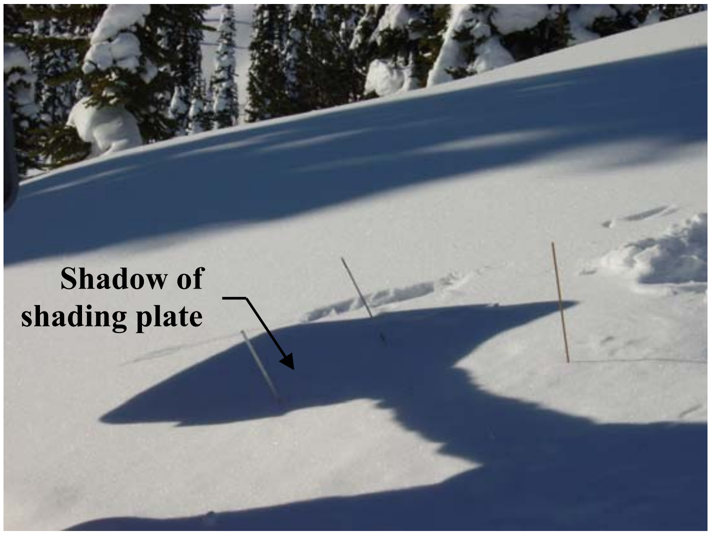

Figure A.3: *Shading of array from direct short wave radiation (photo: ASARC).*

snow surface, the temperature decrease due to shading was calculated by subtracting the shaded temperature from the average of the (unshaded) temperatures measured one minute before and one minute after. Five such consecutive 'shading' values were recorded at each array site during each experiment. The data plotted in Figure A.4 are the averages for each set of five values. Only three measurements, at 5 cm depth, showed an increase in temperature with shading. These points, which may be the result of errors in timing and recording, were excluded. The measured temperature decrease after shading was typically small and decreased with depth (Table A.2).

Table A.2: *Summary of temperature decrease measured after shading from direct short wave radiation for 10 s.*

Depth (cm)	**n**	**'Shaded' temperature decrease (ºC)**	
		Maximum	***Maximum***
5	90	1.1	1.1
10	93	0.3	0.3
15	93	0.2	0.2
20	93	0.2	0.2
25	93	0.1	0.1

Consideration of the length of time for which the array was shaded is important in assessing the results of these shading experiments. As noted in Section 2.1, Brandt and Warren (1993) observed initial rapid cooling after shading their equipment from direct short wave radiation, which they attributed to elimination of the excess short wave radiation absorbed by the measurement equipment. Subsequent gradual temperature decrease was thought to reflect cooling of the snowpack itself. A plot of their data shows the duration of the rapid cooling to be approximately 1 minute, but no mention of the measurement time interval is made. Morstad (2004) used temperature readings recorded immediately after turning off the solar lamp in an experimental chamber to quantify

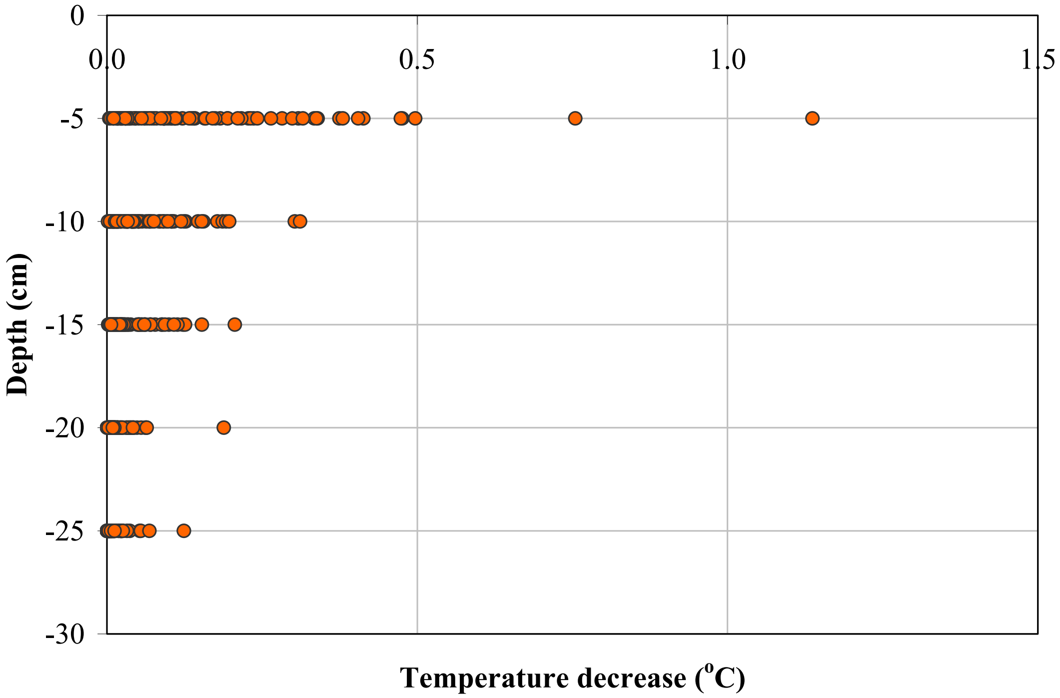

Figure A.4: *Temperature decrease measured after shading arrays from direct short wave radiation for 10 s. Data include measurements at different times through the season, different times during the day, different aspects and slope angles, different snow conditions and different weather conditions (approximately 93 measurements at each depth).*

measurement errors. As temperature data were recorded every 30 seconds during his experiments, it is assumed that the noted temperature decrease occurred within this length of time.

Because the thermocouples have low thermal mass, and therefore respond quickly to temperature changes, removal of the short wave radiation source should have an immediate effect. For this reason, and to reduce the likelihood of disturbing the surface energy balance while shading, a short shading period was thought to be appropriate. Attempts were made to decrease the datalogger storage interval below one minute for the field shading experiments, to try and capture the point at which the temperature decrease changes from rapid to gradual, but these were unsuccessful due to datalogger and programming limitations. Several experiments were undertaken in which field staff varied the length of the shading period, but the results were inconclusive. Some show no noticeable change in the measured temperature decrease with a longer shading period, while others show larger temperature decreases as the shading period lengthens. It is possible that shading periods of 10 seconds were too short to fully capture the 'measurement error' rapid temperature decrease, but this cannot be confirmed without higher frequency measurements during the shading experiments. The magnitude of the temperature measurement errors at 10 cm depth estimated from the shading data is, however, comparable with the measurement error estimates calculated in the previous section.

A.2 Depth measurement errors

Because near-surface temperatures vary substantially with depth, an accurate determination of the thermocouple depths throughout each field experiment is important for interpretation of the temperature measurements. The same person placed all of the thermocouples for all experiments and, although great care was taken during placement, it was difficult to ensure that they were inserted completely parallel to the snow surface. The slope normal depth of each thermocouple tip was measured upon completion of each experiment, but initial and interim measurements could not be made without disturbing the surrounding snow.

To keep the measurements close to the snow surface and to reduce difficulties in tracking thermocouple depths, the temperature measurement equipment was only set up during periods without forecast precipitation. Temperature data was collected on all or part of 32 different days during the winters of 2005 and 2006; new snow occurred on seven of these days. Field measurements made on the top of Gopher Butte knoll indicate approximately 8 cm of new snow on 21 April 2006, which settled rapidly (to approximately 4 cm) the following day. Manual observations and precipitation data from the Mount Fidelity study plot indicate that approximately 5 cm of new snow fell on 6 February 2006. The remaining experiment days with snowfall, less than 3 cm in all cases, prompted the end of a temperature measurement period. Measurements collected on these days were insufficient to define the magnitude of daytime warming and, as such, they were not included in the dataset used to develop the warming model.

Settlement of light near-surface snow layers also added to the difficulty of determining depth changes throughout each field experiment. Although the low density of balsa wood was a prime reason for its choice as material for the thermocouple holders, the balsa wood sections were observed to settle at different rates than the surrounding snow. The magnitude of this effect varied depending on factors like the density and temperature of the near-surface snow.

During the winter of 2005, the design of the balsa wood holders was such that they moved independently of each other within the snowpack. Because each thermocouple settled at a different rate, this arrangement made it difficult to track the depths. Despite the use of a guiding template and having a second field person 'eyeball' each holder to ensure it was placed parallel to the snow surface, substantial variation between the intended and actual (measured at the finish of each experiment) tip depth occurred (± 3 cm). Melting of the snow around the upper thermocouples was also noted during some experiments, adding to the difficulty of determining the initial depth of each thermocouple. With the exception of the last experiment (25-26 April 2005), in which substantial melting around the top thermocouples was observed, depths throughout each experiment were assumed to be as measured at completion. Position errors were judged to be less than 3 cm for most measurements. For the April 25-26 experiment, depth changes as a result of melting were estimated from photographs taken of each array site at hourly intervals during the daytime.

To alleviate some measurement difficulties, Ethafoam guiding blocks were added in the winter of 2006 (Section 3.2.2). Two blocks, each holding five thermocouples, were backfilled in place at each array site. The backfilled snow around the blocks was observed not to settle relative to the settlement of the undisturbed snow at the tip of the thermocouples. The blocks established a single position error for each group of five thermocouples instead of individual errors for each thermocouple, as with the 2005 equipment. For each group of five thermocouples, the blocks also kept the depth changes consistent throughout each experiment.

A variety of information was used to estimate depth changes. Field staff took frequent photographs of each array site during most field experiments, recording the time at which each photograph was taken. Where settlement or melting occurred such that the top thermocouple(s) became visible, the location of the top thermocouple relative to the snow surface could be estimated. With the 2006 equipment setup, it was assumed that all thermocouples held by a foam block (five) moved together and that the relative difference in depth between thermocouples remained consistent throughout the entire experiment. In calculating depths, it was also assumed that the top thermocouple began each experiment at the intended placement depth of 2 cm, unless specific notes about higher or lower initial placement were made. Overall depth changes noted between photographs were linearly interpolated over the intervening time in 15 minute intervals.

As the field season progressed, field staff collected additional information to improve determination of depths. An avalanche probe placed on top of the knoll for the duration of each field experiment was used to measure changes in overall snow depth due to precipitation and settlement. Where photographs showing the top thermocouple were not available, thermocouple depths were adjusted using this information. The vertical increase in depth (due to new snow) and vertical decrease in depth (due to settlement) were assumed to be the same at all the array locations.

Hourly precipitation data from the Fidelity research station were used to identify the timing and magnitude of new snow depth for periods in which neither appropriate photographs nor field observations were available. As noted previously, 6 February 2006 and 21 April 2006 were the only two days included in the daytime warming dataset on which snowfall occurred. With assumed initial (2 cm) and known final (as measured at experiment completion) depths and new snow estimates, an approximate settlement rate was calculated and applied throughout each experiment.

To assess the depth estimates and resultant effects on temperature measurement accuracy, a comparison was done using the data collected from 6-12 February 2006. This field experiment, the first of the 2006 season, was completed before field staff began recording settlement measurements to assist with depth estimation. Considering this, the length of this experiment, the occurrence of light precipitation and observed settlement in the field, it was expected to be a field experiment in which depth estimation errors would be relatively high. Table A.3 summarizes a comparison between temperatures interpolated from the field data using two different methods of estimating depth. The difference shown reflects the difference in temperature interpolated using the 'best-estimate' depths (determined as outlined above) and those interpolated using an assumed constant depth throughout the experiment (equal to that measured at completion).

Table A.3: *Comparison of temperature values for the 6-12 February 2006 field experiment interpolated (15 minute interval) with two different methods of determining depth. 'Best-estimate' depths were estimated as outlined in the preceding paragraphs, while constant depths assume the depth measured upon completion of the field experiment throughout.*

Depth (cm)	**Temperature difference (ºC) |'best-estimate' depth temperature - constant depth temperature|**		
	Maximum	***Mean***	***Standard deviation***
5	5.6	0.7	0.9
10	3.5	0.5	0.6
15	2.1	0.4	0.4
20	2.7	0.3	0.3
25	1.0	0.3	0.3

Under difficult depth determination conditions, depth discrepancies were estimated to be less than 5 cm (maximum difference = 4.7 cm, mean difference = 1.9 cm). These result in depth-dependent temperature errors of up to 5.6 ºC at 5 cm depth, decreasing to a maximum of 3.5 ºC at a depth of 10 cm. The observed decrease in temperature error with depth is expected, as temperature gradients are typically higher closer to the snow surface. Note that these errors were calculated by comparing a 'good' depth estimate against an inaccurate depth estimate (i.e. not a comparison of the depth estimate against the actual depth). Given all the information considered in estimating thermocouple depths, the difference between the estimated and actual depths is likely much smaller.

A.3 Summary

Examination of the field measurements indicates that, under dry snow conditions, the magnitude of the temperature measurement errors at 10 cm depth was less than 0.3 ºC. At 5 cm depth, the magnitude increases to approximately 1 ºC. Temperature measurement errors were substantially higher when the upper snowpack layers begin to melt.

Thermocouple depth estimates were prepared using all available information. With 'worst-case' conditions for depth estimation, the majority of depth-dependent temperature errors are expected to be less than 2.5 ºC and 1.7 ºC at depths of 5 and 10 cm, respectively. In reality, the depth-dependent temperature errors are anticipated to be considerably lower.

APPENDIX B: PARAMETER ESTIMATION

B.1 Radiation fluxes

Radiation measurements are not often available to avalanche forecasters. The instruments are relatively expensive, and lack of power and/or personnel necessary to keep radiometers free from snow can limit the applicability of measurements where they are available. In order to keep input data requirements for the warming model simple, estimates that can be calculated from standard observations or easily obtainable information were required. The following sections outline the approach used to estimate each of the radiation fluxes included in development of the warming model.

The short wave radiation estimates were also used in the temperature measurement error assessment outlined in Appendix A.

B.1.1 Incoming short wave radiation

Three simple methods of estimating incoming short wave radiation under clear sky conditions were obtained from a review of short wave radiation parameterizations prepared by Niemelä et al. (2001a). The equations, which require only the solar zenith angle as input, are provided below with reference to the original source.

$$\mathrm{SW}_{\mathrm{clr}} = S_0 \cdot \cos\theta \cdot (0.47 + 0.47 \cdot \cos\theta) \qquad \textit{Moritz, 1978} \qquad \text{(B.1)}$$

$$\mathrm{SW}_{\mathrm{clr}} = 0.72 \cdot S_0 \cdot \cos\theta \qquad \textit{Bennett, 1982} \qquad \text{(B.2)}$$

$$\mathrm{SW}_{\mathrm{clr}} = 10 + 1411 \cdot \cos\theta - 310 \cdot (\cos\theta)^{0.5} \qquad \textit{Paltridge and Platt, 1967} \qquad \text{(B.3)}$$

where $\mathrm{SW}_{\mathrm{clr}}$ = incoming short wave radiation under clear skies (W/m^2)
S_0 = solar constant (1367 W/m^2)
θ = solar zenith angle

The following parameterizations, also found in Niemelä et al. (2001a), were applied to adjust each of the clear sky short wave radiation estimates for cloud cover.

$$\mathrm{SW_{all}} = [(1 - c) + t_c \cdot c] \cdot \mathrm{SW_{clr}} \qquad \textit{Berliand, 1960} \qquad \text{(B.4)}$$

$$\mathrm{SW_{all}} = (1 - 0.6 \cdot c^3) \cdot \mathrm{SW_{clr}} \qquad \textit{Laevastu, 1960} \qquad \text{(B.5)}$$

where $\mathrm{SW_{all}}$ = incoming short wave radiation under all sky conditions ($\mathrm{W/m^2}$)
c = cloudiness (decimal fraction)
t_c = cloud transmissivity (assumed to be 0.48)

The resultant incoming global short wave radiation estimates apply to a horizontal receiving surface.

A dataset consisting of 102 points was compiled by taking all positive incoming short wave radiation measurements from the winters of 2005 and 2006 for which a corresponding manual sky observation was available. Based on the sky condition definitions included in the Canadian Avalanche Association Observation Guidelines and Recording Standards (CAA, 2002, p. 2), cloudiness was estimated from each manual sky observation (Table B.1). To keep the incoming short wave radiation estimates simple, the opacity of the observed cloud cover was not considered.

Table B.1: *Cloudiness estimates for manual sky observations (after CAA, 2002, p. 2).*

Manual sky observation	Data code	Definition	Estimated cloudiness
Clear	CLR	No clouds.	0
Few	FEW	Up to 2/8 of the sky is covered with clouds.	0.125
Scattered	SCT	3/8 to 4/8 of the sky is covered with clouds.	0.375
Broken	BKN	More than half but not all of the sky is covered with clouds.	0.750
Overcast	OVC	The sky is completely covered.	1
Obscured	X	A surfaced based layer or non-cloud layer prevents observer from seeing the sky.	1

For each data point, the solar zenith angle at the appropriate day and time was determined using methods outlined by Walraven (1978). Six estimates of all sky incoming short wave radiation were then calculated, using each of the clear sky parameterizations with both cloud cover adjustments, and compared with the measured hourly average values (Table B.2). The highest coefficient of determination ($r^2 = 0.83$, $p < 0.001$) between incoming short wave radiation measurements and estimated values corresponded to the combination of equations B.1 and B.4 (Figure B.1). These equations were subsequently used when incoming short wave radiation estimates were required.

Table B.2: *Comparison between measured incoming global short wave radiation and values estimated with several different methods.*

Method of estimating incoming short wave (equations)	***n***	**Coefficient of determination (r^2) with measured incoming global short wave radiation**
B.1 and B.4	102	0.83
B.1 and B.5	102	0.78
B.2 and B.4	102	0.77
B.2 and B.5	102	0.72
B.3 and B.4	100	0.82
B.3 and B.5	100	0.76

Field measurements and estimates of incoming global short wave applied to a horizontal receiving surface and, in order to use them with knoll slope temperature measurements, they had to be projected accordingly. The following procedure was utilized:

1. Split the hourly measurements of global incoming short wave radiation into direct and diffuse components. Equations 6.1 and 6.2 follow the approach used by Geldsetzer and Jamieson (2001b).

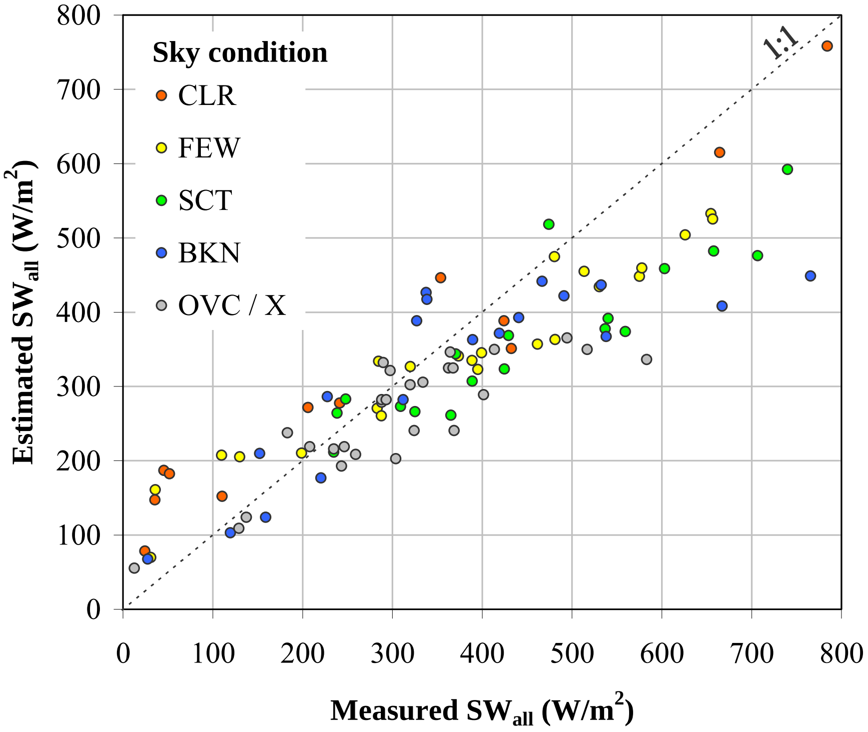

Figure B.1: *Comparison of measured and estimated incoming global short wave radiation. Estimated values were calculated using equations B.1 and B.4. A significant coefficient of determination (r^2 = 0.83, p < 0.001) was found in the dataset (n=102).*

$$SW_{diff} = SW \cdot c + SW \cdot clr \cdot (1 - c) \qquad (B.6)$$

$$SW_{dir} = SW_{all} - SW_{diff} \qquad (B.7)$$

where SW_{diff} = diffuse incoming short wave radiation (W/m^2)
SW_{dir} = direct incoming short wave radiation (W/m^2)
SW_{all} = incoming short wave radiation under all sky conditions (W/m^2)
c = cloudiness (decimal fraction)
clr = contribution of diffuse incoming short wave radiation under clear skies (assumed to be 0.15)

2. Calculate the hourly solar zenith angle and azimuth to determine the direction of direct incoming short wave radiation (Walraven, 1978).

3. Adjust the hourly direct incoming short wave radiation values for the slope and aspect of the receiving slope (Robinson, 1966, Chapter 2)
4. Combine the adjusted direct component with the diffuse component to obtain an hourly measure of global short wave radiation incident on a slope.

B.1.2 Incoming long wave radiation

Niemelä et al. (2001b) also published a summary of incoming long wave radiation parameterizations; the following methods were obtained from this work. The original reference cited for each is again provided in italics following the equation.

$$iLW_{clr} = [1 - (1 + w)\cdot\exp(-(1.2 + 3\cdot w)^{0.5})]\cdot\sigma\cdot(T_0 + 273.15)^4 \qquad \textit{Prata, 1996} \quad \text{(B.8)}$$

$$iLW_{clr} = 59.38 + 113.7\cdot[(T_0 + 273.15) / 273.16)]^6 + 96.96\cdot(10\cdot w / 25)^{0.5} \qquad \textit{Dilley and O'Brien, 1998} \quad \text{(B.9)}$$

where iLW_{clr} = incoming long wave radiation under clear skies (W/m^2)
w = precipitable water content (cm)
σ = Stefan-Boltzman constant (5.67×10^{-8} W/m^{2}K^4)
T_0 = screen-level air temperature (ºC)

Screen-level temperature refers to a measurement made in a louvered screen meeting meteorological standards. In high snowfall areas, screens are typically adjusted to maintain a height of approximately 1.2 to 1.4 m above the snow surface (CAA, 2002, p. 47).

Precipitable water content was calculated using the following equation obtained from Niemelä et al. (2001b).

$$w = 46.5\cdot[e_0 / (T_0 + 273.15)] \qquad \textit{Prata, 1996} \quad \text{(B.10)}$$

where e_0 = screen-level water-vapour pressure (hPa)

The following method, obtained from Dürr and Philipona (2004), was used in all cases to estimate the screen-level water-vapour pressure.

$$e_{\text{sat}} = 6.1121 \cdot \exp[17.502 \cdot T_0 / (T_0 + 240.97)] \qquad \textit{Buck, 1981} \qquad \text{(B.11)}$$

where e_{sat} = saturated water vapour pressure (hPa)

$$e_0 = (\text{RH} / 100) \cdot e_s \qquad \text{(B.12)}$$

where RH = relative humidity (%)

To adjust incoming long wave radiation estimates obtained from Equations B.8 and B.9 for cloud cover, the following parameterization found in Niemelä et al. (2001b) was applied.

$$\text{iLW} = (1 + 0.26 \cdot c) \cdot \text{iLW}_{\text{clr}} \qquad \textit{Jacobs, 1978} \qquad \text{(B.13)}$$

where iLW = incoming long wave radiation under all sky conditions (W/m^2)
c = cloudiness (decimal fraction)

Konzelmann et al. (1994) presented the following equation for daily mean incoming long wave radiation, which was also evaluated.

$$\text{iLW} = [(0.23 + 0.483 \cdot [e_0 / (T_0 + 273.15)]^{0.125}) \cdot (1 - c^3) + 0.963 \cdot c^3] \cdot \sigma \cdot (T_0 + 273.15)^4 \qquad \text{(B.14)}$$

In addition, a long wave radiation parameterization developed by Iziomon et al. (2003) was included in the comparison.

$$\text{iLW} = \sigma \cdot (T_0 + 273.15)^4 \cdot \{1 - 0.43 \cdot \exp[-11.5 \cdot e_0 / (T_0 + 273.15)]\} \cdot [1 + 0.0050 \cdot (8 \cdot c)^2] \qquad \text{(B.15)}$$

A dataset consisting of 110 points was compiled by taking all incoming long wave radiation measurements from the winters of 2005 and 2006 for which a corresponding manual sky observation was available. Cloudiness was estimated from the manual sky observations as per Table B.1. A comparison of the four incoming long wave radiation estimation methods is included in Table B.3. The highest coefficient of determination ($r^2 = 0.84$, $p < 0.001$) corresponded to the combination of equations B.9 and B.13 (Figure B.2). These two equations were subsequently used when incoming long wave radiation estimates were required.

Table B.3: *Comparison between measured incoming long wave radiation and values estimated with several different methods.*

Method of estimating incoming long wave (equations)	***n***	**Coefficient of determination (r^2) with measured incoming long wave radiation**
B.6 and B.13	110	0.80
B.9 and B.13	110	0.84
B.14	110	0.68
B.15	110	0.81

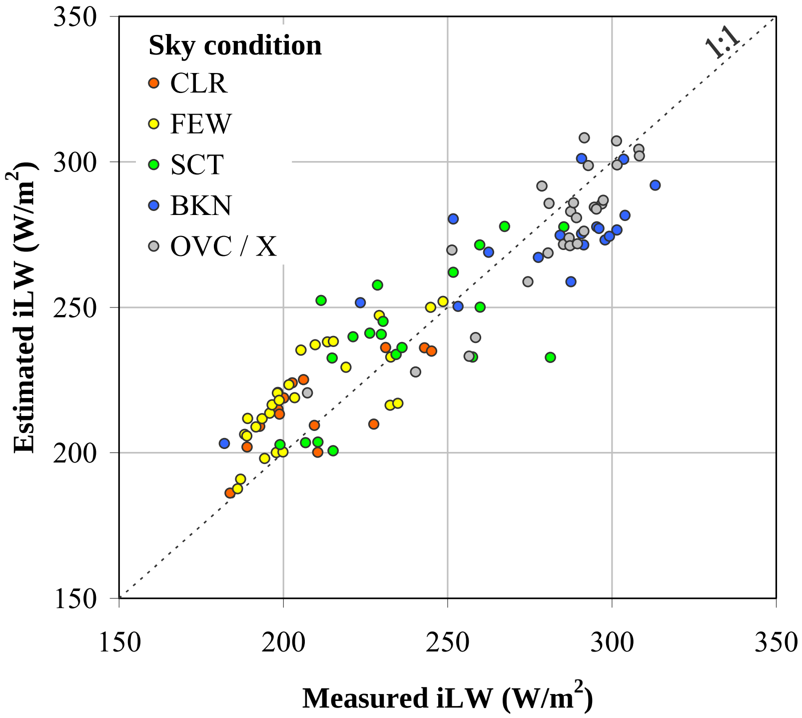

Figure B.2: *Comparison of measured and estimated incoming long wave radiation. Estimated values were calculated using equations B.9 and B.13. A significant coefficient of determination ($r^2 = 0.84$, $p < 0.001$) was found in the dataset ($n = 110$).*

B.1.3 Outgoing long wave radiation

Outgoing long wave radiation at the snow surface can be calculated using the following equation (Male and Gray, 1981).

$$\mathrm{oLW} = \varepsilon_s \cdot \sigma \cdot (T_s + 273.15)^4 \tag{B.16}$$

where oLW = outgoing long wave radiation ($\mathrm{W/m^2}$)
ε_s = emissivity of snow
σ = Stefan-Boltzman constant (5.67×10^{-8} $\mathrm{W/m^2K^4}$)
T_s = snow surface temperature (ºC)

Cited values for the emissivity of snow include 0.95 for a melting snowpack (Woo and Giesbrecht, 2000), 0.97 (Koivusalo and Heikinheimo, 1999) and 0.97 to 1.0 (Male and Gray, 1981). Warren (1982) suggests 0.99 as a reasonable value for snow and notes that, while albedo shows substantial variation with changes in snow properties, the emissivity of the snow surface is relatively independent of snowpack properties such as grain size, impurity content, snow depth, water content and density. A value of $\varepsilon_s = 0.99$ was used in this study for calculating outgoing long wave radiation at the snow surface.

Manual snow surface temperature measurements were made periodically at all array locations during the field experiments (Section 3.2.3). For times when manual measurements were not available, and for potential use in the warming model, an empirical equation for surface temperature was developed. A dataset including 418 hourly manual snow surface temperature measurements made during the field experiments was randomly split into two groups; 80% percent of the data to build the regression model and 20% for testing. Field measurements which indicated a snow surface temperature above 0º C were suspect, and therefore not included in the dataset.

Independent variables considered in the multivariate regression analysis included Julian day, time, cloudiness, air temperature, wind speed, aspect (represented as degrees from north and degrees from east) and slope angle. Cloudiness was estimated from manual sky observations as per Table B.1, air temperature values were hourly measurements obtained from the Mount Fidelity study plot and wind speed was based on a daily average value, also measured in the study plot.

Stepwise linear regression performed on the model building dataset (n = 334) identified significant ($p < 0.001$) coefficients for cloudiness, air temperature, wind speed and aspect. With the model building data, the regression equation provided below resulted in a coefficient of determination (r^2) of 0.63 and standard error of estimate (SEE) of 3.21 ºC. There is a problem with the linear regression equation, however, as normality of the residuals is rejected with both the Kolmogorov-Smirnov test ($D = 0.085$, $p < 0.05$) and the Lilliefors test ($p < 0.01$).

$$T_s = -12.029 + 7.090 \cdot c + 0.589 \cdot T_a + 1.217 \cdot u_{avg} + 0.0187 \cdot \mathrm{dfN} \qquad \text{(B.17)}$$

where T_s = snow surface temperature (ºC)
c = cloudiness (decimal fraction)
T_a = air temperature (ºC)
u_{avg} = average wind speed (m/s)
dfN = aspect (degrees from north)

Performance of Equation B.17 was also evaluated using the data points retained for model testing. Within the model testing dataset (n = 84), a significant coefficient of determination ($r^2 = 0.64$, $p < 0.001$) was found between snow surface temperatures calculated with Equation B.17 and measured values (Figure B.3). When used in development of the warming model, an upper limit of 0 ºC was applied with Equation B.17 to prevent unrealistic snow surface temperature estimates.

Because the linear regression equation violates the assumption of normally distributed residuals and due to previously noted concerns regarding drift in the manual surface temperature measurements (Section 3.2.3), a second means of estimating snow surface temperature was also considered. Based on measurements made in the Swiss Alps, Plüss (1997) proposed the following parameterization for daily mean snow surface temperature:

$$T_{\mathrm{s}} = T_{\mathrm{a}} + 7.5 \cdot (c^{1.15} - 0.67) \leq 0\ ºC \qquad \text{(B.18)}$$

Significant coefficients of determination were found between snow surface temperatures calculated with Equation B.18 and measured values in both the model building ($r^2 = 0.58$, $p < 0.001$, $n = 334$) and model testing ($r^2 = 0.61$, $p < 0.001$, $n = 84$) datasets. Figure B.4 shows the scatterplot of measured and estimated snow surface temperature values for the model testing data.

A lack of outgoing long wave radiation measurements or consistent surface temperature measurements prevented further verification of outgoing long wave radiation calculations prior to development of the warming model. Values estimated using both surface temperature equations (B.17 and B.18) were evaluated during development of the warming model. Where daily average estimated long wave radiation values were required, they were calculated using daily cloudiness observations, daily wind speed averages (if required) and the average of air temperature measurements made in the Fidelity study plot at 0700 and 1200.

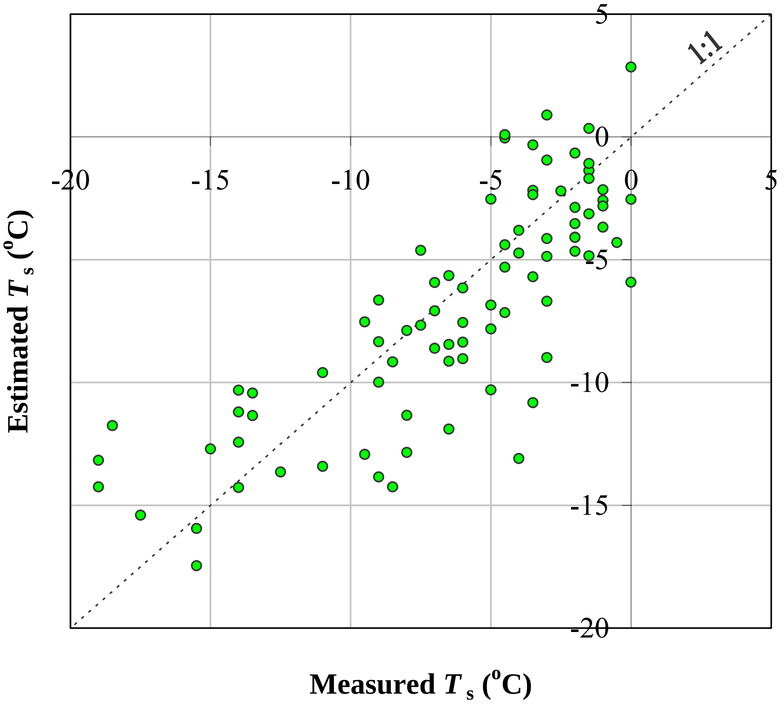

Figure B.3: *Comparison of measured snow surface temperatures with those estimated using the empirically derived regression equation (B.17). A significant coefficient of determination ($r^2 = 0.64$, $p < 0.001$) was found in the model testing dataset ($n = 84$). When used in development of the warming model, an upper limit of 0 ºC was applied to prevent unrealistic snow surface temperature estimates.*

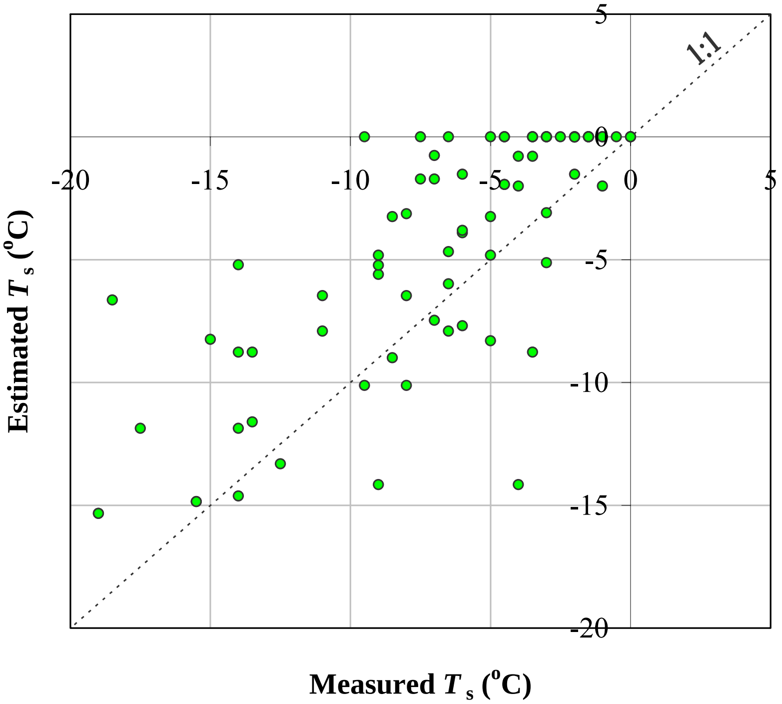

Figure B.4: *Comparison of measured snow surface temperatures with those estimated Equation B.18. A significant coefficient of determination ($r^2 = 0.61$, $p < 0.001$) was found in the model testing dataset ($n = 84$).*

B.2 Snowpack parameters

Development of the warming model also required estimates for snowpack parameters, such as albedo, extinction coefficient and conductivity, which influence the snow-surface energy balance. Because field measurements were not available to verify these parameters, individual evaluation of the best estimation method for each could not be completed. Different combinations of the albedo and extinction coefficient estimates were included in the preliminary stages of warming model development to determine which best fitted with the field measurements (Section 6.4.1).

B.2.1 Albedo

Five simple methods of estimating albedo were included in warming model development. The first was based on fixed albedo values found in Male and Gray (1981). Where manual snow profile observations indicated that the surface form consisted of wet grains (WG), as per the International Classification for Seasonal Snow on the Ground (Colbeck, 1990), an albedo of 0.61 was assigned. For any other type of surface snow grain type, the albedo was set to 0.86.

Henneman and Stefan (1999) developed the following empirical equation for snow albedo from measurements made over a freshwater lake in wintertime.

$$\alpha = -0.011 \cdot N + 0.83 \tag{B.19}$$

where α = snow surface albedo

N = number of days since snowfall

Equation B.19 applies only under non-melt conditions. When WG were present on the snow surface, a fixed value of 0.61 was again used.

Baker et al. (1990) found fairly strong relationships between field measurements and several empirically derived equations (both linear and exponential) relating the daily mean albedo decay to the number of days since snowfall. Equation B.20 is one of the equations developed and presented by Baker et al. (1990) which showed the highest r^2 and lowest standard error in comparison with their field data.

$$\alpha = 0.839 - 0.0473 \cdot N^{0.5} \tag{B.20}$$

Kondo and Yamazaki (1990) used the following equation for snow albedo in their snowmelt model.

$$\alpha = 0.4 + (0.85 - 0.4) \cdot \exp(-N / 4) \tag{B.21}$$

The final albedo parameterization included in the warming model analysis was obtained from Plüss (1997). In addition to the number of days since snowfall, this approach also considers mean daily air temperatures.

$$\text{for } T_a \leq 0\ ^\circ\text{C:} \quad \alpha = 0.4 + 0.5 \cdot \exp(-0.05 \cdot N) \tag{B.22}$$

$$\text{for } T_a > 0\ ^\circ\text{C:} \quad \alpha = 0.4 + 0.34 \cdot T_i^{-0.167} \tag{B.23}$$

where T_i = sum of positive daily mean air temperatures since last snowfall (ºC)

B.2.2 Extinction coefficient

All of the short wave radiation extinction coefficient estimates used were based on a linear relationship with snow density, as modelled in earlier versions of SNOWPACK (Lehning et al., 2002a). They followed the form:

$$\beta = \rho / c_1 + c_2 \tag{B.24}$$

where β = extinction coefficient (m^{-1})
ρ = snow density (kg/m^3)
c_1, c_2 = constants

Two sets of constants were tested during the early stages of warming model development (Table B.4).

Table B.4: *Summary of constants used in Equation B.24 to calculate short wave radiation extinction coefficient.*

Source	**c_1 (kg/m^2)**	**c_2 (m^{-1})**
Lehning et al. (2002a)	3	50
Meirold-Mautner (2004)	10	30

At each of the five discrete depth intervals for which daytime warming measurements were interpolated (5, 10, 15, 20, 25 cm), an average snow density over that depth was calculated from field measurements. Depth-averaged extinction coefficients were then determined using Equation B.24. Where manual density measurements were not available for thin snow layers, values were estimated from grain type and hand hardness observations (Geldsetzer and Jamieson, 2001a).

B.2.3 Conductivity

Sturm et al. (1997) compiled a dataset of 488 published measurements to develop the following parameterization for the effective thermal conductivity of snow.

$$\text{for } 156 \leq \rho \leq 600: \quad k = 0.138 - 1.01 \cdot (\rho / 1000) + 3.233 \cdot (\rho / 1000)^2 \qquad \text{(B.25)}$$

$$\text{for } \rho < 156: \quad k = 0.023 + 0.234 \cdot (\rho / 1000) \qquad \text{(B.26)}$$

where k = effective conductivity of snow (W/m·K)
ρ = snow density (kg/m^3)

The average densities calculated to estimate extinction coefficient were provided as input into either Equation B.25 or B.26 to determine average effective conductivity values.